Energy Advances

ROYAL SOCIETY OF CHEMISTRY

REVIEW ARTICLE

View Article Online
View Journal | View Issue

Cite this: *Energy Adv.*, 2023, 2, 1075

Synthetic approaches for perovskite thin films and single-crystals

Anastasia Soultati, [a] Marinos Tountas, [b] Konstantina K. Armadorou, [a] Abd. Rashid bin Mohd Yusoff, [c] Maria Vasilopoulou *[a] and Mohammad Khaja Nazeeruddin *[d]

Received 1st March 2023,
Accepted 4th June 2023

DOI: 10.1039/d3ya00098b

rsc.li/energy-advances

Halide perovskites are compelling candidates for the next generation of clean-energy-harvesting photovoltaic technologies owing to an unprecedented increase in power conversion efficiency and their low cost, facile fabrication and outstanding semiconductor properties. The potential of perovskite materials has been identified by understanding the fundamental science of perovskites such as crystallisation dynamics and charge carrier dynamics and finding various novel perovskite combinations from the periodic table. Current evidence suggests that the synthetic approach applied for the deposition of halide perovskite layers is a key factor dictating device efficiency and stability. In this review, we aim to investigate the large variety of synthetic procedures followed for the deposition of perovskite polycrystalline films and single crystal layers. We will summarize the current understanding and ability to influence material properties by using these synthetic methods and explore the link between synthetic approaches and material properties relevant to photovoltaic and other applications.

1. Introduction

Halide perovskites (HPs) have recently drawn great attention due to their outstanding optoelectronic properties, such as their solution processability,[1–4] high absorption coefficients, ambipolar charge carrier mobility and large carrier diffusion lengths, and facilely tunable composition and dimensionality[5–7] that can potentially enable the corresponding devices to exhibit unprecedented performances.[8–14] This unique combination of properties has stimulated intense research studies in solar cells,[15–20] light emitting diodes (LEDs),[21–25] field effect transistors (FETs),[26–29] and memories.[30–33] The significant performance metrics that have been achieved in these optoelectronic devices are strongly dictated by the method these HPs are synthesized/deposited in thin films. Moreover, perovskite single-crystals have also emerged as an alternative material platform that can overcome the limitations of common polycrystalline films.[34–38] For both perovskite films and single crystals, appropriate synthetic protocols are applied aiming to fabricate a high quality perovskite material and layer and the corresponding device that meets the specific needs of a given application.

However, the soft lattice of these perovskites poses several challenges to the formation of smooth, pinhole-free perovskite films.[39–49] Many methods have already been developed for the efficient synthesis and processing of polycrystalline films and single crystal layers. The aim of this review is to summarize recent approaches for the synthesis of perovskite films, both polycrystalline and single-crystal based, and discuss the advantages and obstacles encountered with each of these methods used to deposit this family of materials. This review is intended to be comprehensive and to provide a thorough description of the large variety of different processing routes applied for halide perovskite thin films and single crystals. A brief description of the basic halide perovskite material properties is given prior to the presentation of their fabrication methods, aiming to make the paper also accessible not only to those wishing to gain a holistic understanding of the whole field but also to those seeking essential information regarding a certain type of deposition process.

[a] *Institute of Nanoscience and Nanotechnology, National Centre for Scientific Research Demokritos, 15341 Agia Paraskevi, Attica, Greece. E-mail: m.vasilopoulou@inn.demokritos.gr*
[b] *Department of Electrical Engineering, Hellenic Mediterranean University, Estavromenos, 71410 Heraklion Crete, Greece*
[c] *Department of Chemical Engineering, Pohang University of Science and Technology (POSTECH), Pohang, Gyeongbuk 37673, Republic of Korea*
[d] *Group for Molecular Engineering of Functional Materials, Institute of Chemical Sciences and Engineering, École Polytechnique Fédérale de Lausanne (EPFL), Rue de l'Industrie 17, CH-1951 Sion, Switzerland. E-mail: mdkhaja.nazeeruddin@epfl.ch*

2. Structures, compositions and properties of 3D and 2D halide perovskites

Three-dimensional (3D) halide perovskites (HPs) crystallize in the ABX_3 perovskite structure, where A and B are monovalent and divalent cations, respectively, and X is a halide anion. The A^+ cations, in particular, are larger than the B^{2+} metallic ones and function as structural templates with their shape, size, and charge distribution being crucial factors for the stabilization of the perovskite structure. More specifically, A^+ is usually an organic ($CH_3NH_3^+$, methylammonium, MA; formamidinium, FA; $CH_6N_3^+$, guanidinium, Gua) or inorganic (caesium, Cs^+) cation, B^{2+} is a large atomic number metal (such as lead, Pb^{2+}; tin, Sn^{2+} and germanium, Ge^{2+}) and X^- is a halogen (chloride, Cl^-; bromide, Br^-; and iodide, I^-).

The simplest possible ABX_3 perovskite consists of a high-symmetry cubic structure belonging to the space group $Pm\bar{3}m$.[50] In this structure the halogen anions X^- occupy the vertices in $[BX_6]_4^-$ octahedra, which share corners in all three orthogonal directions to generate infinite 3D $[BX_3]^-$ frameworks, while the divalent metal cations B^{2+} are placed at the centers of these octahedra (Fig. 1).[51] The smallest volume enclosed by neighbouring octahedra defines a cuboctahedral cavity and hosts the monovalent cation A^+. Different possible perovskite structures can be regarded as being obtained by rotating or distorting the BX_6 octahedra, displacing the B^{2+} metal cations off-center and rotating the A^+ cations within the cuboctahedral cavity. More than one structure is usually found for a perovskite material with a given chemical composition, depending on the temperature and preparation method. For example, methylammonium lead triiodide ($MAPbI_3$), a prototypical hybrid organic–inorganic metal halide perovskite, can undergo phase transformations from cubic to tetragonal at a temperature of 54 °C and from tetragonal to orthorhombic at −111 °C during cooling.[52]

The crystal structure stability of HPs can be predicted by calculating the so-called tolerance factor, $\alpha = \frac{r_A + r_X}{\sqrt{2}(r_B + r_X)}$[53,54] (with r_i being the radii of i = A, B and X ions in the perovskite ABX_3), which gives an estimate of the ionic size mismatches that a perovskite structure can tolerate until a different structure-type is formed. Both the performance and stability of inorganic–organic perovskite solar cells are limited by the size of the cations required for forming an appropriate lattice. It has been found that compounds with tolerance factors of a = 0.9–1.0 have an ideal cubic structure; a = 0.8–0.9 results in a distorted perovskite structure with octahedral tilting (usually orthorhombic), while when the tolerance factor is higher than 1 or lower than 0.8 non-perovskite structures are formed (Fig. 2a).[55] It is common in the halide perovskite literature to denote the phase with a cubic structure as the α-phase and the phase with a non-perovskite structure as the δ-phase.[51] Based on the above considerations, only three A^+ cations known to date have tolerance values between 0.8 and 1 and are thus able to form a stabilized perovskite, namely Cs^+, $CH_3NH_3^+$ (MA), and $HC(NH_2)_2^+$ (FA).[56]

However, commonly used single-cation HPs present limitations due to their thermal or structural instabilities. $MAPbI_3$, for example, the prototypical halide perovskite studied in PSCs, degrades fast upon exposure to light and moisture (the latter is due to the hygroscopic nature of the methylammonium cation), while it is also decomposed during annealing at 85 °C even in an inert atmosphere.[57–59] On the other hand, despite being advantageous in terms of its bandgap (1.48 eV *vs.* 1.57 eV for $MAPbI_3$)[60] and thermal stability (it is relatively stable up to 150 °C in air), $FAPbI_3$ suffers from severe structural instability at room temperature as it commonly crystallizes into a photoinactive, non-perovskite hexagonal δ-phase (“yellow phase”) instead of a photoactive perovskite α-phase (“black phase”); in addition, it is sensitive to solvents or humidity.[61]

A reasonable way to overcome the limitations of single-cation (and anion) HPs is the compositional engineering approach by mixing cations and halides in order to achieve perovskite compounds with improved thermal and structural stability.[55] Intermixing different cations can combine the advantages of the constituents, while avoiding their drawbacks. Mixed cation 3D perovskites of the composition $(MA)_x(FA)_{1-x}PbI_3$, where x = 0.6, delivered superior device performance when used as light-harvesting layers in mesoscopic solar

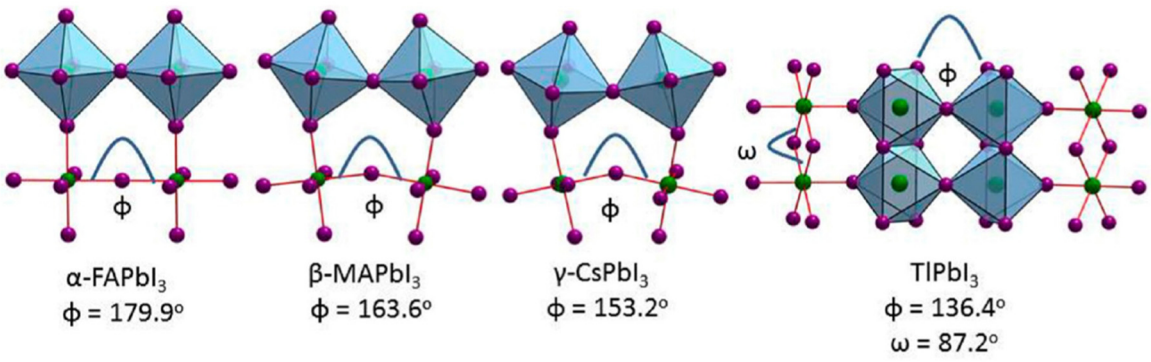

Fig. 1 Crystal structures of the $APbI_3$ series at room temperature for A = FA, MA, Cs, Tl, and NH_4 cations, highlighting the effect of the structural distortions and the connectivity of the $[PbI_6]^{4-}$ octahedra. Adapted with permission from ref. 51.

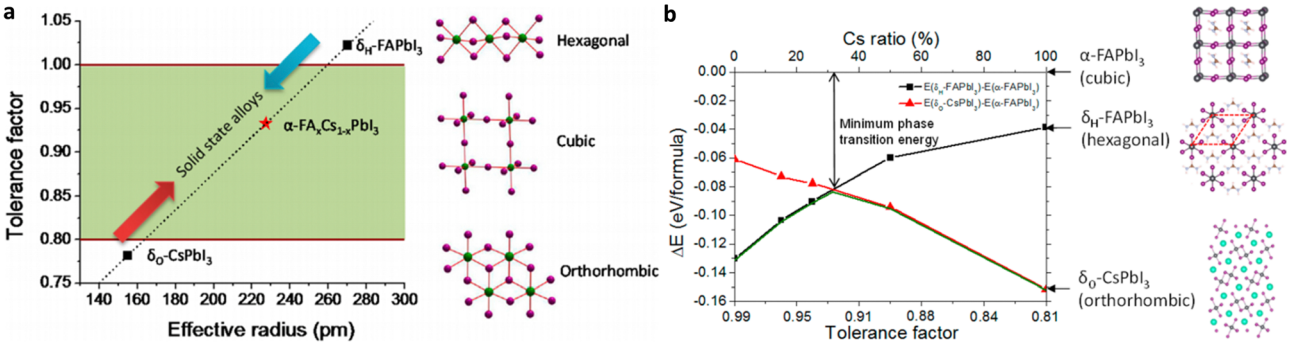

Fig. 2 (a) Correlations between the tolerance factor and crystal structure of perovskite materials. (b) Calculated energy difference between the α-phase and different δ-phases for $FA_{1-x}Cs_xPbI_3$ alloys with different Cs ratios. Adapted with permission from ref. 55.

cells.[62] The mixed-cation composition with optimized stoichiometry $MA_{0.6}FA_{0.4}PbI_3$ outperformed the single-cation compositions $MAPbI_3$ and $FAPbI_3$, while it also completely avoided the undesirable formation of the δ-phase, while maintaining the red-shifted band gap of $FAPbI_3$. The superior carrier-collection efficiency was related to the longer exciton lifetime of more than 130 ns in the $MA_{0.6}FA_{0.4}PbI_3$ material. These results showed that even a small amount of MA is sufficient to induce a preferable crystallization into the photoactive phase of the FA perovskite, resulting in a more thermally and structurally stable composition than the pure MA and FA compounds. This illustrates that the MA can be thought of as a "crystallizer" (or stabilizer) of the black phase FA perovskite. The fact however that MA is only slightly smaller than FA still permits a large fraction of the yellow phase to exist. Furthermore, by alloying $FAPbI_3$ with $CsPbI_3$, the tolerance factor can be effectively tuned, and the stability of the photoactive α-phase of the mixed $FA_{1-x}Cs_xPbI_3$ perovskite is significantly enhanced (Fig. 2b).[55] These mixed cation perovskite films demonstrate much improved stability in a high-humidity environment and better solar cell performance and device stability than the $FAPbI_3$ counterparts.

Moreover, the substitution of the larger I atoms with smaller Br ones in the mixed halide structure, $MAPb(I_{1-x}Br_x)_3$, for $x > 0.2$, leads to the reduction of the lattice constant and a transition from the distorted tetragonal perovskite structure of pure $MAPbI_3$ to the cubic perovskite structure of $MAPbBr_3$, hence inducing advanced optoelectronic properties and superior PSC performance.[63,64] Further intermixing both MA/FA cations and I/Br anions in an optimized $(FAPbI_3)_{0.85}(MAPbBr_3)_{0.15}$ perovskite structure stabilizes the perovskite phase and increases its crystallinity.[65] As a step forward, intermixing Cs^+, which has a considerably smaller ion than both MA^+ and FA^+, in a triple cation configuration $Cs_x(MA_{0.17}FA_{0.83})_{(100-x)}Pb(I_{0.83}Br_{0.17})_3$ provides additional versatility in fine-tuning high quality perovskite films that can yield stabilized PCEs.[15] Incorporation of optimum amounts of Cs^+ reduces the trap density by one order of magnitude, which is responsible for the increased V_{OC} and FF, eventually leading to an enhancement in PCE. The triple cation perovskite films are less affected by temperature for a fixed halide ratio, while an increased Br content also contributes considerably to thermal stability. Cs^+ induces the black phase of FA-based HPs at room temperature and better morphology as more uniform grains are formed that enable better charge transport, which in turn endows the fabricated devices with higher FFs. Moreover, alkali halide (NaX) additives effectively passivate both the organic cation and halide anion vacancies in the triple CsMAFA perovskite. Especially, sodium fluoride forms strong hydrogen bonds (N–H···F) with the organic (FA/MA) cations and strong ionic bonds with Pb in the triple perovskite film, protecting the materials from degradation and leading to long-term stability of the corresponding device.[66]

A pseudo-halide anion, formate ($HCOO^-$), also improves the growth and crystallization of perovskite films.[67] The insertion of FAHCOO into the precursor solution removes the halide vacancies in the $FAPbI_3$ film, reducing the trap-assisted recombination. Consequently, formate results in an increase of FF, leading to higher PCE.[68] Moreover, the elimination of deleterious lattice defects in $FAPbI_3$, which can lead to degradation of the halide perovskite film, is beneficial for the operational stability of PSCs.

Furthermore, incorporation of traces of small radius rubidium (Rb) (r_{Rb^+} = 152 pm *versus* r_{Cs^+} = 167 pm) has been recently found to stabilize the black phase of FA perovskites.[69] Whereas it is clear from the tolerance factor discussion above that Cs^+ is the only elemental cation that is large enough to sustain the perovskite structure, Rb^+ can still be integrated into PSCs, despite not being suitable as a pure $RbPbI_3$ compound. PSCs based on perovskite materials bearing the rubidium cation along with caesium and/or organic cations have reached reasonable device performances.[16] The outstanding maximum V_{OC} of 1240 mV indicates a "loss in potential" (difference between V_{OC} and the band gap) of only ~0.39 V, which is one of the lowest recorded for any perovskite material, implying very small non-radiation recombination losses owing to its very low bulk and surface defect density. Moreover, it was observed that the charge transport within the RbCsMAFA perovskite layer is substantially faster than in CsMAFA, which is already much more defect-free than MAFA. Enhancement in charge extraction can also be achieved by reactive surface engineering of the perovskite layer. The creation of a built-in electric field in the

surface of the perovskite film reduces surface recombination, which favors the improvement of the photovoltaic parameters.[70]

Halide perovskites exhibit a direct bandgap, which can be effectively tuned through compositional adjustment to allow absorption to reach the high energy frontier of the near infrared spectral region. The change in band gap observed with compositional adjustment, such as tailoring of halide concentration, can be explained as follows: the electronic states at the top of the valence band are mainly of halide p-character with a small contribution from metal s-orbitals (*i.e.*, Pb 5s orbitals); those at the bottom of the conduction band are mainly derived from the metal p states (*i.e.*, Pb 6p).[50] The fully-occupied 5s orbital of Pb^{2+} has strong antibonding coupling with I 5p, making upper valence bands dispersive. The strong s–p antibonding coupling results in a small hole effective mass, which is comparable with electron effective mass, making $MAPbI_3$-based perovskites ideal candidates for thin-film solar cells with a p–i–n configuration. The replacement of I^- with Cl^- or Br^- leads to an increase in the band gap, due to the lower-lying Br-4p and Cl-3p electronic states that populate the top of the VB.[71] In addition, the smaller dielectric constant associated with the larger bandgap in $MAPbBr_3$ results in a larger binding energy, a smaller Bohr radius, a larger effective *g*-factor (*i.e.*, a quantity that characterizes the magnetic moment and angular momentum of an atom or particle), and larger oscillator strength of the lowest-energy excitons in $MAPbBr_3$ compared to those in $MAPbI_3$.[63]

Due to the antibonding character and mixing of s and p orbitals to form band extrema, perovskites present only shallow defects, primarily A- and X-site vacancies, while interstitial and antisite defects, which would form detrimental deep trap states in the electronic structure, are almost absent.[72] However, several types of extrinsic surface defects caused by unsaturated surface bonds and/or the surrounding environment are a major issue in grainy, polycrystalline HP films. For instance, X-terminating surfaces form traps due to the lack of local stoichiometric composition and improper surface bonding, which can be mitigated by introducing an appropriate passivation agent (PA). In an effective passivation scheme, new chemical bonds are formed at the perovskite surface and the derived orbitals shift the defect level either toward or into the band edges, hence suppressing the detrimental influence of the defect.[73]

In a similar manner, substitution of Pb with Sn lowers the conduction band bottom, hence reducing the bandgap due to the lower-lying Sn-p states (1.2–1.4 eV in Sn-based iodide perovskites as compared to 1.45–1.7 eV in Pb-iodide perovskites).[51] This arises from the greater instability of the Sn^{2+} lone pair of electrons (residing in the s orbital), which in the octahedral coordination environment is pushed up in energy, creating broader bands than the corresponding Pb lone pair. In a first approximation, the MA cations do not contribute to the optical absorption, and their role is to act as a structural filler and to ensure the charge neutrality of the unit cell. However, they can affect the band gap energetics through steric and coulombic interactions, which may deform the perovskite lattice in a cation-specific way. On the other hand, mixed halide perovskites were found to be prone to photo-instability as photo-excitation during light-soaking was suggested to cause halide segregation into two crystalline phases, namely iodide-rich and bromide-rich domains, the former having a lower band gap and acting as a recombination trap centre, thus limiting the photovoltage attainable with these materials.

Two dimensional (2D) HPs can be generally described by the general formula $L_2A_{n-1}M_nX_{3+1}$, where L is a large aliphatic or aromatic alkylammonium cation of the chemical type R-NH_3, such as 2-phenylethylammonium (PEA) and *n*-butylammonium (*n*-BA).[74] They are also known as Ruddlesden–Popper (RP) layered perovskites because they consist of alternative organic spacer and perovskite layers. Other structures of the 2D perovskites are the Dion–Jacobson (DJ) phase and the phase with alternating cations in the interlayer space (ACI), corresponding to the differences in crystallography and stacking motif, respectively.[75] They are hence quite similar to conventional 2D materials having a van der Waals layered crystal structure. The $(A_{n-1}M_nX_{3n+1})^{2-}$ part of their formula denotes the conductor layer that derives from the parent 3D (AMX_3) perovskite. The MX_6 octahedrons form the perovskite sub-layers that are sandwiched by the insulating organic spacers formed by the long chain molecular cations. The number of BX_6 octahedrons and thus the thickness of each perovskite layer are defined by the *n* value ($n = 1, 2, 3, 4, \ldots$) and can be adjusted by careful control of the stoichiometry.[76]

The incorporation of large organic spacers within their structure endows this class of HP materials with superior structural, thermal and moisture stability.[77] Their structural stability is due to the strong van der Waals forces among the organic layers.[78] Notably, the formation of even a small amount of a 2D perovskite structure can successfully inhibit the low-temperature phase transition of $FAPbI_3$ and $CsPbI_3$ perovskites, hence rendering α-$FAPbI_3$ and α-$CsPbI_3$ stable at room temperature.[79] The moisture stability is due to the hydrophobic nature of the organic spacers, typically ammonium cations, that prohibit the water molecules from penetrating into the perovskite crystal lattice.[80] In addition, ion migration, which is a severe limitation in PSCs based on 3D HPs, is not a great issue in 2D RP perovskites due to the higher activation energy of ion migration in 2D perovskites compared to 3D ones with similar compositions.[81] Moreover, ''edge states'' that existed in perovskite layers when $n > 2$ can provide a direct pathway for dissociating excitons into longer-lived free carriers.

However, besides their exceptional overall stability, 2D HPs also present some not very appealing characteristics regarding their application in PSCs. The electrically insulating nature of the organic spacer and the high conductivity of the perovskite conductor layers give rise to a natural multiple-quantum-well structure: the perovskite layers serve as potential ''wells'', while the organic spacer layers play the role of potential ''walls''. This results in a weaker absorption ability of RP 2D perovskites within the visible spectrum due to their larger bandgap values compared to the 3D counterparts. For example, the bandgap (E_g) values of $BA_2MA_{n-1}Pb_nI_{3n+1}$ and $PEA_2MA_{n-1}Pb_nI_{3n+1}$ RP

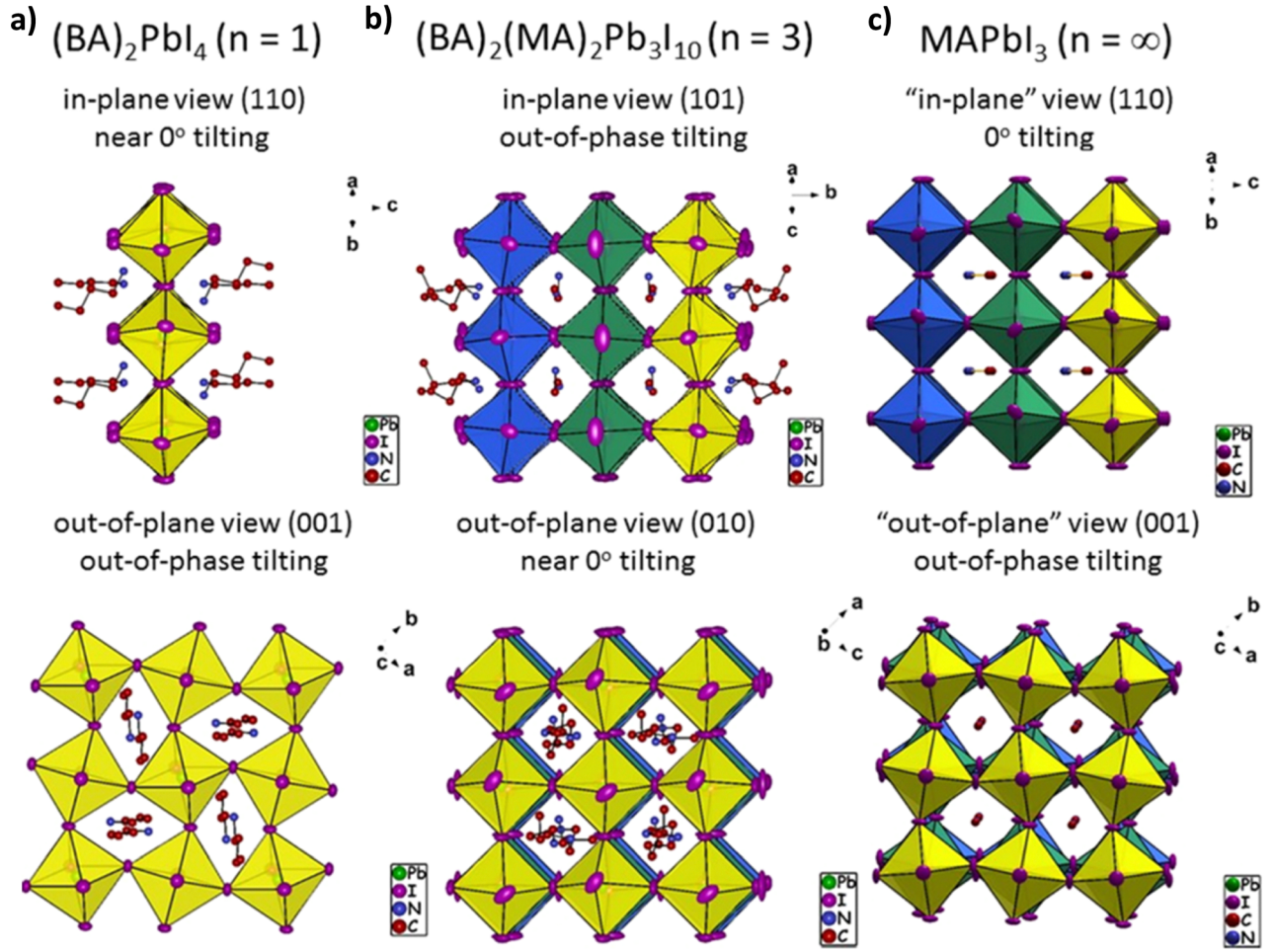

Fig. 3 Views of the (a) $(BA)_2PbI_4$ single-layer (n = 1), (b) $(BA)_2(MA)_2Pb_3I_{10}$ three-layer (n = 3) 2D, and (c) $MAPbI_3$ ($n = \infty$) 3D lead iodide perovskite crystal structures, highlighting their three-dimensional distortions. This figure illustrates the differences in the distortion modes of the n = 3 perovskite, emphasizing the in-plane and out-of-plane views of the perovskite slabs. Slabs belonging to different layers have been drawn in different colors (yellow, blue, green) to project the connectivity of the slabs in the third dimension. Adapted with permission from ref. 86.

perovskites are 2.24 eV and 2.36 eV (for n = 1), respectively,[82,83] while that of $MAPbI_3$ is only 1.54 eV.[84] Moreover, they present higher exciton binding energies (BEs), which make it more difficult for dissociation of excitons to photogenerated carriers to occur.[85] Excitons in 2D HPs are generally considered as the Wannier-type and their BEs in a single layer (n = 1) RP perovskite are in the range of ~157–480 meV (depending on the organic spacer, Fig. 3).[86,87] This large exciton BE is much higher than the thermal energy at room temperature (k_BT = 25.7 meV). Therefore, the photogenerated electron and hole pairs in RP HPs are strongly bound together by coulombic attraction. This is why the so-called excitonic absorption can be easily observed even at room temperature in these 2D perovskites in the form of a sharp peak below the bandgap onset. However, in most cases the excitonic absorption is merged with the absorption onset at room temperature, while at low temperatures this sharp peak is quite distinct.

In addition, the insulating organic spacer largely prohibits carrier transport, hence inducing charge accumulation and non-radiative recombination at the conductor/insulator interface. Moreover, the charge extraction can also be hindered by the insulation of the organic spacers. The charge mobility is much higher in the direction along the perovskite slabs than in the direction perpendicular to the orientation of these slabs. To this end, for efficient 2D PSCs it is important to have perovskite slabs with the out-of plane orientation, so that thicker films with balanced charge transport and light absorption can be used to achieve a high PCE.

Because of these unfavorable characteristics, RP perovskite-based PSCs have lagged behind in efficiency compared to their 3D counterparts, and the goal of current research efforts is to maximize the efficiency without compromising their stability. For example, huge research efforts have been devoted to altering the composition of 2D perovskites, aiming to improve their optoelectronic properties. These also include molecular design of spacer cations, such as altering alkyl chain length,[88] exposing ammonium dications,[89] and inserting π-conjugated segments.[90] Thus, a much wider

range of optoelectronic properties can be tuned for 2D perovskites than for 3D analogues.

An attractive approach to tackle the limitations of lower absorption and limited charge transport of 2D HPs is their combination with the parent 3D structure. In fact, as the value of n in the perovskite formula increases above 10, HPs with properties similar to those of their corresponding 3D counterparts are obtained; yet these materials present features of 2D perovskites.[91] Typically, the absorption onset of such perovskite materials combining the 2D and 3D structures is close to that of the corresponding 3D counterparts. Moreover, as the bandgap values of 2D perovskite phases are much larger than those of 3D ones, charges are highly confined to the 3D phase, hence overcoming the limitations of trapping and recombination at the interfaces between layers in the 2D phase, resulting in longer carrier lifetimes.[92] Nevertheless, the presence of the 2D component endows their devices with exceptional stability and ultrahigh V_{OC} values resulting in PCEs comparable to 3D ones, indicating them to be highly attractive candidates for PSCs. Finally, due to their highly hydrophobic nature and resilience to moisture, thin 2D perovskite films are also inserted as protective interlayers at either the bottom or top side of a 3D perovskite absorber.[93]

3. Synthetic approaches for polycrystalline perovskite films

The structural and optoelectronic properties of HPs are highly determined by the synthetic procedure adopted for their preparation. This is because only high-quality films can enable excellent intrinsic perovskite material characteristics to be fully exploited. A variety of synthetic procedures for 3D perovskites aiming to achieve high-quality perovskite films has been reported. They can be categorized into vacuum vapor deposition and solution processes.

3.1 Vacuum deposition methods

With the vacuum deposition method, high-quality perovskite films and, consequently, high efficiency PSCs can be obtained. The perovskite films are prepared by co-evaporation of the two precursors, the inorganic metal halide (MX_2 such as PbI_2) and the organic halide salt (*i.e.*, MAX, FAX, CsX, where X = I, Br, Cl). With this technique high quality perovskite films that exhibit satisfactory substrate coverage and uniformity within expectations can be constructed; such thin films are highly appropriate for planar junctions. For example, in 2013 Snaith and coworkers succeeded in achieving a record efficiency of 15% in planar PSCs by using a dual-source vapor deposition system to deposit $MAPbI_{3-x}Cl_x$ perovskite films of superior quality by evaporating lead chloride ($PbCl_2$) and methylammonium iodide (MAI) precursors simultaneously.[94] However, this method requires the use of expensive vacuum facilities, thus increasing the device manufacturing cost. Moreover, it is not appropriate for the fabrication of mesoscopic PSCs, which requires the infiltration of the perovskite pigment onto mesoporous metal oxide.

3.1.1 Thermal evaporation. Thermal evaporation can be described as a physical process during which one or more precursor materials are placed inside a semimetal basket and are evaporated above this basket source when heated under low pressure conditions at around 10^{-6} Pa or lower. The vapors are then sublimed into the cooler substrate surface and, subsequently, deposited onto it. By employing vacuum conditions, the vapor particles can travel freely for longer distances from the source towards the substrate, thus producing a final film with better morphology and quality compared to solution-based techniques. Moreover, this method can be used in the deposition of layered thin films towards the creation of multiple junction solar cells on top of large substrates, which is quite promising for the creation of larger devices.[95] Another considerable advantage making the technique an attractive option for scale-up is its employment in the case of flexible substrates. A determining parameter for this technique, however, would be the evaporation temperature of each moiety, which is critical in controlling the grain size.[96] This family of techniques can be divided into dual-source evaporation and sequential evaporation.

3.1.1.1 Single source and dual-source vapor deposition (VD). The easiest way to employ thermal evaporation is by one-step evaporation of the precursor material on top of the desired substrate. For example, the PbI_2 and MAI precursor salts are placed inside metal boats, are evaporated simultaneously under vacuum conditions and then deposited on the desirable surface, which is then annealed for the film crystallization to be completed (Fig. 4a).[95] However, this process requires careful adjustment of the deposition rate of each reagent, since the stoichiometry of the perovskite plays an important role in the efficiency of the final thin film.[92] Another possibility would be for the $MAPbI_3$ powder to be prepared before being placed inside the metal basket under vacuum conditions and evaporated.[97] This would allow better control over the stoichiometry of the thin film, which would affect its properties. In both cases, this method offers the deposition of extremely uniform and pinhole-free films of adjusted thickness all over the substrate area.[98] The improved uniformity of the perovskite film is very important to ensure successful fabrication of not only highly efficient small-size perovskite optoelectronic devices,[99] but also of large-area devices.[100,101]

3.1.1.2 Sequential evaporation. During sequential evaporation, PbI_2 powder is first sublimed onto the substrate through the same process as the dual source technique. Following this, MAI reacts with the already deposited inorganic layer and forms the final thin film, accompanied by a color change (Fig. 5a–c). A major advantage of this sequential method is the highly smooth surface compared to solution processes, due to the first-deposited PbI_2 film. Moreover, films created through a two-step process exhibit full surface coverage and high crystallization phase purity,[101] because of the low-

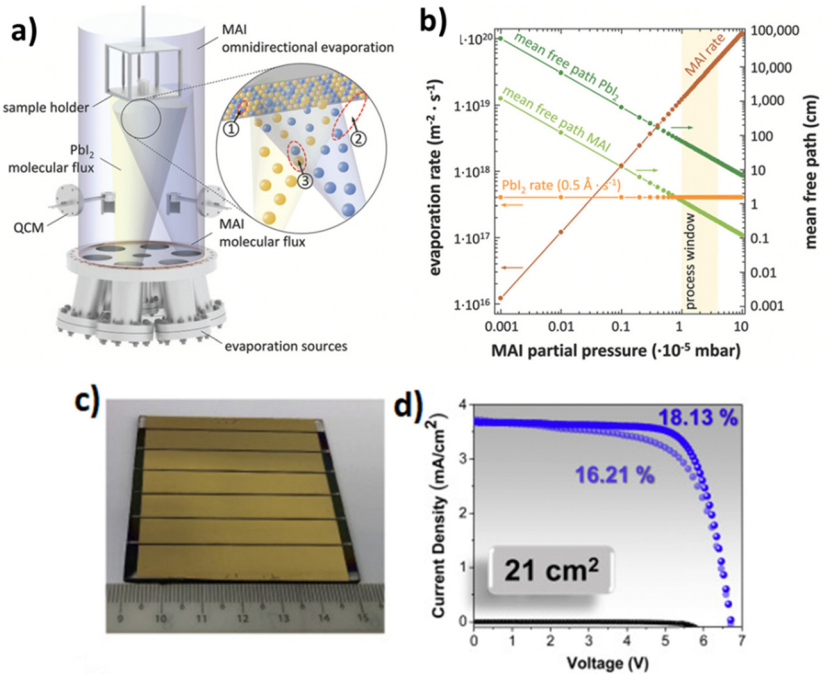

Fig. 4 Schematic illustration of the employed evaporation system and chemical processes that can take place during the co-evaporation of PbI_2 and MAI. (a) During co-evaporation three different reaction paths are conceivable: (1) a reaction of as-deposited PbI_2 with MAI on the substrate, (2) a delayed reaction of as-deposited PbI_2 with MAI from the environment, and (3) a reaction of PbI_2 with MAI before reaching the substrate. (b) Theoretically expected evaporation rates and mean free paths of PbI_2 and MAI in an omnidirectional process atmosphere as a result of the high vapor pressure and low evaporation enthalpy of MAI. Adapted with permission from ref. 95. (c) Image of a 21 cm^2 active area PSM consisting of 6 series-connected sub-cells. (d) Treated-$MAPbI_3$ PSM dark, forward, and backward *J*–*V* curves measured in air. Adapted with permission from ref. 99.

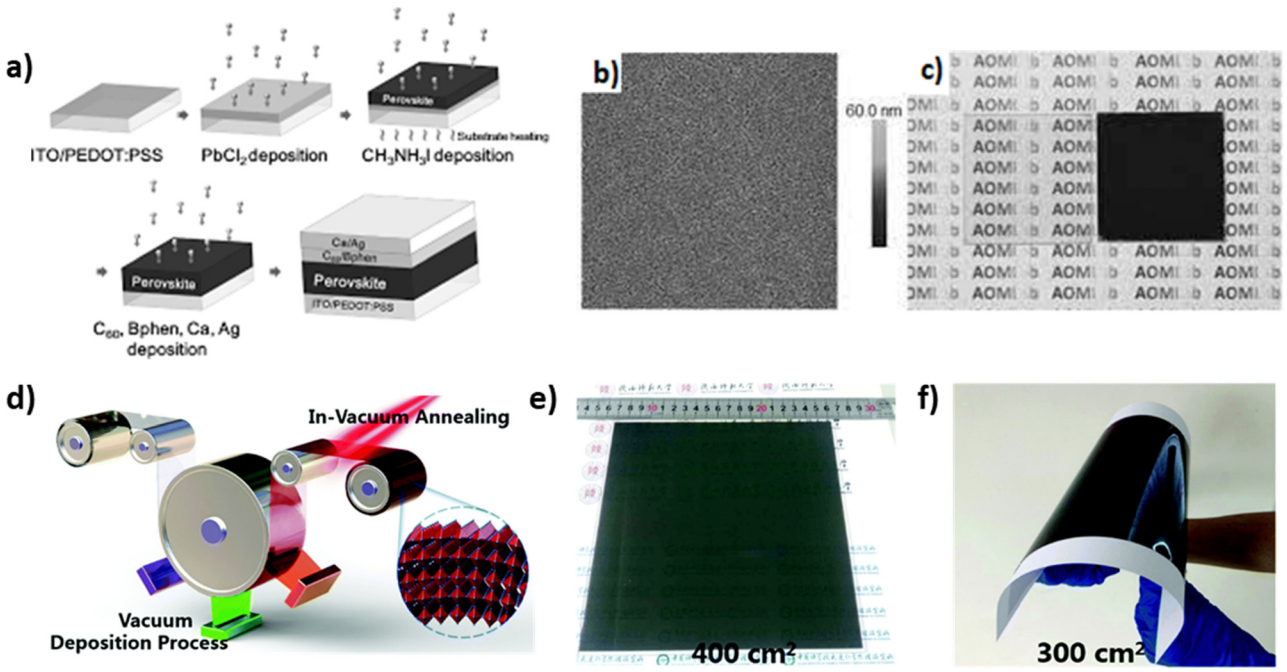

Fig. 5 (a) Schematic illustration of perovskite solar cells fabricated by sequential layer-by-layer vacuum deposition. (b) AFM image (30 μm^2) of the vacuum-deposited $PbCl_2$ thin film. (c) Photographs of the vacuum deposited $PbCl_2$ (left) and perovskite (right) thin films. Adapted with permission from ref. 102. (d) Schematic illustration of multisource vacuum deposition with an in-vacuum annealing process for large-area perovskite films. Photographs of FA-based perovskite films deposited on (e) glass and (f) PET substrates. Adapted with permission from ref. 104.

contamination deposition under vacuum conditions during the molecular time-of-flight. In any case, more perovskite films with better carrier-diffusion properties are fabricated with this method, since the size of the grains is larger and the control over the film properties is more effective through the control of each moiety separately.[102] This layer-by-layer deposition is affected by physicochemical factors such as the temperature of the substrate, which, when not properly controlled, could result in non-stoichiometric films. It has been reported that the post-sublimation steps of the crystallization can be performed under ambient conditions so that this problem is avoided, since the air moisture contributes to the transformation of the unreacted MAI to $MAPbI_3$.[103] Unfortunately, in spite of the exceptionally uniform films and the high reproducibility that this technique offers, the cost of the infrastructure required for the perovskite formation is not a favorable factor towards its use on a larger scale. Nevertheless, Feng *et al.* demonstrated uniform large-scale $Cs_{0.15}FA_{0.85}PbI_3$ perovskite films of high quality using a three-source layer-by-layer vacuum deposition method (Fig. 5d–f).[104] The prepared perovskite films showed also large grain size and good crystallinity, resulting in highly efficient $Cs_{0.15}FA_{0.85}PbI_3$-based solar cells with outstanding stability.

3.1.2 Pulsed laser deposition (PLD). Pulsed laser deposition is another type of physical vapor deposition technique. In this method, the precursor material, sometimes in pellet form, is subjected to a pulsed laser beam of high energy, while being inside a high vacuum chamber (Fig. 6a). In this way, the laser vaporizes the target material almost instantly, thus creating a plasma plume which is deposited as a thin layer onto the desired substrate. The substrate can be either perpendicular (on-axis deposition) or parallel to the plasma plume (off-axis deposition), with the latter not being used as often as the former.[105] This methodology was employed in earlier years for the deposition of a moiety onto a substrate by maintaining the precursor composition on top of the deposited film for perovskite-like structures. Additionally, the solid precursor materials can be kept at room temperature during the deposition and the plasma energy source is placed outside the vacuum chamber, making this method quite simplistic compared to other vacuum methodologies.[106] At the same time, the superior quality of the crystalline layers could be attributed to the high energy of the impacting ions.[108]

However, one possible disadvantage of PLD could be the non-uniform deposition of films, since re-evaporation takes place after the initial laser burst, which could be counter-attacked by multiple laser pulses on top of the same substrate. Moreover, the amount of material deposited should gradually decrease with each pulse, so as to create the appropriate number and size of crystals inside the perovskite layer. In this way, one can gain control over the film thickness.[105,106]

Nevertheless, some additional difficulties may still arise in the case of organic–inorganic thin films caused by the different vaporization rate of each composing moiety, which in turn affects their deposition. Although this may be of little importance in conventional perovskite film fabrication,[107] its consequences are more apparent in more complicated structures such as $(NH_2CH)_{1-x}(CH_3NH_3)_xSnI_3$ that shows enhanced thermal stability. As reported by Hoffmann-Urlaub *et al.*,[108] the organic moiety creates a smoother surface on the film, because of its volatilization through plasma, while the inorganic moiety has a different morphology due to a different forming path, thus creating inhomogeneous areas on the substrate. This is why the target material should not be stoichiometric but its organic part is in excess.

In this way, it is obvious that many parameters should be controlled so as to fabricate large-grained thin films. Some of them would be the power of the beam, the pulse repetition rate, the deposition pressure and the substrate temperature (Fig. 6b and c). Such a procedure tailored to each deposition and subsequent high perovskite solar cell performance could be made possible through a two-step hybrid process.[109] This technique for $MAPbI_3$ perovskites involves the deposition of the lead halide through PLD onto the substrate and the subsequent addition of methyl ammonium iodide by spin-coating, followed by an annealing step. Through this process, an increase in grain size and control over film thickness are observed, minimizing any defects and increasing carrier

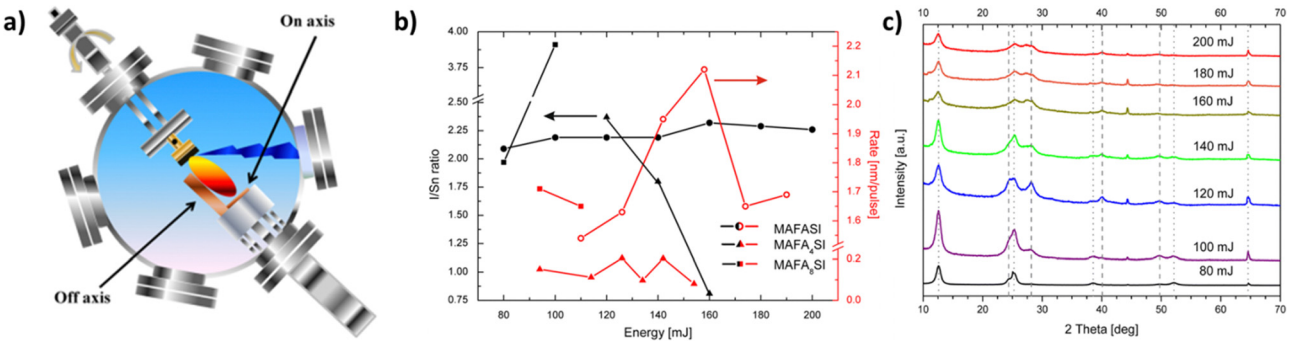

Fig. 6 (a) Schematic representation and photograph of substrate arrangements for "on-axis" and "off-axis" deposition by pulsed laser deposition (PLD). Adapted with permission from ref. 107. (b) Ratio of iodine to tin (black symbols) and deposition rate (red symbols) as functions of energy density for MAFASI, $MAFA_4SI$ and $MAFA_8SI$ thin films. (c) Diffractograms of MAFASI thin films deposited at various energies, ranging from 80 to 200 mJ. The dotted lines indicate the positions of [001]-reflections of α-SnI_2, while the dashed ones indicate the (111), (002), (022) and (222)-lattice planes of the perovskite structure from left to right, respectively. Note that the intensities are plotted on a linear scale. Adapted with permission from ref. 108.

mobility. In this way, the creation of highly crystalline and uniform films is possible, while the low temperature employed is promising for future fabrication under more flexible conditions.

3.1.3 Chemical vapor deposition. Chemical vapor deposition (CVD) can be characterized as a vacuum deposition chemical process. At first, the volatile precursors PbI_2 and MAI of the perovskite film are generated and then injected from the main gas flow into a quartz chamber under vacuum conditions. In the chamber, gas-phase reactions take place, forming intermediate products which are then deposited on top of the substrates. The precursors are adsorbed onto the surface of the substrates, followed by diffusion of the reagents, nucleation and island growth, with the final result being the formation of the perovskite film. During the film formation, the precursors can either react or decompose. Any volatile by-products formed during the reaction are desorbed and transferred to the main flow.[110] When the pressure conditions during the reaction are taken into consideration, the CVD techniques can be categorized as atmospheric pressure CVD (APCVD), low-pressure CVD (LPCVD) and ultrahigh vacuum CVD (UHVCVD).[111,112] If the gas phase is taken into consideration, the technique can have as subcategories metal organic chemical vapor deposition (MOCVD), aerosol assisted CVD (AACVD), direct liquid injection CVD (DLICVD), and hybrid physical CVD (HPCVD).[113–116] The easiest way of categorization, however, is based on the methodology used: one-step and two-step CVD. Fig. 7 illustrates some examples of CVD systems for deposition of perovskite films.

3.1.3.1 One-step CVD. During one-step deposition, the organic and inorganic moieties in the gas phase of the perovskite thin film are simultaneously injected into a vacuum chamber, are co-evaporated and adsorbed on the preheated substrate. This method is quite helpful, since no secondary evaporation step is necessary and is a gas-only method.[110] However, this method can also be applied in the case of mixed halide perovskites, producing pinhole-free $CH_3NH_3PbI_{3-x}Cl_x$ films, containing $PbCl_2$, PbI_2 and MAI moieties, as far as planar cells are concerned (Fig. 8).[113] In this case, the differences in vaporization time should be taken into consideration. The best results in terms of crystallinity are obtained with the use of argon as a gas carrier, at 360 °C evaporation temperature and 100 °C annealing temperature. In this way, perovskite films with larger grain size and longer carrier diffusion lengths can be obtained.

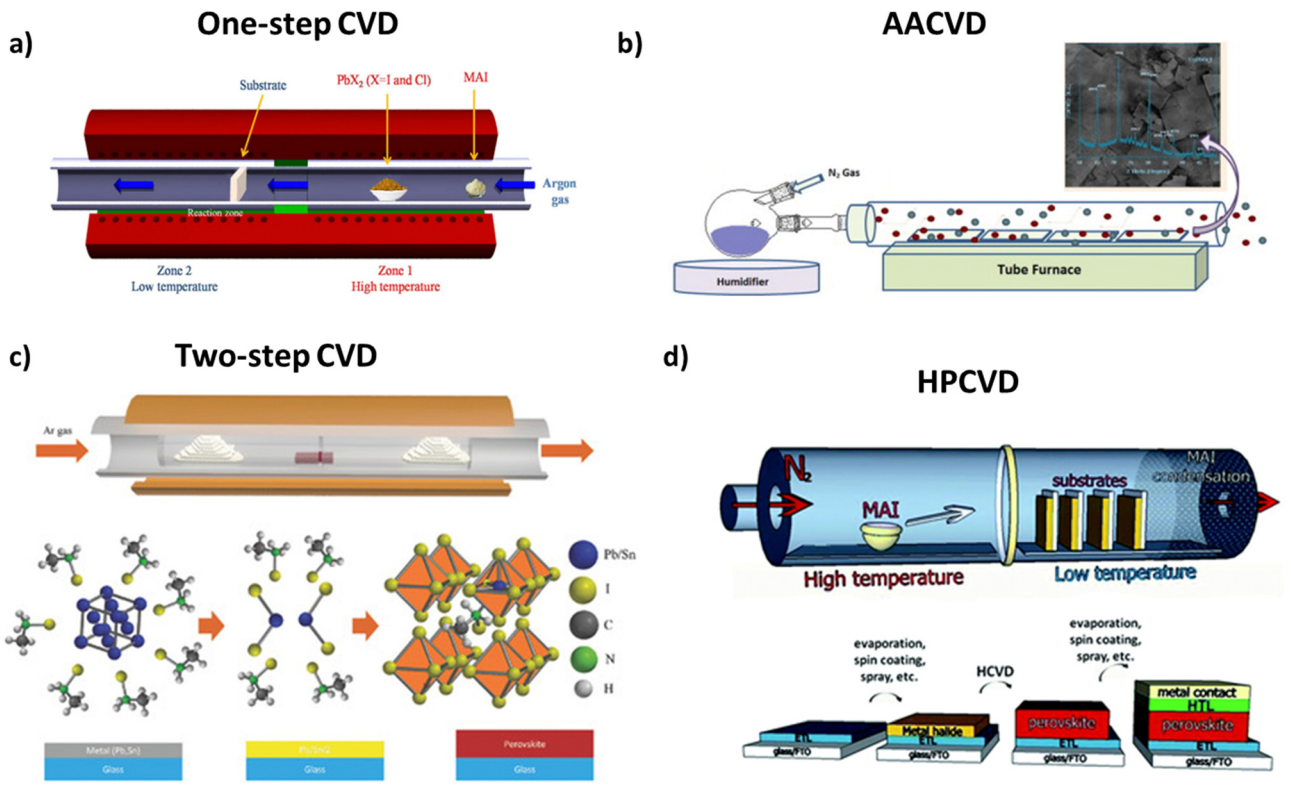

Fig. 7 (a) Schematics of the perovskite film fabrication using MAI and PbX_2 sources deposited onto a c-TiO_2-coated FTO glass substrate which is performed in a CVD furnace. Adapted with permission from ref. 111. (b) Schematics of the all-inorganic perovskite $CsPbBr_2I$ by an aerosol assisted CVD method. Adapted with permission from ref. 116. (c) Schematic of the CVD furnace and growth conditions of a perovskite film, and schematics of reaction details of the metal film with MAI, resulting in perovskite film formation. Adapted with permission from ref. 118. (d) Hybrid chemical vapor deposition based perovskite synthesis (top) diagram of the HPCVD furnace and MAI deposition onto metal halide seeded substrates. (Bottom) Layered structure of a complete solar cell fabricated by a HPCVD process. The complete solar cell is a glass substrate followed by a FTO layer, an electron transport layer, a perovskite layer, a hole transport layer, and a top metal contact. Adapted with permission from ref. 120.

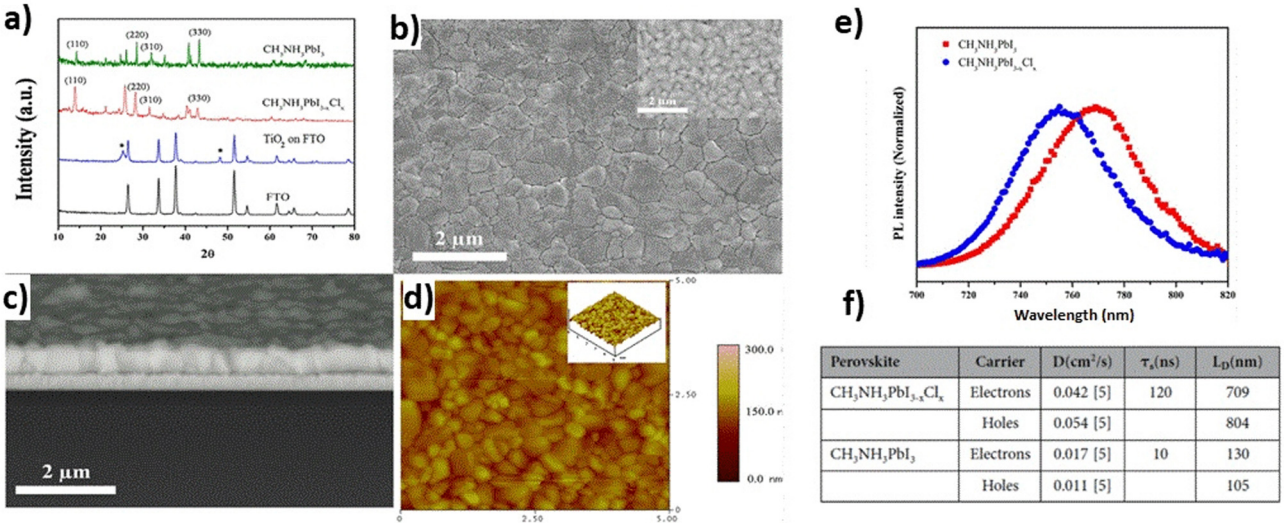

Perovskite	Carrier	D(cm²/s)	τ_r(ns)	L_D(nm)
$CH_3NH_3PbI_{3-x}Cl_x$	Electrons	0.042 [5]	120	709
	Holes	0.054 [5]		804
$CH_3NH_3PbI_3$	Electrons	0.017 [5]	10	130
	Holes	0.011 [5]		105

Fig. 8 Structural characterization of the perovskite films deposited on c-TiO_2-coated FTO substrates using the CVD method: (a) XRD patterns of FTO, the TiO_2 film on the FTO substrate (the peaks labeled with "*" are from TiO_2), $CH_3NH_3PbI_{3-x}Cl_x$ and $CH_3NH_3PbI_3$; (b) top-view secondary electron SEM image of a $CH_3NH_3PbI_{3-x}Cl_x$ layer, with an inset showing a backscattered electron (BSE) image with higher resolution; (c) cross-sectional BSE SEM image of a $CH_3NH_3PbI_{3-x}Cl_x$ layer; and (d) AFM height images (10 × 10 μm²), with an inset showing a 3D topographic image. (e) Photoluminescence spectra of lead halide perovskite films. (f) Carrier life-times and diffusion lengths of the perovskite films prepared by CVD which were derived from the time-resolved PL data. Adapted with permission from ref. 113.

3.1.3.1.1 Aerosol assisted CVD. In this variation of the aforementioned method, the precursor mixture of the main gas flow is in the form of an aerosol, which is later decomposed during the deposition. For this method to be applied, the solvents and moieties used should be relatively volatile, making this variation a plausible deposition method for large-area substrates.[115] This statement is also supported by the fact that AACVD takes place under ambient pressure, reducing the need for vacuum equipment. Unfortunately, perovskite solar cells fabricated through this method have shown low efficiency that originated mainly from the high surface roughness of the prepared perovskite film due to the large density changes during film formation.[110,117]

3.1.3.2 Two-step CVD. In the case of two-step deposition, each moiety is deposited separately on a substrate. At first, PbI_2 is transferred into the quartz tube and consequently onto the substrate. The PbI_2 coated substrate remains in the chamber, while a new flow of MAI vapor is injected, reacting with the already deposited thin film and thus forming the desired product. This allows the property tuning of each layer separately by gaining more control over the final film thickness and stoichiometry.

Two-step chemical vapor deposition can also be combined with the metal-alloying technique, in order to control better the film morphology. The team of Tavakoli *et al.*[118] suggested a solvent-free process, where Pb and Sn metals are evaporated separately, forming an alloy layer with controlled thickness on top of the substrate, with the MAI vapor being deposited on top of the alloy layer under vacuum conditions. The engineering process of the alloy composition enables the creation of a eutectic mixture which, in turn, enhances the quality of perovskite films through large-sized grains in the uniform film (Fig. 9).

3.1.3.2.1 Low-pressure CVD. A variation of two-step CVD employing milder conditions is low-pressure CVD, which is a slow solid–gas reaction. This method, promising for future scalability of perovskite optoelectronic devices, involves the deposition of a PbI_2 thin layer on top of the substrate through spin-coating. Subsequently, the covered substrate and CH_3NH_3I powder are placed at different positions and at different temperatures inside a tubular furnace. The two moieties react with each other and are finally annealed under ambient conditions. The derived films show strong absorption and satisfactory stability, while the method itself requires less energy consumption and more cost-friendly machinery.[112]

3.1.3.3 Hybrid physical–chemical vapor deposition (HPCVD). In the previous sections, we described the differences between thermal evaporation and chemical evaporation techniques. In some cases, however, there is a combination of both methods applied during the formation of organic–inorganic thin films through a hybrid chemical evaporation procedure. More specifically, thermal evaporation under high vacuum conditions is employed for the deposition of the metal halide, while the addition of the organic moiety on top of the already covered substrate through chemical vapor deposition follows. By all means, during the deposition steps, the substrate is maintained under low pressure and temperatures below 170 °C and the post-annealing steps take place under ambient conditions, for the deposition to be uniform and without any defects.[119] The advantage of this two-step fabrication would be control over the thickness and the uniformity of the film because of the vacuum thermal evaporation (VTE) process, as

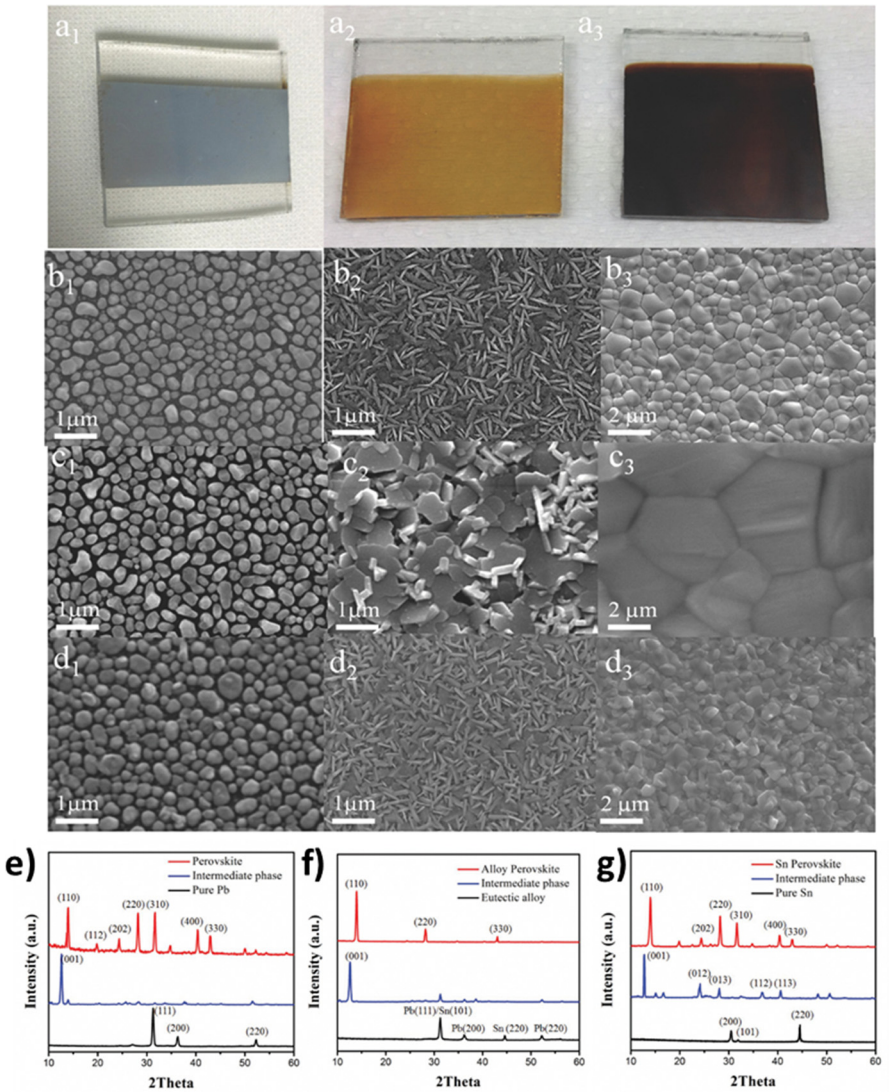

Fig. 9 Photographs of substrates after (a1) deposition of the metal alloy, and after reaction times of (a2) 20 min (intermediate SnI_2/PbI_2 phase) and (a3) 40 min (perovskite film). Top-view SEM images of the (b1) Pb metal, (c1) eutectic alloy film, and (d1) Sn metal; and intermediate phases for the (b2) Pb, (c2) eutectic alloy, and (d2) Sn formed after 20 min reaction time; and perovskite films for the (b3) Pb, (c3) eutectic alloy, and (d3) Sn after 40 min reaction time. X-Ray diffraction patterns of metal films, intermediate phases after 20 min reaction, and perovskite films formed by the reaction between the metal precursor and MAI after 40 min, for different metal precursors (e) pure Pb, (f) the eutectic alloy, and (g) pure Sn. Adapted with permission from ref. 118.

well as better nucleation and crystallization through the MAI moiety diffusion on top of the substrate on the gas phase.[120,121] Recently, crystalline $CsPbBr_3$ films were prepared with a two-step hybrid CVD process. In order to increase the quality of the perovskite films, the reaction temperature was set between 310and 360 °C.[122] The same conditions were also reported for the fabrication of scaled-up modules, with the economical aspect taken into consideration.[123] Qiu *et al.* demonstrated the fabrication of large area perovskite solar cells, where the FA-Cs mixed perovskite layer was deposited *via* a hybrid CVD process.[124] Upon increasing the area of the cell by a factor of 1000, a slight reduction of the device performance was obtained, suggesting that hybrid CVD is a promising method for scalable perovskite optoelectronic devices. Table 1 summarizes the electrical parameters of perovskite solar cells based on vacuum deposition methods for the preparation of the perovskite absorption layer.

3.2 Solution deposition approaches

In the early attempts, deposition was sufficiently accomplished in a single step using a common solution of PbI_2 and MAI precursors.[125] However, the lack of suitable solvents that can dissolve both components and the high perovskite reaction rate resulted in large morphological variations and therefore in large deviations in the achieved efficiencies. In 2013, Grätzel and co-workers described a sequential deposition method for the successful infiltration of the perovskite pigment within a porous TiO_2 film.[126] In particular, lead iodide (PbI_2) was first introduced *via* spin coating from solution into the nanoporous TiO_2 film and subsequently dipped into a solution of methyl

Table 1 Perovskite solar cell parameters based on vacuum deposition methods of perovskite layers

Method	Perovskite	J_{SC} (mA cm^{-2})	V_{OC} (V)	FF	PCE (%)	Ref.
Vapor-deposition	$MAPbI_{3-x}Cl_x$	21.5	1.07	0.67	15.4	94
Vapor-deposition	$MAPbI_3$	21.6	1.08	0.83	19.5	97
Physical vapor-deposition	$MAPbI_3$	19.47	0.932	0.60	10.9	98
Thermal evaporation	$MAPbI_3$	16.12	1.05	0.67	12.04	99
Co-evaporation	$MAPbI_3$	23.3	1.12	0.777	20.28	100
Sequential evaporation	$CsPbBr_3$	7.59	1.328	0.752	7.58	101
Sequential evaporation	$CH_3NH_3PbI_{3-x}Cl_x$	20.89	1.02	0.722	15.4	102
Vacuum deposition	$Cs_{0.15}FA_{0.85}PbI_3$	24.88	1.11	0.772	21.32	104
Pulsed laser deposition	$CH_3NH_3PbI_{3-x}Cl_x$	—	—	—	7.7	107
Pulsed laser deposition	$MAPbI_3$	—	—	—	1.12	109
LPCVD	$MAPbI_3$	21.7	0.91	0.645	12.73	112
One-step CVD	$CH_3NH_3PbI_{3-x}Cl_x$	18	0.97	0.64	11.1	113
One-step CVD	$MAPbI_3$	15.9	0.95	0.61	9.2	113
AACVD	$MAPbI_3$	16.1	0.77	0.44	5.42	117
CVD	$MAPb_xSn_{1-x}I_3$	25.5	0.796	0.692	14.04	118
Hybrid evaporation	$MAPbI_3$	13.14	1.029	0.4267	5.77	119
Hybrid CVD	$CH_3NH_3PbI_{3-x}Cl_x$	19.1	0.92	0.62	10.8	120
HPCVD	$MAPbI_3$	18.58	1.00	0.66	12.3	121
Hybrid CVD	$CsPbBr_3$	4.85	1.39	0.65	4.41	122
LPHCVD	$MAPbI_3$	18.20	0.991	0.72	13.52	123
HCVD	$Cs_{0.1}FA_{0.9}PbI_{2.9}Br_{0.1}$	20.2	0.90	0.67	12.3	124

ammonium iodide (MAI) to synthesize the resultant $MAPbI_3$ perovskite film. It was found that the conversion to the perovskite occurred within the nanoporous oxide as soon as the two precursors came into contact, hence allowing for better control over the morphology and reproducibility of perovskite films. As a result, solid-state mesoscopic perovskite solar cells with a high efficiency of 15% were obtained, thus providing new opportunities for the fabrication of solution-processed mesoscopic PSCs. However, this method is not very convenient for the preparation of planar devices because it often results in films with significant surface roughness that frequently peel off from the substrate.[127]

3.2.1 Spin-coating. The most widely used technique for the fabrication of perovskite optoelectronic devices on the laboratory scale is spin-coating. It can be either a one-step or two-step deposition method that is characterized as a solution-processing based one. The main advantages of this method are its simplicity and its low cost.

3.2.1.1 One step spin-coating. During the one-step process, organic halides along with metal halides are mixed with an appropriate solvent, forming the precursor solution. Mostly aprotic polar solvents, such as *N*,*N*-dimethylformamide (DMF), dimethyl sulfoxide (DMSO), γ-butyrolactone (GBL), 2-methoxyethanol (2-ME) and acetonitrile (ACN), are used, which exhibit high boiling point and low vapor pressure when at room temperature.[128] The solution formed is subsequently deposited on the substrate surface on top of the electron transport layer in standard architecture solar cells. This substrate is placed on a spin-coater and spun at high rotational speeds for a couple of seconds so that the excess solvent evaporates. During the evaporation, the creation of the perovskite layers takes place, with crystals being formed and grown due to the ionic interaction between metal cations and halogen anions.[129] The substrate is finally annealed at a temperature between 80 and 150 °C for 10 minutes to 2 hours, so that the remaining solvent is removed.[130] A similar technique to this is hot casting, during which the mixture of the organic and inorganic solutes is first heated at 70 °C and subsequently deposited on an already heated substrate at 180 °C. The substrate is then put in a spin-coater and finally annealed on a hot plate, which leads to the development of millimeter-scale crystallites.[131]

Even though this method may appear to be quite simple, there are some problems found within it. The uniformity of the perovskite layer, crucial to its light harvesting properties, is dependent on factors such as annealing conditions. As reported by Wang *et al.*,[132] fast crystallization due to accelerated solvent evaporation leads to incomplete pore filling, while Li *et al.*[133] suggested that low-volatile organic components need higher temperatures to be driven out, thus creating defects in the film. A solution to this problem would be a solvent-induced crystallization method, in which a second solvent is added to the substrate before the annealing step so as to induce the nucleation process, resulting in the formation of large crystals.[134] However, even if such a methodology is employed, the thickness of the film and the possible grain boundaries should be taken into consideration with a more elaborate method being employed.[129]

3.2.1.2 Two-step spin-coating. To overcome the aforementioned defects, a two-step spin-coating method is proposed as a better alternative. The metal halide mixed with the appropriate solvent, usually DMF, is first deposited on the bottom electrode material and subsequently subjected to spin-coating followed by annealing under the conditions mentioned above. In the next step, the organic halide moiety is dissolved in a solvent, where the organic halide exhibits low solubility and is deposited on top of the dried metal halide layer. Then the already prepared metal halide film is placed on the spin-coater and thermally annealed in a similar fashion. In this way, the first layer is converted into the desirable perovskite film. The morphology of the final film can be adjusted by the

manipulation of spinning speed and deposition time.[133,134] Fig. 10a illustrates the one-step and two-step coating procedures of $CH_3NH_3PbI_3$ on mesoporous TiO_2 substrates. In the two-step deposition, the perovskite film fills the TiO_2 pores, resulting in a void-free $CH_3NH_3PbI_3$ layer, while in the one-step deposition the formation of perovskite islands is clearly seen (Fig. 10b and c).

The two-step method has also been proved to solve the hysteresis effect in a planar device, since the homogeneity of the film minimizes the existence of defects and charge traps. Moreover, it is more cost effective in terms of materials than the one-step deposition method, since the quantity of the second solution is adjusted according to the concentration of the metal halide solution. Thus, the thickness of the second deposited film depends on the thickness of the first one, which supports their immediate reaction upon contact.[135,136]

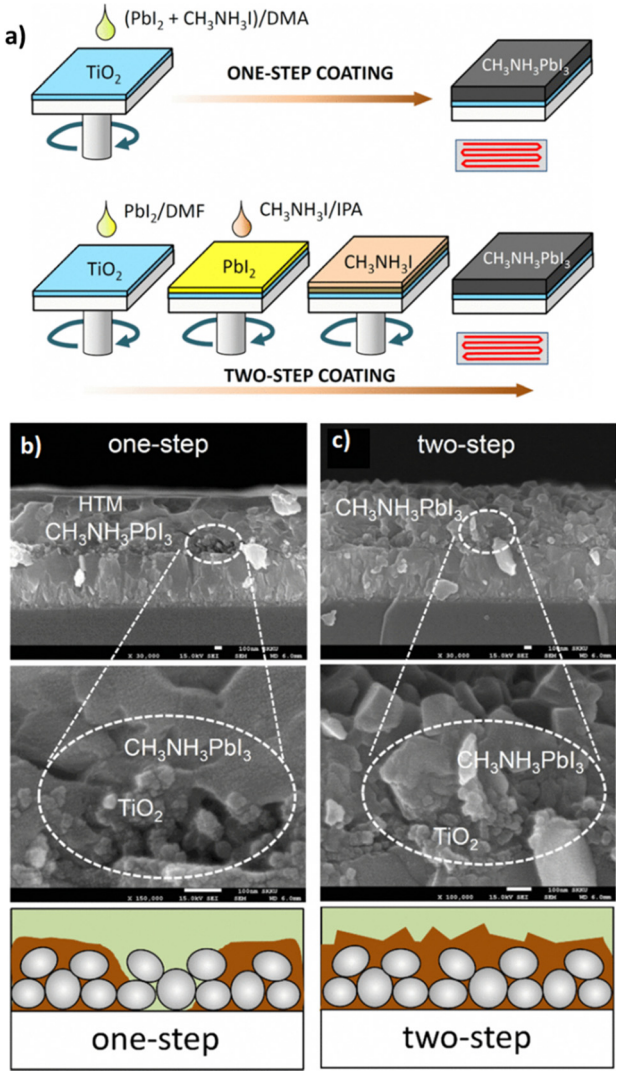

Fig. 10 (a) One-step and two-step spin-coating procedures for $CH_3NH_3PbI_3$ formation. PbI_2 was mixed with CH_3NH_3I in *N,N*-dimethylacetamide (DMA), which was spin-coated and heated for one-step coating. For two-step coating, a PbI_2-dissolved *N,N*-dimethylformamide (DMF) solution was first spin-coated on the substrate, dried and then a CH_3NH_3I-dissolved isopropyl alcohol (IPA) solution was spin-coated on the PbI_2 coated substrate. Cross-sectional SEM images of (b) one-step deposition of $CH_3NH_3PbI_3$ and (c) two-step deposition of $CH_3NH_3PbI_3$. One-step deposition leads to imperfect pore-filling as shown in the high magnification SEM image. Two-step deposition results in the pores of the TiO_2 layer being fully filled with $CH_3NH_3PbI_3$ as confirmed by the void-free $CH_3NH_3PbI_3$ layer. Adapted with permission from ref. 135.

3.2.2 Drop-casting. Drop-casting can be characterized as the simplest technique for perovskite film deposition. Along with spin coating, its main advantages lie in its low cost and easy execution. During this method, the perovskite solution containing both the organic and the inorganic moieties is deposited into a substrate with the help of a pipette. This is followed by heating the substrate in a hotplate so that the solvent can be evaporated, thus forming the film. Nonetheless, the thickness of the perovskite film as well as its optoelectrical properties are dependent on the concentration of the solution, its viscosity and the rate of evaporation of the solvent while on the substrate, since no spinning is performed.[137] Compared to the spin-coating procedure, perovskite films formed by drop-casting show improved film quality and uniformity without pinholes.[138] More importantly, the growth of perovskite crystals prepared by drop-casting is significantly affected by the temperature during film preparation. It is shown that $MAPbI_3$ presented a (110) orientation when low temperature (60 °C) was applied to the prepared perovskite film. On the other hand, at high temperatures (>120 °C) the $MAPbI_3$ crystals were (200) oriented, demonstrating that this different orientation resulted in a different perovskite film morphology with needle-like and ground grains, respectively.[139] Zuo and Ding also showed that the solar cells based on the drop-casting perovskite films exhibited high performance under a high relative humidity of 88% attributed to the prevention of water invasion in the $MAPbI_3$ layer through a surrounding solvent vapor that protected the prepared film during its formation. Recently, all-inorganic and lead-free perovskite films were prepared by the drop-casting method; they exhibited highly-crystalline phase-pure layers under a low-temperature process. When the corresponding all-inorganic $CsPbBr_3$ film was employed in photodetectors, an improved device performance with higher responsivity compared to spin-coated film devices was demonstrated.[140]

This deposition method was also used for the creation of larger-scale perovskite thin films. Mei *et al.*[141] reported the creation of a TiO_2/ZrO_2 scaffold in which the perovskite solution could enter through drop casting. This solution, containing PbI_2, CH_3NH_3I, 5-ammonium valeric acid iodide (5-AVAI) and γ-butyrolactone as a solvent, led to the creation of a perovskite with stoichiometry $(5\text{-AVA})_x(MA)_{1-x}PbI_3$. This ameliorated the contact with the TiO_2, so as to create a layer with fewer defects, enhanced performance and promising reproducibility on a 10 cm × 10 cm substrate. This type of device structure, employing carbon as a back contact, seems also to have enhanced stability under continuous illumination under outdoor conditions.[142] In a recent work, 2DRP perovskite films were prepared by using the drop-casting method without any

further processing step such as antisolvent treatment or inert-gas blowing. For large-scale perovskite solar cell fabrication, a slot-die coating system was used to deposit a homogeneous and compact perovskite film on a 25 mm × 25 mm PET/ITO/PEDOT:PSS substrate. The fabricated device achieved a power conversion efficiency of 8.8%, which was lower compared with that based on a perovskite film drop-cast on a glass/ITO/PEDOT:PSS substrate due to the higher sheet resistance of the PET/ITO.[143]

3.2.3 Vapor-assisted solution process. So far, it has become clear that vacuum and solution processes constitute two dominant fabrication techniques for perovskite films. Nevertheless, although vacuum-based environment processes where the inorganic and organic compounds (*i.e.* PbX_2 and MAX, respectively) serve as the vapor source provide high quality films with respectable features, they also lead to time consuming deposition steps and costlier equipment. On the other hand, while the fabrication of a perovskite film *via* any solution coating process appears to be an alternative approach due to the simple concept that both materials can rapidly form from their solution phase reaction after annealing, undesired pinholes may occur across the whole film.[144,145] Thus, a different deposition technique is developed called the vapor-assisted solution process (VASP) that combines the advantageous characteristics of both processes.[146] The VASP is considered to be a modified two-step sequential solution deposition process in which the second step is replaced with a gas-phase reaction.

According to this technique, the evolution of the film starts with the construction of the inorganic framework of the perovskite material by a solution process, and subsequently an *in situ* reaction between the inorganic species and the desired organic vapors takes place, forming the perovskite film.[147] A crucial factor to the formation of the film is the source temperature that creates the appropriate vapor pressure so as not to damage or decompose the gaseous halide salts completely. The substrate temperature will also affect the dynamics of the perovskite formation. In other words, the VASP exploits the kinetic reactivity of the organic vapor and the thermodynamic stability of the perovskite during the *in situ* growth process. Hence, the advantage that this technique has over pure vacuum and solution processing is the intercalation of the organic components into the inorganic framework through vapor, as it prevents the high growth rate of the perovskite material during the co-deposition of precursors and the degradation of the latter upon dipping the inorganic framework into an organic solution. In sum, the VASP can provide perovskite films with full substrate coverage, small surface roughness and well-defined grain sizes up to the microscale. Chen *et al.*[147] reported the formation of $CH_3NH_3PbI_3$ ($MAPbI_3$) films on mesoporous TiO_2 by means of a vapor-assisted solution method for use in solar cells. The cross-sectional SEM images showed that the VASP fabricated $MAPbI_3$ films exhibited a continuous capping layer with a flat surface, yielding better optical and electrical properties and hence higher power conversion efficiency as compared to solution deposited perovskite films (Fig. 11a). In addition, Sedighi *et al.*[148] employed the VASP approach to prepare mixed halide perovskites ($CH_3NH_3PbI_{3-x}X_x$) in an ambient atmosphere for solar cell fabrication, as well. The perovskite films were synthesized by exposing PbI_2 to CH_3NH_3X (where X = I, Br, or Cl) vapor. The final films exhibited good crystallization (Fig. 11b), particularly $CH_3NH_3PbI_3$, while the inclusion of chlorine and bromine into the perovskite lattice led not only to lower temperature and shorter reaction time but also to smaller grains (Fig. 11c–e) and surface roughness.

Recently, high-performance perovskite solar cells with PCEs of ~21% were demonstrated using methylammonium chloride (MACl) vapor in order to improve the quality of the $MAPbI_3$ layer and increase its grain size.[149] In another work, solar devices with a planar structure of fluorine-doped tin oxide (FTO)/compact-TiO_2/C_{60}/$(FA)_x(MA)_{1-x}PbI_3$/spiro-OMeTAD/Au with different MA:FA mixed cation ratios were fabricated by Chen *et al.*[150] The formation of the mixed perovskite films was achieved by heating the PbI_2 coated substrates with the FAI and MAI powders uniformly applied around them at 170 °C for 30 min under low vacuum. Their best planar device revealed a PCE of 16.48%. Furthermore, 2D/3D mixed perovskite films were developed using a low-pressure VASP, where phenylethylammonium iodide (PEAI) was added in PbI_2 and then the prepared film was reacted with methylamine ($CH_3NH_{2(g)}$ and $MA_{(g)}$ vapors).[151] It was demonstrated that the 3D $MAPbI_3$ perovskite was formed on the surface of multiple 2D RP perovskite layers of $PEA_2MA_{n-1}Pb_nX3_{n+1}$ with different *n* values, suggesting a vertical-gradient phase distribution, which could be effectively applied in perovskite optoelectronic devices. Moreover, quasi-2D $PEA_2(FAPbBr_3)_{n-1}PbBr_4$ films prepared through the VASP were incorporated in perovskite light-emitting diodes, exhibiting not only high luminance and external quantum efficiency, but also good reproducibility.[152] In a moderate concentration DMSO-vapor environment, a smooth perovskite film with uniformly distributed nanograins was formed, showing an enhanced photoluminescence quantum yield and quenched nonradiative recombination. DMSO-vapor also plays a crucial role in the crystallinity and growth of the perovskite film in order to form a high-quality and pin-hole free perovskite layer. Shadabroo *et al.*[153] showed that DMSO vapor-annealing treatment of Cs_2AgBiB_6 was beneficial to the performance of Pb-free all-inorganic perovskite solar cells.

3.2.4 Hydrothermal synthesis. The term ''hydrothermal'' is historically rooted in earth science during the middle of the nineteenth century, where it was used to describe the formation of minerals by hot water when magma cooled. On this basis, hydrothermal synthesis emerged as a frontline technology for single crystal growth[154] and metal leaching.[155] Since then, extensive research has been performed regarding the synthesis of new materials *via* the hydrothermal route and the understanding of the reaction mechanism focusing mainly on the reactivity of the reactants, regularities of synthetic reactions and conditions, and their effect on the structure and properties of the final products.[156]

Today, hydrothermal synthesis refers to the synthesis of substances by chemical reactions in a sealed heated aqueous solution at appropriate temperature (100–1000 °C) and pressure

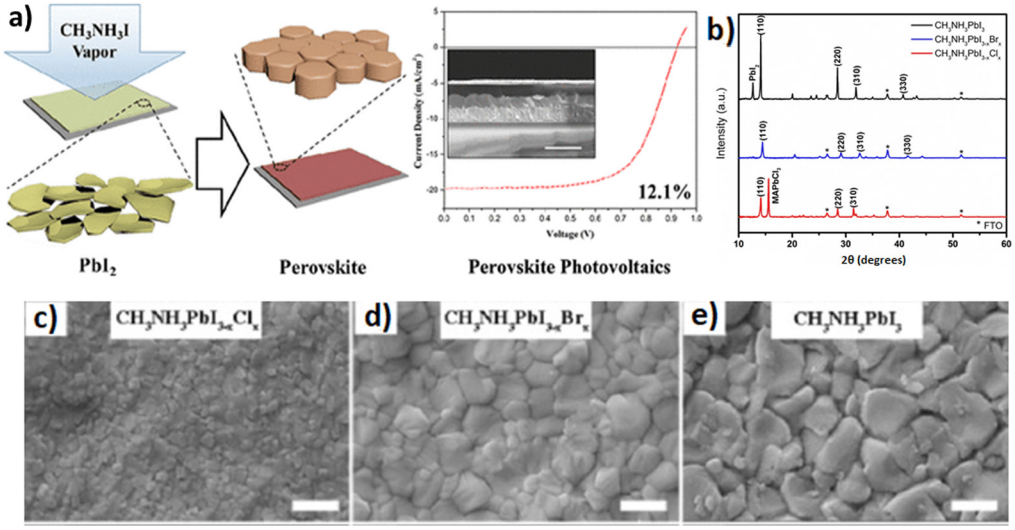

Fig. 11 (a) Schematic illustration of perovskite film formation through a vapor-assisted solution process. Adapted with permission from ref. 147. (b) XRD patterns for films of $CH_3NH_3PbI_3$, $CH_3NH_3PbI_{3-x}Br_x$, and $CH_3NH_3PbI_{3-x}Cl_x$ deposited by the VASP method. FTO = fluorine-doped tin oxide. SEM surface images of (c) $CH_3NH_3PbI_{3-x}Cl_x$, (d) $CH_3NH_3PbI_{3-x}Br_x$, and (e) $CH_3NH_3PbI_3$ deposited by the VASP method. Scale bars are 500 nm. Adapted with permission from ref. 148.

(1–100 MPa).[155,156] According to reaction temperature, hydrothermal synthesis is classified into two categories: subcritical and supercritical synthesis reactions. A subcritical synthesis reaction is carried out in the temperature range of 100–240 °C, while a supercritical synthesis reaction occurs at much higher temperatures. In addition, according to the vapor pressure of the main composition in the reaction, either low-pressure or high-pressure conditions can be employed to control the morphological features of the as-made materials. The uniqueness of this technique stems from the fact that any stable precursor used in the process can break at relatively low temperature, thus preventing the extensive agglomeration that solid-state reactions generally cause at high sintering temperature. Consequently, other problems encountered with high-temperature processes, like poor stoichiometry control due to the volatilization of components, can be avoided. Moreover, another factor that distinguishes hydrothermal synthesis from other conventional synthesis methods is that it is a rather environmentally benign method which may be attributed, apart from the low processing temperatures, to the absence of milling and the ability to recycle or dispose waste that cannot be recycled.[157]

Nowadays, hydrothermal synthesis is linked to several interdisciplinary branches of science, favoring the preparation of numerous advanced materials[158] including perovskites.[159] Given the fact that hydrothermal synthesis permits rapid mixing of precursors for homogeneous products with controllable parameters, it has become one of the most preferable and adaptable chemical routes to prepare homogeneous perovskite films. In 2012, the Peng group[160] first demonstrated the synthesis of $CH_3NH_3PbBr_3$ and $CH_3NH_3PbI_3$ by mixing lead acetate with HI/HBr solution and methylamine alcohol solution and then heated at 150 °C in an oven for 1–12 h. The hydrothermally grown microcrystals were used as the active material in Li-ion batteries, presenting a discharge capacity of 331.8 mA h g^{-1} (at a current density of 200 mA g^{-1}). Fig. 12a–c shows the SEM image and the corresponding EDX spectrum of the hydrothermally prepared $CH_3NH_3PbBr_3$ along with the cycling performance of the Li-ion batteries based on the $CH_3NH_3PbI_3$ and $CH_3NH_3PbBr_3$ perovskites. Mahmood *et al.*[161] reported the synthesis of lead iodide (PbI_2) micro-needles using a hydrothermal method in the presence of surfactant cetyltrimethylammonium bromide (CTAB) at a low temperature of 100 °C for 8 h. Highly crystalline $MAPbI_3$ micro-needles were produced by covering the surface of PbI_2 micro-needles using an isopropanol solution of CH_3NH_3I (MAI) that resulted in a pin-hole free perovskite solar cell yielding a PCE of 17.98%, as shown in Fig. 12d. All-inorganic based cesium lead-halide ($CsPbX_3$) was also synthesized by a hydrothermal method.[162] In particular, $CsPbI_3$ and $CsPb_2Br_5$ powders were hydrothermally prepared and then deposited *via* a spin-step spin-coating method to form the active layer of perovskite solar cells. Hydrothermally developed $CsPbI_3$ and $CsPb_2Br_5$ crystals formed highly crystalline nanowires and nanorods, respectively, as shown in SEM images of Fig. 12e and f. Both δ-$CsPbI_3$ and tetragonal $CsPb_2Br_5$ nanostructures were PL active with unique optical properties, suggesting their successful use in Cs-based perovskite optoelectronic devices.[162]

3.2.5 Solvothermal synthesis. Like hydrothermal synthesis, solvothermal synthesis is a solution reaction-based procedure. The difference between the two techniques is that instead of water, in the solvothermal synthesis the primary solvent is usually an organic one. The implementation of solvothermal synthesis, whereby an often homogeneous mixture of liquid and solid precursors is heated in a sealed reaction vessel close to or above the boiling point of the main solvent, is particularly well known for the preparation of crystalline materials. In

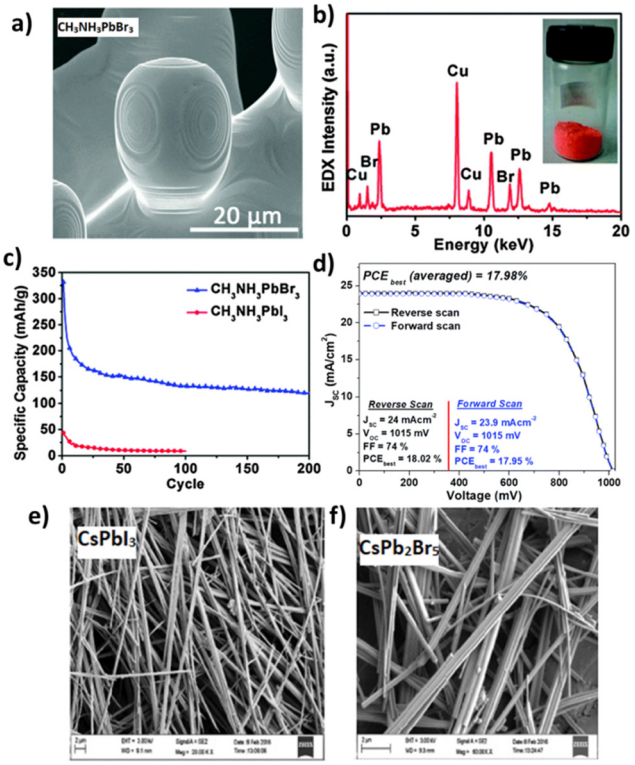

Fig. 12 (a) SEM image of hydrothermally synthesized $CH_3NH_3PbBr_3$ and (b) the corresponding EDX spectrum with the photograph of $CH_3NH_3PbBr_3$ inset. (c) Cycling performances of the Li-ion batteries made of perovskite $CH_3NH_3PbBr_3$ and $CH_3NH_3PbI_3$. Adapted with permission from ref. 160. (d) *J*–*V* curves (in both the forward and reverse scans) for the best-performing device with $MAPbI_3$ micro-needles. Adapted with permission from ref. 161. FE-SEM images of (e) high quality yellow phase $CsPbI_3$ nanowires and (f) highly crystalline $CsPb_2Br_5$ nanorods. Adapted with permission from ref. 162.

general, the production of materials of specific form with certain physical properties of well-defined structures would traditionally require high-temperature solid-state reactions for long periods of time often combined with pressure and controlled gas atmospheres to ensure homogeneous mixing of the precursors used.[155] Rationally, solid-state chemists have endeavored to find an alternative synthesis approach to master the difficulties of acquiring homogeneous mixing of solid precursors under milder reaction conditions using soft chemistry and being able at the same time to gain control over the crystal form (particle size and phases).[163] Among several soft chemical routes to synthesis proposed, solvothermal synthesis appears to be the most appealing one. In other words, solvothermal synthesis constitutes a versatile alternative to calcination for developing at milder temperatures inorganic solids[164] and, most recently, metal–organic framework structures.[165] To date, hydrothermal synthesis has been fine-tuned for the synthesis of industrially applicable solid materials[166,167] and especially quartz[164] from mimicking the synthesis of natural minerals to a varying synthesis of advanced materials, highly documented in the literature.[152]

Unfortunately, there has been little research related to one-step preparation of mixed-metal oxides *via* the solvothermal method.[168,169] These functional materials, having provided the momentum for a large number of technological applications, usually contain one or more transition-metal elements, whose oxidation states are pivotal in dictating their underlying properties (*i.e.* electronic, magnetic or redox properties).[170] Perovskites containing transition metals exhibit constructive properties derived from the control of certain oxidation states. Nevertheless, controlling crystal morphology in terms of particle shape and size is also crucial for the use of solvothermal synthesis. Lately, a number of studies have demonstrated the benefit of solution-mediated crystallization of multinary oxides containing metals whose oxides are volatile, which can be prevented without affecting the stoichiometry of the precursors. In most of the cases, it has been shown that the crystallization of materials could be attained by the use of solvents.[162] The solvent medium is linked to the solubility of the reactants and, apart from its contribution to the nucleation process by bringing the precursors, it may lead to the crystallization of the final product without the need for high concentrations of hydroxide salts. In this regard, apt selection of the precursor composition and reaction conditions can result in very homogeneous particles with a narrow size distribution.[171,172] Crystalline $CH_3NH_3PbI_3$ was prepared *via* a solvothermal method for the first time in 2015, where the crystal growth depended on the temperature and reaction time.[173] Recently, all-inorganic perovskites have also been solvothermally synthesized. Zhai *et al.*[174] showed that by modifying the solvothermal reaction sources, the versatility of perovskite crystal structure could occur, demonstrating phase transformation from cubic $CsPbBr_3$ nanoplatelets to rhombohedral Cs_4PbBr_6 nanocrystals, and *vice versa*. The solvothermal method was also proved as a successful procedure for Mn-doped $CsPbX_3$ perovskite quantum dots and nanoplatelets. It was shown that controllable solvothermal reaction conditions and most importantly the Cs-to-Pb feeding ratio were crucial to the perovskite preparation.[175,176] Furthermore, high-quality $CsPbX_3$ nanowires prepared by the solvothermal method exhibited good crystallinity and a high photoluminescence quantum yield. Consequently, the incorporation of $CsPbI_3$ in photodetectors was beneficial to the device performance, achieving fast light response speed and a high switching ratio.[177]

Moreover, self-assembled $CsPbBr_3$ nanowires prepared by a two-step solvothermal procedure and a direct-dripping method showed unique polarization characteristics.[178] Interestingly, excitation polarization-dependent emission was demonstrated, attributed to the anisotropic charge distribution of the perovskite nanowires. More recently, a new approach to solvothermal preparation of $CsPbBr_3$ nanowires was demonstrated, using short-chain ligand engineering in order to improve the photoelectric properties of the perovskite. The prepared nanowires exhibited excellent uniformity, a good photoluminescence lifetime and high mobility.[179]

3.2.6 Ultrasound-assisted synthesis. Ultrasound-assisted synthesis, also known as ultrasonication, is considered to be a green synthetic route widely employed for the acceleration of various organic reactions which would conventionally require

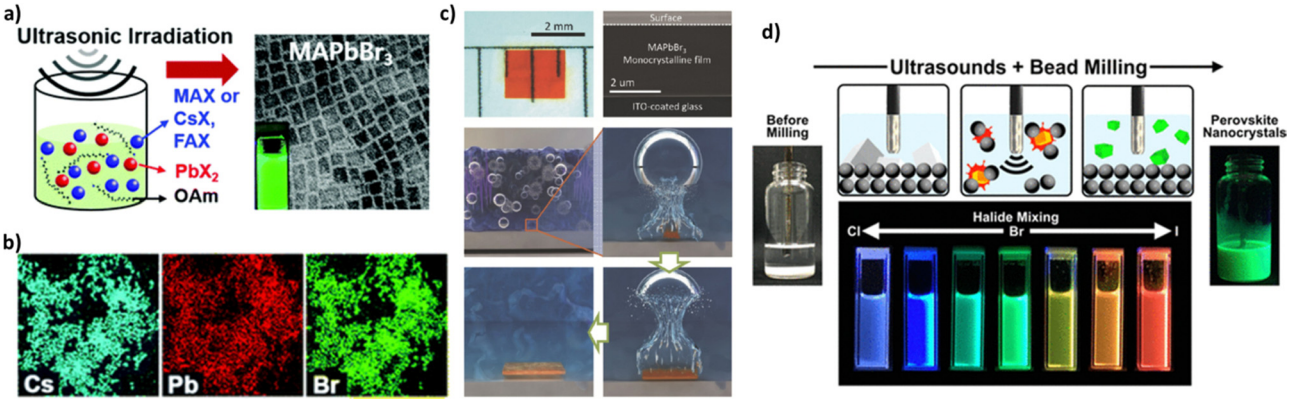

Fig. 13 (a) Ultrasound-induced synthesis of $APbX_3$ perovskite nanocrystals with a wide range of compositions, where A = CH_3NH_3, Cs, or HN=$CHNH_3$ (formamidinium), and X = Cl, Br, or I. (b) EDX maps showing homogeneous distributions of Cs, Pb, and Br in $CsPbBr_3$ NCs. Adapted with permission from ref. 186. (c) Optical image of the monocrystalline film (left). Cross-sectional SEM image of a freshly cut monocrystalline film (right). Illustrations of the CTAC mechanism on a microscopic scale. Adapted with permission from ref. 187. (d) Schematic illustration of the ultrasound-assisted bead milling (top) and photograph under a UV lamp of the colloidal halide-mixed perovskite nanocrystals. Adapted with permission from ref. 189.

not only long reaction times but also toxic and costly precursors, possibly resulting in poor yields along with expensive products.[180] Ultrasonically induced and intensified reactions provide an easier and more sustainable synthetic methodology for the preparation of various nanostructured[183] as well as light-activated materials[181–184] that usually cannot be manufactured by traditional techniques. The application of ultrasound-assisted synthesis is based on the cavitation phenomenon whereby the formation of small vapor-filled cavities in a liquid–solid phase occurs when it is subjected to extreme conditions of pressure and temperature.[185] The crystallization procedure is affected and governed by the ultrasonic treatment, yielding controllable size properties of the single crystalline nanoparticles. Recently, the research community has managed multiple types of ultrasonically assisted perovskite crystal growth. Jang *et al.*[186] reported the successful ultrasound-assisted synthesis of lead halide perovskite nanocrystals (Fig. 13a and b) used for the fabrication of high-sensitivity photodetectors. $APbX_3$ perovskite nanocrystals with different compositions (where A = CH_3NH_3, Cs, or HNQCHNH$_3$ (formamidinium), and X = Cl, Br, or I) exhibited uniform plate-type morphologies with an average size of 10 nm. Ultrasonic irradiation accelerated the dissolution of the precursors (AX and PbX_2) in toluene, which determined the growth rate of the nanocrystals.

Peng *et al.*[187] used ultrasonication to grow $CH_3NH_3PbBr_3$ ($MAPbBr_3$) monocrystalline films of various thicknesses for perovskite solar cells. By exploiting the perovskite's tendency to crystallize in solution, they designed a novel growth method termed cavitation-triggered asymmetrical crystallization (CTAC) to aid heterogeneous nucleation *via* the introduction of a very short ultrasonic pulse ($\approx$1 s) into the solution when it reached a low supersaturation level, thus overcoming the limitations of conventional single-crystal growth techniques due to their propensity to create solely free-standing perovskite single crystals. At high supersaturation levels, cavitation triggered immoderate nucleation and thus the growth of numerous small-scale crystals. Fig. 13c shows an optical image and a cross-sectional SEM image of the monocrystalline film (left and right, respectively). Lately, ultrasound assisted synthesis was used to prepare high-quality perovskite quantum dots (QDs).

Chen *et al.*[188] presented in their research work that ultrasonic irradiation, apart from its use in accelerating the precipitation of perovskite quantum dots, contributed to the crystallization process of QDs providing particles of smaller sizes with a narrower size distribution. They also prepared perovskite quantum dots with different chemical compositions that led to an immensely wide color gamut. In addition, the photoluminescence peak intensity can be controlled by adjusting the halide component in the perovskite precursor through an ultrasound-assisted bead milling method (UBM).[189] Fig. 13d illustrates the perovskite $MAPbBr_3$ QD preparation and the different colors emitted under UV irradiation. Purification of red-emissive $MAPbI_3$ QDs prepared by UBM using different carboxylate esters resulted in minimizing the particle size distribution and thus improving the optical properties of perovskite QDs. When purified $MAPbI_3$ QDs were incorporated in light emitting devices, an excellent external quantum efficiency was obtained.[190]

3.2.7 Microwave-assisted synthesis. Another green synthetic technique, besides ultrasound-assisted synthesis, used for the activation and acceleration of organic reactions is microwave-assisted synthesis.[191] While originally used merely in organic synthesis, this technology has taken a new dimension experiencing exponential growth both in industry and in academia in recent years and is continuously refined with new and innovative applications in materials science,[192] nanotechnology[193] and further disciplinary areas of science.[194] In general, microwave chemistry is based on the utilization of microwave irradiation to heat matter or to introduce energy into a system by dielectric heating. By extension, microwave-assisted synthesis consists of the conversion of electrical energy delivered to a substance through electromagnetic waves into kinetic energy by dielectric heating. Kinetic energy is eventually

converted into heat that will uniformly and rapidly be distributed throughout the reaction mixture. The efficiency of this process relies on the susceptibility of the irradiated substance (*e.g.* solvent and/or precursors) to absorb the microwave energy of appropriate wavelength and subsequently induce heating that drives chemical reactions. In order for this to happen, the specific substance must have a dipole-moment and/or ionic conductivity. Gedye *et al.*[195] and Giguere *et al.*[196] were the first to demonstrate the effect of microwave warming on accelerating organic chemical transformations. The major advantage of microwave heating, compared to other heating strategies, is that it does not require external heating sources such as oil-bath systems or electric heaters. The differentiating feature of microwaves from other forms of irradiation like X- and γ-rays is their non-ionizing nature, and thus, no change in the molecular structure of the material being heated occurs, only thermal activation occurs.

One of the most effective ways to form better crystals is by temperature tuning. Several approaches of synthetic protocols have been proposed for hybrid perovskites ranging from two-step processes to direct crystallization.[26,197,198] Although perovskites have the merit of being deposited from their precursors into a thin film by solution-based processes, it is rather difficult to gain control over the nucleation and crystallization of the as-prepared film from a saturated solution by evaporation of the solvent. The procedure of crystallization is affected by a number of variables like an oxygen-rich atmosphere and humidity that may cause a compounding effect of crystal sizes and surface chemistries.[199] Both chemical and physical properties can be adjusted at the atomic level *via* the use of reactants and thermal annealing. The most popular procedure to initiate crystallization of perovskite films is thermal annealing at 100 °C for 10 min. Thereafter, different thermal annealing processes have been reported such as high-temperature thermal annealing,[200] multistep thermal annealing[201] and laser induced thermal annealing.[202] However, aside from the aforementioned thermal annealing processes, it has been shown that the microwave irradiation process can lead to a faster crystallization of the perovskite material requiring less energy.[203] In fact, the implementation of microwave irradiation as a thermal initiator can lead to the crystallization of the perovskite material within few minutes, thus making microwave assisted synthesis one of the most promising synthetic routes towards the generation of hybrid perovskites. During optimization experiments, it has been found that the applied microwave power is pivotal to both crystallinity and device efficiency.[204] Tuning the irradiation time changes not only the crystallization of the synthesized perovskite, but also the photoluminescence emission and quantum yield.[205] However, prolonged exposure to microwave irradiation will lead to the opposite result. Another factor that plays a crucial role in the preparation of perovskites under microwave irradiation is the solvent. In order to point out how critical the effect of solvents is on perovskite materials, Cao *et al.*[198] mixed PbI_2–CH_3NH_3I adducts with different solvents, including DMF, DMSO and diethyl ether. It was noticed that while the adducts added to DMF or DMSO would turn black when irradiated, the mixed PbI_2–CH_3NH_3I added to diethyl ether did not change to black, indicating that the latter could not absorb the radiation and convert it into heat. The change in the color of the mixed PbI_2–CH_3NH_3I added to DMF or DMSO suggested that the solvents could absorb energy, convert it into heat and thus accelerate the perovskite precursors to react at the atomic level and crystallize. In fact, according to their research, the grain size of perovskite films revealed a trend of linear increase between the time of microwave treatment and different time intervals.

3.2.8 Solid-state reaction-based methods. Methods based on solid-state reactions have been developed to solve some of the problems arising during the two-step dipping method, where PbI_2 films are dipped in CH_3NH_3I solution to form $CH_3NH_3PbI_3$ perovskite. These problems include the incomplete conversion of PbI_2 precursor salt into the perovskite and the lack of control concerning the grain morphology.[206] The principle of the solid-state method, also characterized as a direct contact and intercalation process (DCIP), is that the salt precursors of a conventional $CH_3NH_3PbI_3$ perovskite material are able to react through diffusion promoted by high temperature.[207] During a solid-state reaction process, the initial perovskite precursor solutions, namely PbI_2 and CH_3NH_3I, are deposited through spin-coating on top of two separate substrates and are subsequently annealed to form thin films. Next, the substrates with the deposited films come into direct contact, with the CH_3NH_3I film being placed face-to-face on top of the PbI_2 film. An annealing step in the 100–200 °C range[208] for 30 minutes then takes place so that CH_3NH_3I diffuses effectively into the yellow PbI_2 film. During annealing, perovskite nuclei start forming at the interface between the two deposited films, a process being completed gradually in the whole bulk of the PbI_2 film.[209] At the end of annealing, the top substrate is removed, revealing a compact dark brown $CH_3NH_3PbI_3$ perovskite film. The color change from yellow to dark brown is a sign that the initial PbI_2 film has been fully converted into a perovskite material.[210] The preparation of the $CH_3NH_3PbI_3$ film using the solid-state reaction method and the corresponding photographs of the formed films are presented in Fig. 14a.

As mentioned, the interdiffusion step of this process includes annealing at high temperatures. A high temperature of above 100 °C is most commonly applied because effective diffusion between the two precursor films is impeded by the kinetically unfavourable van der Waals gap in the interface between them. However, the necessity of applying higher annealing temperature to enable the diffusion entails consuming more energy and creating more non-radiative defects in the final film. It is thus possible to shorten the diffusion distance through the use of a nanoporous PbI_2 film or a less crystallized nanoporous one, so that lower temperatures can be applied. In nanoporous films, the diffusion distance is determined by the size of particles and not the bulk film thickness, while the larger surface area accelerates the reaction. In this way, the temperature employed can be decreased to 75 °C.[211]

A main advantage of this solid-state reaction method is that there is no need for orthogonal solvents during the film

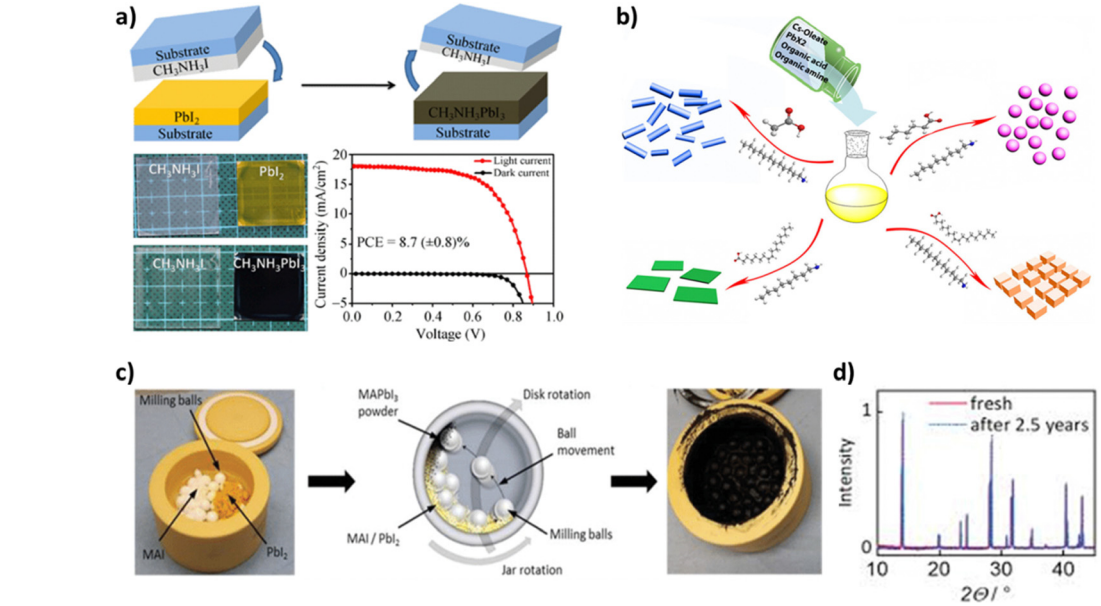

Fig. 14 (a) Schematic illustration of the fabrication process of perovskite films using a solid-state reaction (top) and the corresponding photographs of the real films (bottom-left). The *J*–*V* curves of the perovskite solar cells prepared using the solid-state chemical reaction method under AM 1.5G irradiation and in the dark (bottom-right). Adapted with permission from ref. 210. (b) Schematic illustrating the formation processes for different $CsPbX_3$ (where X = Cl, Br, I) nanocrystals mediated by organic acid and amine ligands at room temperature: hexanoic acid and octylamine for spherical quantum dots; oleic acid and dodecylamine for nanocubes; acetate acid and dodecylamine for nanorods; and oleic acid and octylamine for few-unit-cell-thick nanoplatelets. Adapted with permission from ref. 222. (c) Photograph of a milling jar loaded with milling balls, MAI, and PbI_2 precursor powders (left), schematic of the ball milling procedure for the mechanochemical synthesis of perovskite powders (middle), and photograph of the milling jar after the ball milling process and successful mechanochemical synthesis of black $MAPbI_3$ powder (right). (d) XRD patterns of $MAPbI_3$ powders before and after more than two and a half years of storage in a dry atmosphere. Adapted with permission from ref. 237.

fabrication and that the final film is compact with minimal surface roughness. Moreover, no careful control of the ratio of the two precursor salts is required in order to form stoichiometric perovskites. The sole controlling parameters of the reaction in question are the quantity of CH_3NH_3I and the reaction time, both of which should be sufficient enough to let the PbI_2 film be converted into $CH_3NH_3PbI_3$. Any CH_3NH_3I excess can be removed *via* both the annealing step and the removal of the top substrate, which creates the possibility that it could be reused in another deposition process. Finally, the solid-state reaction method shows potential for a future-scale up, thanks to the reproducibility of this process as well as lack of solvents.[207,210]

3.2.9 Precipitation reaction. Generally, precipitation refers to a chemical reaction that occurs in solution when two ions bond together to form an insoluble salt, which is known as the precipitate. A precipitation reaction can occur when the solubility of a solution changes, inducing supersaturation. According to the supersaturation principle, a solution of the desired substance is added to another solvent (the so-called anti-solvent) in which the former is sparingly soluble. After this addition, precipitation will follow, because of the lower solubility of the substance. Generally, precipitation takes place when the concentration of a substance becomes higher than its solubility, as in the case of supersaturated solutions.

Indeed, in the case of perovskites, their crystallization process is controlled by the supersaturation induced by the solubility change with solvent mixing. More specifically, after the initial perovskite precursor salts are dissolved in a suitable highly polar aprotic solvent, a non-polar solvent is added. The precursor ions are insoluble in the latter, leading to the production of a highly supersaturated state which results in the crystallization of perovskite material in the mutually mixed solution. Considering that multiple ions bond together to create the final perovskite structure, the precipitation reaction is often called co-precipitation, since it implies the simultaneous precipitation of ions from the precursor salts. However, in the case of techniques employed for the synthesis of perovskite crystals, the term used is anti-solvent precipitation.[212]

3.2.10 Anti-solvent dripping technique. The anti-solvent precipitation or crystallization method is used for simple fabrication of uniform perovskite films from solutions. During this procedure, the solution containing perovskite precursors dissolved in aprotic solvent is deposited through spin coating on top of the desired substrate. For example, in the case of $MAPbI_3$ perovskite, the salt precursors are MAI and PbI_2. At a specific time point during spin coating, a certain quantity of anti-solvent is quickly dripped onto the substrate, so that the salt precursors precipitate out of the solution. In this way, crystallization takes place, yielding a compact film as a final result and thus leading to the desired film formation. This film formation can be accompanied by a change in color, such as in $MAPbI_3$ perovskite films, where the initial film is yellow-colored but it darkens to brown after the anti-solvent is added because

of the precipitation of salts out of the solution and the subsequent film crystallization.[213,214]

It is worthwhile to note that there are certain combinations of solvents with anti-solvents used for the precipitation method to take place effectively, producing compact and uniform perovskite films. As a general rule, solvents in which perovskite precursor salts have poor solubility, such as chlorobenzene (CB), toluene (TL) and diethyl ether (DE), seem to be most commonly employed as anti-solvents, even though many other green antisolvents, such as ethanol and ethyl acetate, have been probed.[215–217] According to Paek *et al.*,[218] the critical parameters to decide on an appropriate anti-solvent are its miscibility, high boiling point, and dielectric constant (with a value of >5). Moreover, according to the anti-solvent employed in each synthesis, the quantity dripped and the point of dripping during spin coating tend to differ and need to be optimized appropriately.

3.2.11 Hot-injection method and ligand-assisted reprecipitation (LARP) method. As mentioned, the precipitation reaction is commonly employed to form perovskite crystals from solution. The growth of these crystals can be limited to the nanometer scale through the addition of organic ligands, namely carboxylic acids and amines, in the perovskite precursor solution. This modified method, yielding nanocrystals of various morphologies in colloidal solutions, is called the hot-injection method or ligand-assisted reprecipitation method, according to the temperature and specifics employed.[219]

The ligand-assisted reprecipitation technique involves two steps. In the first step, the perovskite precursors and ligands are added in a ''good'' polar solvent such as dimethylformamide (DMF), tetrahydrofuran (THF) or dimethyl sulfoxide (DMSO). The dissolution of precursor salts and molecule ligands is favored by polar solvents. For the fabrication of $CH_3NH_3PbBr_3$ nanoparticles, the salts used are CH_3NH_3Br and $PbBr_2$, the ligands added are a medium-to-long chain alkyl ammonium bromide, such as octylamine, and oleic acid, while octadecene was also incorporated in the solution as a non-coordinating solvent. The solution is then stirred and heated at 60–80 °C until it becomes colorless. In the second step, a ''bad'' non-polar solvent in which the perovskite materials are slightly soluble, such as toluene, acetone or hexane, is added to the aforementioned solution, while rigorous stirring follows. The poor solubility of the perovskite precursor salt ions in such solvents promotes their reprecipitation and the formation of the desired products as solids at the bottom of the reaction flask, with solution colour changes indicating the identity of the reaction products. The mixture is finally cooled and centrifuged in order to collect the desired nanocrystals.[220–222] Fig. 14b illustrates the formation processes for different $CsPbX_3$ nanocrystals, such as nanorods, quantum dots, nanocubes and nanoplatelets.

A similar method to LARP is the hot-injection method, requiring higher temperatures in the 80–200 °C range. In this type of synthesis two solutions containing precursor salts and ligands need to be prepared. In order to fabricate $CsPbX_3$ nanocrystals, cesium acetate and oleic acid are dissolved in hexadecane at 120 °C, thus forming cesium oleate solution. For preparing the second solution, PbX_2 is added to octadecene and the mixture is dried under vacuum at 120 °C. After drying, a capping ligand mixture of dried oleylamine and oleic acid at a 1 : 1 ratio as is injected in a N_2 atmosphere. After PbX_2 has been dissolved, the temperature is raised to 140–200 °C for tuning the nanocrystals' size. The cesium oleate solution is then injected into the second solution, with perovskite crystals forming instantaneously. The solution is cooled in an ice bath and then subjected to centrifugation, resulting in the final perovskite crystals.[223] For the fabrication of other perovskite crystals, such as $FAPbBr_3$ with formamidinium instead of cesium, formamidinium acetate is added in lieu of cesium acetate and heated at 130 °C, thus forming FA-oleate as the first reaction solution. Another more complex approach for synthesizing $FAPbBr_3$ nanocrystals incorporating oleylammonium bromide and CH_3MgBr precursors was proposed by Protesescu *et al.*, with the former precursor producing brightly-luminescent cubic-shaped nanocrystals.[224]

The use of long alkyl chain ammonium cations as capping ligands on the surfaces of nanoparticles is a strategy enabling control over their size and morphology, by preventing the formation of nanostructures other than the desired. Octylamine, along with longer chain amines such as dodecylamine and hexadecylamine, is used to control the kinetics of the crystallization by slowing down the crystallization rate of the precursors. On the other hand, the use of oleic acid or other long chain alkyl acids, such as octanoic acid and butyric acid, involves the stabilization of the colloidal solution under storage conditions, by suppressing the aggregation of nanocrystals. This leads to the crystallization of perovskite moieties into colloidal nanoparticles in a controlled way.

Through the reprecipitation reaction assisted by ligands, it is possible to synthesize a variety of perovskite nanostructures in solution, including zero-dimensional spherical quantum dots, nanocubes, one-dimensional nanorods and two-dimensional nanoplatelets. This is especially pertinent to $CsPbX_3$ perovskites. For each nanostructure, a different organic acid and an amine as capping ligands are employed in order to control the size and morphology of the final product. More specifically, along with the polar solvent and the perovskite precursor salts, hexanoic acid and octylamine were added in order to create spherical quantum dots. Similarly, oleic acid and dodecylamine were employed for nanocubes, acetate acid and dodecylamine for nanorods and oleic acid and octylamine for few-unit-cell-thick nanoplatelets.[222]

Another application of the hot-injection and LARP methods is the creation of quantum dots in a wide color range. By using salt precursors with different halogen anions and tunable compositions, a range of brightly luminescent colloidal $CsPbX_3$ and $CH_3NH_3PbX_3$ quantum dots with high photoluminescence quantum yield values above 70% can be fabricated. In this way, color tuning is performed, since the absorption and photoluminescence maxima vary according to the X-moiety incorporated.[225]

The main advantage of the LARP method over the hot-injection method is that it is performed at moderate temperatures below 70 °C. This also comes in contrast to other techniques requiring heating at high temperatures, such as vacuum ones. Moreover, there are minimal equipment requirements compared to the hot-injection method, where the rate of injection and the inert atmosphere need to be modified accordingly, making it a low-cost technique with scale-up potential. Another benefit is the dispersion of the perovskite product in a colloidal solution medium, making its further deposition on substrates simple.[226] In addition, lead-free perovskite films and nanocrystals, such as $CsSnX_3$, can be easily prepared through the LARP method in the same way as their counterparts containing lead.[227]

3.2.12 Electro/chemical bath deposition. Halide perovskites have also been synthesized *via* electrochemical bath deposition. However, this method has not yet attracted attention and there are few reports demonstrating electrochemically prepared perovskites. For the synthesis of $MAPbI_3$, which is the mostly investigated perovskite formed through electrochemical deposition, usually lead oxide (PbO_2) was first deposited by electrodeposition and then the PbO_2 was immersed in a solution of hydroiodic acid (HI) in ethanol to convert it to PbI_2. Consequently, the PbI_2 film was immersed in a MAI/isopropyl solution to form the desired perovskite.[228] In a similar but simpler approach, the electrodeposited PbO_2 film was immersed in a MAI/isopropanol solution and $MAPbI_3$ was directly formed.[229] Although the PbO_2 did not fully convert to $MAPbI_3$, the temperature during the conversion procedure played a crucial role in the preferable (110) orientation of the synthesized perovskite. Furthermore, the electrochemical perovskite exhibited a higher photoluminescence intensity peak than that prepared by solution-processing of PbI_2, along with lower trap density and almost eliminated grain boundaries. In another approach, Popov *et al.*[230] demonstrated the preparation of uniform $MAPbI_3$ films by sequentially exposing the electrodeposited PbO_2 film to HI and MAI vapors. The dependence of the crystallinity, grain size, and thickness of the prepared perovskite films on the deposition time was also reported. Recently, electrodeposition of $MAPbI_3$ single-crystal particles on indium-tin-oxide (ITO) was reported.[231] The novelty of this work was attributed to the adjustment of perovskite crystal size and density by changing the electrochemical potential applied to the ITO.

Besides PbO_2, PbS has also been used as a precursor for the preparation of $MAPbI_3$. Luo *et al.*[232] electrodeposited PbS and then a MAI CVD process was used for the successful conversion into the desired black perovskite film. More importantly, the authors managed to develop high-quality, curved and large-area $MAPbI_3$ films, which are promising for large-area perovskite optoelectronic devices. In a recent work, a Pb film was electrodeposited on mesoporous titanium oxide (m-TiO_2) and then MAI was deposited atop.[233] $MAPbI_3$ was formed in a MAI/isopropanol solution by adjusting the time of reaction. In addition, the incorporation of the $MAPbI_3$ films in mesoscopic perovskite solar cells led to high values of the electrical parameters, making electrodeposition a feasible method for preparing homogeneous and uniform perovskite films for perovskite-based devices.

Moreover, electrochemical deposition has been applied to prepare all-inorganic perovskite films, as well. For the formation of $CsPbBr_3$, Pb was deposited on mesoporous TiO_2 in PbI_2/isopropanol solution, and then it was converted into $CsPbBr_3$ perovskite in a CsBr/methanol solution.[234] The reaction was performed in air at room temperature under a positive bias. The deposition current and time of the PbI_2 during the first-step of the method were the important factors for the control of the grain size and film thickness of the synthesized perovskite. On the other hand, the crystallinity of the $CsPbBr_3$ film was affected by the second-step-conversion voltage and time. $CsPb_{2-x}Br_{1+x}$ was also prepared by immersing an electrodeposited PbO_2 in HI/ethanol solution to form as already mentioned the PbI_2 film. The preparation of the perovskite film was completed *via* spin-coating CsBr solution in methanol. The authors demonstrated that the addition of a small amount of DMF in the CsBr/methanol solution improved the perovskite film formation and crystallinity, and thus the efficiency of the fabricated perovskite solar cells based on the synthesized $CsPb_{2-x}Br_{1+x}$.

3.3 Mechanochemical synthesis

Mechanochemical synthesis is a solid-state solvent-free method for halide perovskite preparation. In this method a mixture of AX and BX_2 (*e.g.*, MAI, MABr, FAI, and CsI, and PbI_2 and $PbBr_2$) precursor powders are placed together in a ball mill[235] or in a simpler approach in a portal,[236] and ground until the corresponding perovskite is formed. In order to prepare a cleaner crystalline perovskite, ball milling is the best strategy that avoids remains of unreacted precursors that might exist due to pestling. The balls and bowls are usually made of stainless steel or zirconia. During the reaction, energy transfer from the balls to the precursor powders occurs, crushing the reactant materials and forming the perovskite with a simultaneous color change. Fig. 14c shows the mechanochemically synthesized $MAPbI_3$ powder along with the change in color from yellow to black. Thus critical parameters for the size and crystallinity of the prepared perovskite are the bowl rotation speed, the number of milling balls, and the reaction energy.[237]

Over the last decade, various halide perovskites have been synthesized *via* a mechanochemical method including hybrid organic–inorganic perovskites with MA^+ or FA^+ as the organic compound and I^-, Br^- or Cl^- as the X^- halide anion[238–240] and all-inorganic $CsPbX_3$ perovskites.[241–245] Moreover, mechanochemically synthesized Pb-free perovskites based on Sn,[246,247] copper (Cu)[248] and bismuth (Bi)[249] have been demonstrated. Interestingly, the use of CsCl as precursor powder led to the successful preparation of multiple-cation perovskite materials, solving the problem of the poor solubility of some cesium halides in traditional DMSO and DMF solvents.[250] Table 2 summarizes the electrical parameters of solar cells based on solution-processed and mechanochemically synthesized perovskites.

Table 2 Perovskite solar cell parameters based on solution deposition methods and mechanochemical synthesis of perovskite layers

Method	Perovskite	J_{SC} (mA cm^{-2})	V_{OC} (V)	FF	PCE (%)	Ref.
Dip-cast	$MAPbI_3$	17.1	0.992	0.73	12.9	126
One-step spin-coating	$MAPbI_3$	21.2	0.96	0.74	16.7	127
Hot-casting spin-coating	$PbCH_3NH_3I_{3-x}Cl_x$	22.4	0.92	0.82	16.9	131
Drop-cast	$Cs_{0.1}Rb_{0.05}FA_{0.85}PbI_3$	22.69	0.909	0.786	16.21	132
Two-step spin-coating	$MAPbI_3$	16.50	0.97	0.66	10.58	133
One-step spin-coating	$MAPbI_3$	21.1	1.04	0.63	13.8	134
Two-step spin-coating	$CH_3NH_3PbI_3$	21.47	1.024	0.634	13.9	135
Two-step spin-coating	$MAPbI_3$	19.6	0.99	0.793	15.4	136
Drop-cast	$MAPbI_3$	22.76	1.08	0.7563	18.57	139
Drop-cast	$(5\text{-AVA})_x(MA)_{1-x}PbI_3$	22.8	0.858	0.66	12.84	141
Drop-cast	$(5\text{-AVA})_x(MA)_{1-x}PbI_3$	22.7	0.85	0.66	12.9	142
Slot-die	$(C_4A)_2MA_4Pb_5I_{16}$	15.58	1.08	0.52	8.75	143
VASP	$MAPbI_3$	19.8	0.924	0.663	12.1	147
VASP	$CH_3NH_3PbI_3$	19.9	0.90	0.76	13.5	148
VASP	$CH_3NH_3PbI_{3-x}Cl_x$	15.1	1.11	0.69	11.6	148
VASP	$CH_3NH_3PbI_{3-x}Br_x$	14.2	1.07	0.69	10.5	148
VASP	$(FA)_x(MA)_{1-x}PbI_3$	22.51	1.00	0.7356	16.48	150
Hydrothermal	$Cs_2AgBiBr_6$	3.96	0.98	0.624	2.43	153
Hydrothermal	$MAPbI_3$	24	1.015	0.74	18.02	160
Hydrothermal	δ-$CsPbI_3$	2	0.55	0.66	0.74	162
Hydrothermal	α-$CsPbI_3$	13.8	0.94	0.52	6.90	162
Hydrothermal	$CsPb_2Br_5$	5.7	0.82	0.59	2.82	162
Ultrasound-assisted	$MAPbBr_3$	6.69	1.36	0.69	6.53	187
Microwave-assisted	$MAPbI_3$	21.9	1.041	0.735	16.8	199
Solid-state reaction	$MAPbI_3$	22.49	1.08	0.67	16.21	206
Solid-state reaction	$MAPbI_3$	19.6	1.00	0.747	14.7	207
Solid-state reaction	$MAPbI_3$	22.20	1.01	0.6808	15.21	209
Solid-state reaction	$MAPbI_3$	17.9	0.87	0.643	10.00	210
Low-temperature solid-state reaction	$MAPbI_3$	22.5	0.956	0.642	13.8	211
Anti-solvent dripping technique	$Cs_{0.15}FA_{0.85}PbI_3$	24.26	1.05	0.7635	21.53	215
Anti-solvent treatment	$MAPbI_3$	22.2	1.082	0.74	17.75	216
Anti-solvent treatment	$MAPbI_3$	24.48	1.12	0.7695	21.09	217
Anti-solvent treatment	$MAPbI_3$	23.3	1.10	0.79	20.3	218
Electrodeposition	$MAPbI_3$	19.1	0.97	0.55	10.19	228
Vapor-assisted chemical bath deposition	$MAPbI_3$	—	—	—	4.68	232
Electrochemical deposition	$MAPbI_3$	23.24	0.92	0.663	14.33	233
Electrochemical deposition	$CsPbBr_3$	8.85	1.43	0.62	7.86	234
Mechanochemical synthesis	$(Cs_{0.05}FA_{0.95}PbI_3)_{0.85}(MAPbBr_3)_{0.15}$	16.8	1.00	0.74	12.4	237
Mechanochemical synthesis	$FAI/PbI_2/MABr/PbBr_2/CsCl$	22.54	1.16	0.711	19.12	250

One of the main advantages of mechanochemically synthesized perovskites is their high stability, making them promising candidates for perovskite optoelectronic devices. It is demonstrated that $FAPbI_3$ and $CsPbI_3$ prepared *via* a mechanochemical method directly crystallize into the desired black α-phase and more slowly degrade into the yellow δ-phase compared to the corresponding solution-processed perovskites.[237,251] $MAPbI_3$ also shows outstanding stability when stored in dry nitrogen for 2.5 years, as revealed by X-ray diffraction measurements presented in Fig. 14d.[237] Furthermore, the same perovskite powder was thermally stable when exposed to 160 °C for 11 h and humidity conditions, as well. Moreover, a mechanochemical process was applied for upscale synthesis of perovskite powders. Recently, Tang *et al.*[252] reported the synthesis of 100 g $MAPb(I_xBr_{1-x})_3$ and $MAPb(Br_xCl_{1-x})_3$ powders using ball milling and $MAPbX_3$ precursors. Hong *et al.*[237] synthesized 250 g of $CsSnX_3$ powder and used it for the fabrication of perovskite photodetectors based on a completely solvent-free protocol, suggesting the successful development of perovskite devices with reduced environmental and energetic footprints.

4. Growth of single crystals and the corresponding layers

There are several techniques that have been used so far, to grow single-crystal (SC) halide perovskites. The method that is used is very important, since the quality of the crystal is a defining factor in scientific and industrial applications. In this section the corresponding methods for perovskite single-crystal growth and the formation of the corresponding layers are summarized.

4.1 Growth of perovskite crystals

Perovskite single crystals have gained enormous attention in recent years due to their facile synthesis and excellent optoelectronic properties. The synthetic approaches adopted for the growth of perovskite single crystals, particularly through solution-based growth, are described in the following sections.

4.1.1 Droplet-pinned crystallization. The droplet-pinned crystallization (DPC) method was developed in order to grow aligned single crystals.[34,253,254] Ye *et al.* used this method to grow single-crystalline perovskite arrays on top of poly(3,4-ethylenedioxythiophene):polystyrene sulfonate (PEDOT:PSS)

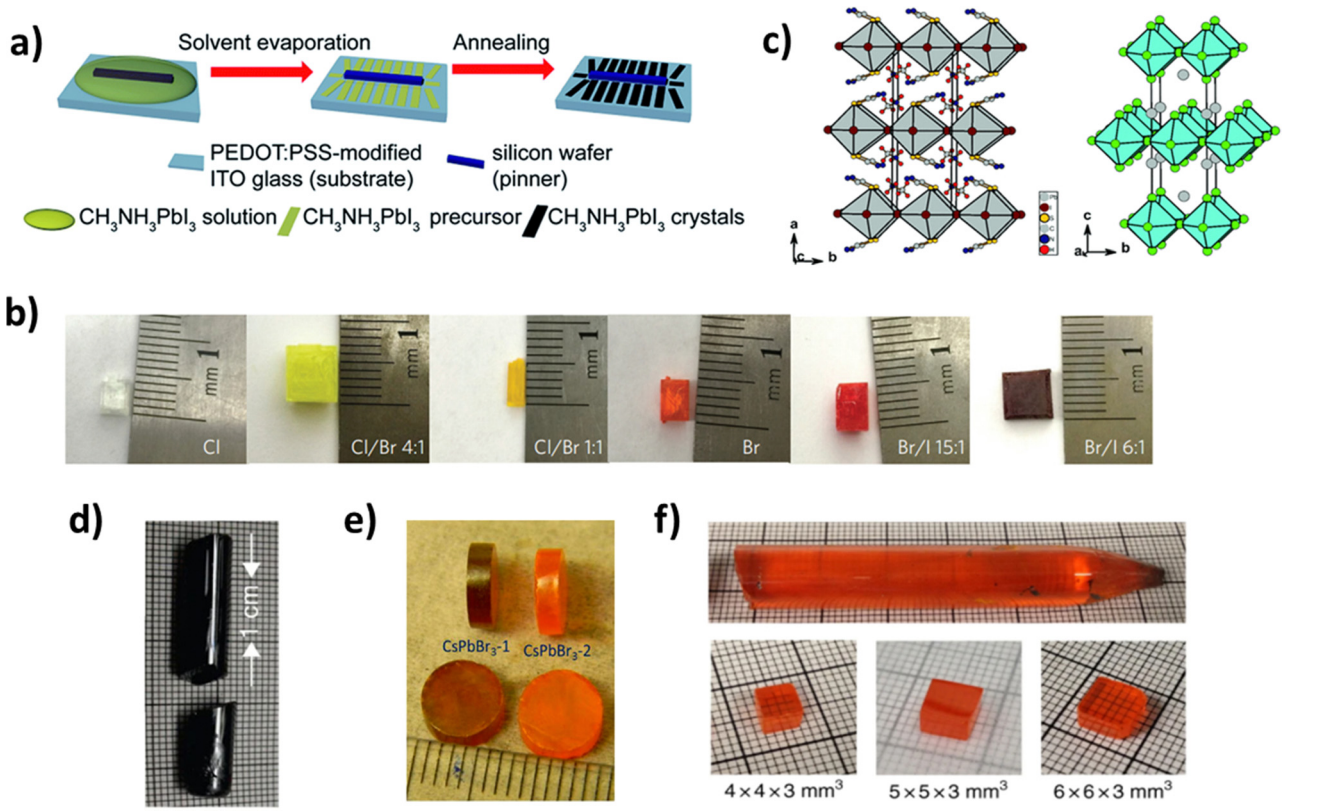

Fig. 15 (a) Schematic of the growth process of $CH_3NH_3PbI_3$ arrays. Adapted with permission from ref. 249. (b) Photographs of single-halide and mixed-halide perovskite SCs with different halide compositions. Adapted with permission from ref. 3. (c) Crystal structures of $(CH_3NH_3)_2Pb(SCN)_2I_2$ (left) and K_2NiF_4 (right). Adapted with permission from ref. 46. (d) $CsSnI_3$ SCs grown in a Bridgman furnace. Adapted with permission from ref. 264. (e) Photograph of the SC specimens: $CsPbBr_3$-1 and $CsPbBr_3$-2. Adapted with permission from ref. 255. (f) As-grown SC ingot with a diameter of 11 mm, and the single crystal wafers with different sizes. Adapted with permission from ref. 263.

layers.[255] 20 μL of $CH_3NH_3PbI_3$ solution was dropped onto the substrates and a piece of silicon wafer was placed on them, in order to pin the solution droplet. The crystal arrays formed after the solvent started evaporating at 80 °C on a hotplate, and then, after 15 minutes, were annealed at 100 °C for 3 minutes. Fig. 15a illustrates the proposed DCP method for $CH_3NH_3PbI_3$ arrays. The single-crystalline perovskite arrays that were developed with this method were then used for making an inverted solar cell, but with very low performance, due to the incomplete coverage of the PEDOT:PSS substrate and to the defects on the crystal surface.

4.1.2 Solvothermal growth. As already mentioned, the solvothermal growth method is performed in a sealed environment, where no generation of an inert atmosphere is needed, while offering accurate control over the morphology of the generated SCs, thus making it an easy and not very complicated method for growing crystals. Yet, there are some safety issues, because the reaction process takes place in a closed environment, where it cannot be observed. Zhang *et al.* used this method in order to grow $(CH_3NH_3)Pb(Br_{1-x}Cl_x)_3$ mixed halide perovskite SCs of stoichiometric $PbBr_2$ and $[(1-y)\text{-}CH_3NH_3Br + yCH_3NH_3Cl]$ DMF precursor solutions.[256] The $PbBr_2$, CH_3NH_3Br and CH_3NH_3Cl precursors in various molar ratios were dissolved in DMF and heated at 50 °C for up to 5 hours, leading to the formation of $CH_3NH_3Pb(Br_{1-x}Cl_x)_3$ SCs. The optical absorption studies displayed a blue shift when the chloride content was increased in the reaction mixture. The XRD measurements of the crystals showed an increase of the 2θ value with more chloride content, suggesting contraction of the unit cell length. Using the same technique, Fang *et al.* reported the growth of single-halide perovskite SCs, as well as $MAPbBr_{3-x}Cl_x$ and $MAPbI_{3-x}Br_x$ mixed-halide perovskite SCs, with an absorption peak shifting from blue to red.[3] The precursor solution was consisted of the mixing of methylamine with haloid acids of different halide ratios, and of lead(II) acetate, in order to form a super-saturated aqueous solution at 100 °C. Then, the SCs were precipitated when the temperature was slowly decreased and crystals with thicknesses of about 0.5–5 mm were synthesized. Fig. 15b shows photographs of 5 mm thick single halide and mixed halide perovskite SCs with different halide compositions.

4.1.3 Slow evaporation. This method for obtaining single crystals with a solution growth process is a straightforward one. A solution is prepared by mixing the reactants in the appropriate solvent and then letting it slowly evaporate in a suitable container. It can be performed either under an inert atmosphere, or under atmospheric conditions, in a variety of containers like an NMR tube, a centrifuge tube, a beaker or a round

bottom flask. However, due to the low solubility of the perovskite precursors, it is difficult to use this method with high precision; therefore this method has a limited application and is not widely used. Liao *et al.* managed to grow hybrid organo-plumbate $(benzylammonium)_2PbCl_4$ small crystals, by mixing stoichiometric $PbCl_2$ and benzylammonium chloride in a concentrated HCl aqueous solution.[257] After slowly evaporating the solution, they took large crystals of up to $5 \times 10 \times 2\,mm^3$. The tunability of the hybrid organo-plumbates makes it easy to customize the band gap and the visible absorbance for an appropriate application in photovoltaics through cation and halide replacement. Daub *et al.* used this method for the reaction of CH_3NH_3I with $Pb(SCN)_2$ in order to grow $(CH_3NH_3)_2Pb(SCN)_2I_2$ crystals, with a structure that was similar to the K_2NiF_4-type as seen in Fig. 15c.[46]

4.1.4 Bridgman method. The Bridgman method is used in order to grow large crystals inside sealed ampoules.[258] A quartz ampoule is filled with the reactants, which are sealed under vacuum, and then the ampoule is moved inside a furnace that is under a temperature gradient. The nucleation of the crystal takes place at the ampoule tip at a defined temperature, and the crystallization spreads through the melted powder. During this process, when impurities have different solubilities than that of the crystal, they get separated from the crystal, but in case the solubility is about the same, the Bridgman method is unable to remove the impurities. This method is used for inorganic SC perovskites, since organic compounds are chemically unstable near their melting point. Also, since the grown crystals are in contact with the ampoule wall, mechanical stresses are induced and the densities of impurities and defects are increased with this method, thus limiting the fabrication of high quality devices.[259] Using the Bridgman method Chung *et al.* managed to grow $CsSnI_3$ polycrystalline ingots (Fig. 15d), which were promising candidates for use in thermoelectric applications.[260] The SC growth was achieved by putting a stoichiometric mixture of CsI, SnI_2 and SnF_2 under vacuum at 450 °C for 30 minutes and then cooling at room temperature. First Rodova *et al.*[261] and later Stoumpos *et al.*[262] grew $CsPbBr_3$ SC perovskites with the same method (Fig. 15e), mainly as promising candidate materials for X- and γ-ray radiation detection. The $CsPbBr_3$ SCs were prepared from equimolar amounts of CsBr and $PbBr_2$ that were transferred to a sealed silica ampoule and then gradually annealed up to 600 °C for 6 hours under vacuum and then left to cool at room temperature.

More recently, He *et al.* managed to grow $CsPbBr_3$ SCs as well, with a modified melt growth method. They obtained large SC ingots that were crack-free with a purity of lower than 10 ppm of total impurities and a low defect density.[263] In order to form polycrystalline $CsPbBr_3$, both CsBr and $PbBr_2$ were mixed in a stoichiometric ratio of 1 : 1 at 580 °C. The synthesis and growth were both done in the same silica tube, in order to reduce contaminations that may develop in a multistep process, where the tube that was used had 11 mm inner diameter, with a conical shaped end, as shown in Fig. 15f. Zhang *et al.* reported also the growth of $CsPbBr_3$ SCs using a modified Bridgman method.[264] A quartz ampoule with an inner diameter of 24 mm, filled with 170 g of polycrystalline $CsPbBr_3$, was transferred to a 2-zone Bridgman furnace. The high and low temperature zones of the furnace were 600 °C and 200 °C, respectively, and the gradient of the temperature was 30–40 °C cm^{-1}. The ampoule was heated in the high temperature zone for 12 hours and then was cooled slowly, at 1 mm h^{-1}. Finally, the furnace was cooled to room temperature during 3 days and a large crack-free SC of $CsPbBr_3$ was obtained.

4.1.5 Inverse temperature crystallization (ITC) method. The ITC method is based on the different solubilities of materials at different temperature values. In particular, these materials are very soluble at room temperature, while their solubility decreases with increase in temperature, leading the perovskite molecules to concentrate in the solution. The crystal growth starts when the solution is supersaturated. Therefore, the SC growth in the ITC method depends equally on the dissolution and precipitation. Fig. 16a–c illustrates the growth of SC perovskites *via* an ITC process.[265] In addition, the most important factor of ITC growth is the selection of solvents, such as GBL, DMF, and DMSO, which are used for the preparation of $MAPbX_3$ (where X = I, Br, Cl, respectively) SCs.[266] On the other hand, the selection of one solvent for the growth of mixed halide perovskites with two and more precursor materials is more challenging.

Saidaminov *et al.*[49] investigated the influence of different solvents at various temperatures on the preparation of $MAPbX_3$ and $FAPbX_3$ SCs, suggesting that GBL and DMF were suitable solvents for ITC growth of I- and Br-based perovskites, respectively. In the same context, $MAPbI_3$ was synthesized *via* the ITC method using GBL solvent.[47] The solution was first prepared at 100 °C under vigorous stirring, and then the temperature was increased to 190 °C in order to form the perovskite crystals. Afterwards, the temperature was decreased to 25 °C, leading to undesirable dissolution of the synthesized SCs. Recently, a large-sized $MAPbI_3$ SC was formed with the ITC method and the anisotropic properties at the surface and bulk of the SC were investigated.[267] Parikh *et al.* suggested that the (112) facet of the $MAPbI_3$ SC exhibited higher trap density than the (100) facet, resulting in higher hysteresis. Furthermore, low trap density along with high mobility was reported for the $MAPbBr_3$ SC based photodetector.[88] The proposed ITC method used a low dissolution process, forming high-crystalline-quality perovskite SCs, which played a critical role in the photoresponse of the fabricated SC devices.

All-inorganic perovskite and mixed cation SCs were also prepared using ITC growth. For instance, large-sized orange colored $CsPbBr_3$ crystals were grown using ternary solvents, where DMF and GBL or cyclohexanol were used to improve the solubility of the perovskite in DMSO.[268,269] Furthermore, a mixed cation $(FAPbI_3)_{0.9}(MAPbBr_3)_{0.05}(CsPbBr_3)_{0.05}$ single crystal was grown in a GBL solution heated at 95 °C.[44] Interestingly, the prepared SC exhibited high stability upon light and water/oxygen exposure for 1000 h and 10 000 h, respectively. Recently, high performance perovskite solar cells based on a mixed cation $FA_{0.6}MA_{0.4}PbI_3$ SC were reported. The ability of the prepared SC, used as the absorption layer, to red-shift the

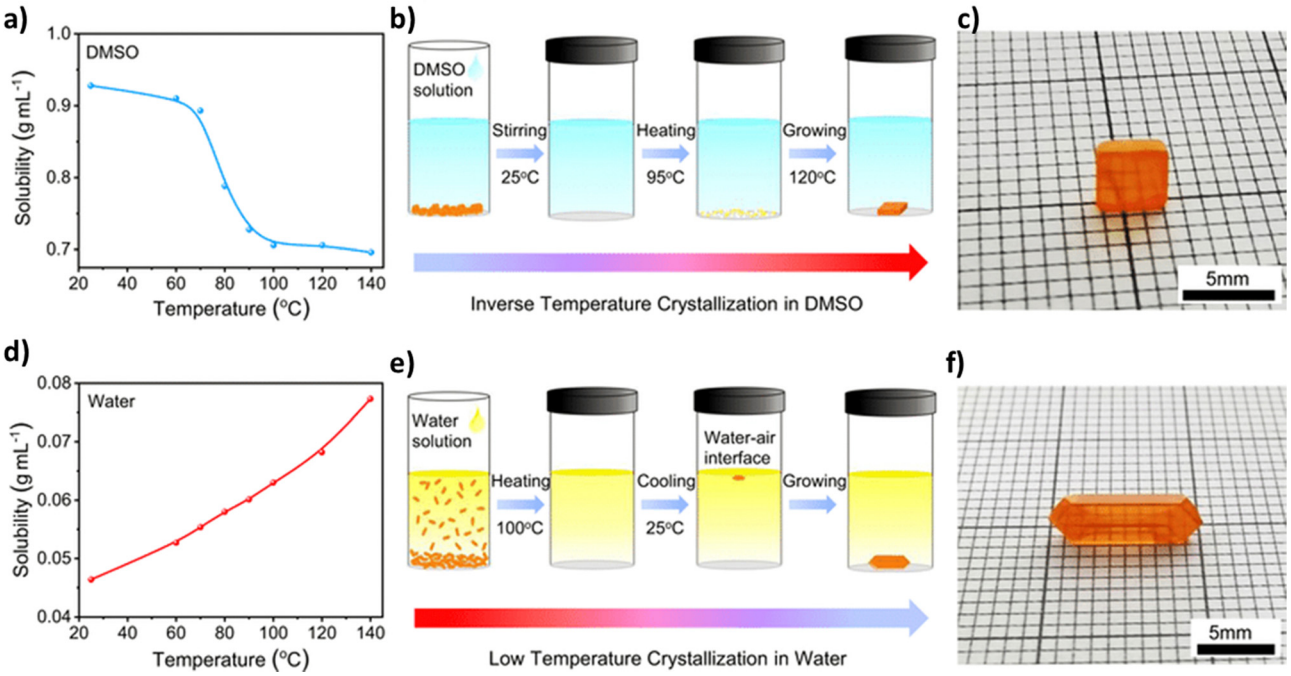

Fig. 16 (a) Temperature-dependent solubility of $CsPbBr_3$ in DMSO. (b) Schematic illustration of the inverse-temperature crystallization in DMSO. (c) Optical image of the as-prepared $CsPbBr_3$ SC. (d) Temperature-dependent solubility of $CsPbBr_3$ in water. (e) Schematic illustration of the low-temperature crystallization in water. (f) Optical image of the as-prepared $CsPbBr_3$ SC. Adapted with permission from ref. 266.

external quantum efficiency spectrum increased the short-circuit current density of the device, exhibiting a high PCE of 22.8%.[270] In addition, Pb-free perovskite SCs, such as $MASnI_3$, were synthesized *via* an ITC procedure.[271] A 2 mm × 1 mm × 1.2 mm $MASnI_3$ without a sign of Sn(IV) in the crystal, as revealed by X-ray photoelectron spectroscopy, exhibited good crystalline properties, along with high optical absorbance, making it a promising material for solar cell fabrication.

4.1.6 Modified inverse temperature crystallization (MITC). Modified inverse temperature crystallization (MITC) combines the ITC method with cooling solution for the synthesis of SC perovskites, where crystal seeds are prepared *via* cooling solution, then they are placed in a precursor solution to grow larger perovskite crystals through the ITC method. Large $MAPbX_3$ and $FAPbX_3$ SCs have been successfully prepared with different shapes. Black $MAPbI_3$ SCs are commonly formed as dodecahedra and sometimes as rhombo-hexagonal dodecahedra.[272] On the other hand, $MAPbBr_3$ and $MAPbCl_3$ single-crystals, which are transparent and orange colored, respectively, exhibit a cuboidal shape.[273] For the synthesis of $FAPbI_3$ SCs, a seed crystal was formed through cooling solution, then ITC growth was repeated three times.[274] The prepared SCs exhibited long carrier lifetimes and high carrier mobility. Moreover, a redshift in the PL emission spectrum of $FAPbI_3$ SCs was observed with respect to that of the corresponding perovskite thin film.

MITC is a useful method to grow all-inorganic SCs. Especially, synthesis of pure $CsPbBr_3$ SCs can be achieved by avoiding undesirable impure crystals formed due to the poor solubility of CsBr.[275,276] Recently, $CsPbBr_3$ was prepared through MITC using water as solvent. The solubility of the crystals at various temperatures was investigated, and the structural and electronic properties of the SCs were studied and compared with those of the $CsPbBr_3$ crystal synthesized in DMSO.[267] Fig. 16d–f illustrates the growth of SC perovskites *via* a MITC process. More recently, Cl-doping of $CsPbBr_3$ SCs grown *via* the MITC method was proposed to improve the photoelectric properties of the perovskite.[277] Reduced trap density and improved carrier mobility were reported for the $CsPbBr_{2.5}Cl_{0.5}$ SC compared with the undoped perovskite crystal, along with the high sensitivity of X-ray detectors, when the Cl-doped SCs were incorporated in the device. Pb-free all-inorganic perovskite SCs were also synthesized using the MITC process, such as $CsCu_2I_3$.[278] The 1D $CsCu_2I_3$ SC with a size of 13 mm showed high quality and stability, as well as a record PLQY of 50.4% at that time.

4.1.7 Antisolvent vapor-assisted crystallization (AVC) method. The antisolvent vapor-assisted crystallization (AVC) method is based on the different solubilities of perovskite precursors in various solvents, at a constant temperature. In particular, a solution is prepared consisting of the precursor perovskite and a solvent with high-solubility. The solution contained already in a vial is transferred to a larger vial having the antisolvent, which un-dissolves the precursor. During this process, the antisolvent diffuses into the perovskite solution acting as a contamination source, thus affecting the crystal growth and quality. Therefore, the choice of solvents is a crucial parameter for AVC growth. On the other hand, the molar ratio of the precursor materials is also important. For instance, 3 : 1 MAI : PbI_2 were dissolved in GBL solvent, and $MAPbI_3$ SCs were

formed using DCM as antisolvent, while for the growth of $MAPbBr_3$ a solution of 1 : 1 MABr and $PbBr_2$ in DMF was prepared using DCM as antisolvent.[279] In the same context, Yang *et al.*[280] proposed the use of toluene as antisolvent for the growth of $MAPbBr_3$ SCs. Furthermore, Wei and co-authors[281] demonstrated the formation of large and clear $MAPbBr_3$ SCs, dissolving MABr and $PbBr_2$ in a molar ratio of 1 : 0.8 in DMF. Interestingly, when incorporated in X-ray detectors, the devices were extremely efficient compared with those based on polycrystalline thin films. In a different approach, PbI_2 was dissolved in HI at 120 °C, forming a yellow solution, in which MAI was added afterwards. Then, the solution was cooled down and diethyl ether was used as antisolvent to grow $MAPbI_3$ SCs.[282]

Moreover, Pb-free $(NH_4)_3Sb_2I_9$ SCs were synthesized *via* the AVC procedure.[283] NH_4I and SbI_3 were dissolved in ethanol, while chloroform was the antisolvent, forming a 5.7 mm × 2.1 mm perovskite SC. Recently, mixed $Cs_xMA_{1-x}PbBr_3$ SCs were prepared according to the AVC method, where $PbBr_2$ and MABr with a molar ratio of 1 : 1 were dissolved in DMF, while CsBr and $PbBr_2$ with various molar ratios were tested.[284] The SCs were formed using methanol as antisolvent. The effects of Cs concentration on the molar volume and bandgap of mixed-perovskite alloys were also investigated. More recently, inorganic-cation pseudohalide 2D $Cs_2Pb(SCN)_2Br_2$ single crystals were synthesized for the first time through AVC.[285] It was demonstrated that the amount of $Pb(SCN)_2$ affected the stoichiometry of the perovskite. The prepared 2D $Cs_2Pb(SCN)_2Br_2$ SCs exhibited good moisture and thermal stability, and also very low exciton binding energy, making them a favorable material for efficient optoelectronic devices, such as photodetectors and solar cells.

4.1.8 Layered solution growth (LSG) method. Layered solution growth (LSG) is the most uncommon method for perovskite single crystal formation. In 1999, Mitzi[286] prepared for the first time perovskite SCs *via* LSG. In particular, $PbCl_2$/hydrochloric acid (HCl) solution was placed in a long straight tube. This solution represented the bottom solution layer. Another solution consisting of methanol was inserted in the tube with a syringe and placed on top of $PbCl_2$/HCl. Finally, $C_6H_5C_2H_4NH_2$ was added into the tube to serve as the top layer. Small $(C_6H_5C_2H_4NH_3)_2PbCl_4$ plate SCs were formed during the diffusion of the layers in the tube. However, LSG was a very slow process, where the formed crystals appeared after several weeks, and the final product was collected after one year.

4.1.9 Solution temperature lowering (STL) method. The solution temperature lowering (STL) method based on seeded growth is used for the synthesis of large perovskite single crystals. This method is divided into two categories depending on the position of the seeded crystal. For instance, $MAPbI_3$ SCs were prepared using the top-seeded solution growth (TSSG) method.[14] During TSSG, the seeded crystals were placed at the bottom of a vial containing the growth solution. Then, a silicon substrate was immersed into the solution, and by lowering the temperature at the top of the vial, single crystals were formed on the silicon substrate. In the same context, $MASnI_3$ and $FASnI_3$ SCs were also synthesized through TSSG, with the latter being unstable compared with the $MASnI_3$ due to the oxidation of tin.[287]

Dang *et al.* used the bottom-seeded solution growth (BSSG) method to prepare $MAPbI_3$ SCs.[288] A seeded crystal was placed in the middle of a tray, and consequently, the temperature was decreased from 65 °C to 40 °C so that the solute becomes saturated and thus crystals are formed. In a similar work, Lian *et al.*[289] synthesized also $MAPbI_3$ SCs using BSSG, lowering the solution temperature from 373 K to 330 K. Even though TSL is a suitable method for the successful preparation of large perovskite single crystals, it is time-consuming, requiring many days or even weeks to obtain high quality crystals.

4.2 Single crystal thin film growth techniques

Apart from the single crystal growing techniques mentioned above, there are also methods that aid in single crystal thin film (SCTF) growth. In order to grow perovskite SCTFs at the micrometer level, there are various methods that have been used, such as vapor phase epitaxial growth, the space-confined method, surface-tension assisted growth, and the top-down method.

4.2.1 Vapor phase epitaxial growth. This method is an old one, which has been used for the growth of electro-optic devices in the III–V semiconductor field.[290,291] It is capable of growing high-quality perovskite SCTFs, but it has a limited application, since an exceptional lattice match between the perovskites and the substrates is mandatory. Wang *et al.* employed this method in order to grow centimeter-scale SCTFs for inorganic halide perovskites ABX_3 on metal alkali halide substrates.[292] The structural and morphological characterization results of the halide perovskite single crystals are presented in Fig. 17. Later, Chen *et al.* also used the vapor phase epitaxial growth method, in order to grow cesium lead bromide perovskite ($CsPbBr_3$) SCTFs on oxide perovskite $SrTiO_3$(100) substrates with a controllable micrometer thickness.[293]

4.2.2 Space-confined method. Liu *et al.* developed the space-confined method, where they make perovskite wafers with controlled thinness by using a geometry-regulated dynamic-flow reaction system.[294] They made a single-crystalline $MAPbI_3$ perovskite wafer, by placing the wafer between two glass slides, which were parallel and had a designated separation height, in order to control the thickness of the created thin film (Fig. 17b). This technique was also used by other groups for more perovskite materials. Chen *et al.* used this method to grow various perovskite SCTFs like $MAPbI_3$, $MAPbCl_3$ and $MAPbBr_3$ with controlled thicknesses ranging from nano- to micrometers, which exhibited great air stability and quality, similar to those of the bulk SCs with a trap density of 4.8×10^{10} cm^{-3}, a carrier mobility of 15.7 cm^2 V^{-1} s^{-1}, and a carrier lifetime of 84 μs.[295] Later Rao *et al.* managed to grow a large area (120 cm^2) $MAPbBr_3$ SCTF on FTO glass, with a controlled thickness ranging from 0.1 to 0.8 mm[296] and a laminar $MAPbBr_3$ SCTF with a controlled thickness of 16 μm and dimensions of 6 mm × 8 mm.[297] Recently, improved crystallinity was demonstrated for $MAPbBr_3$ SCTFs prepared *via* a space-confined method by adjusting the growth temperature, along with the

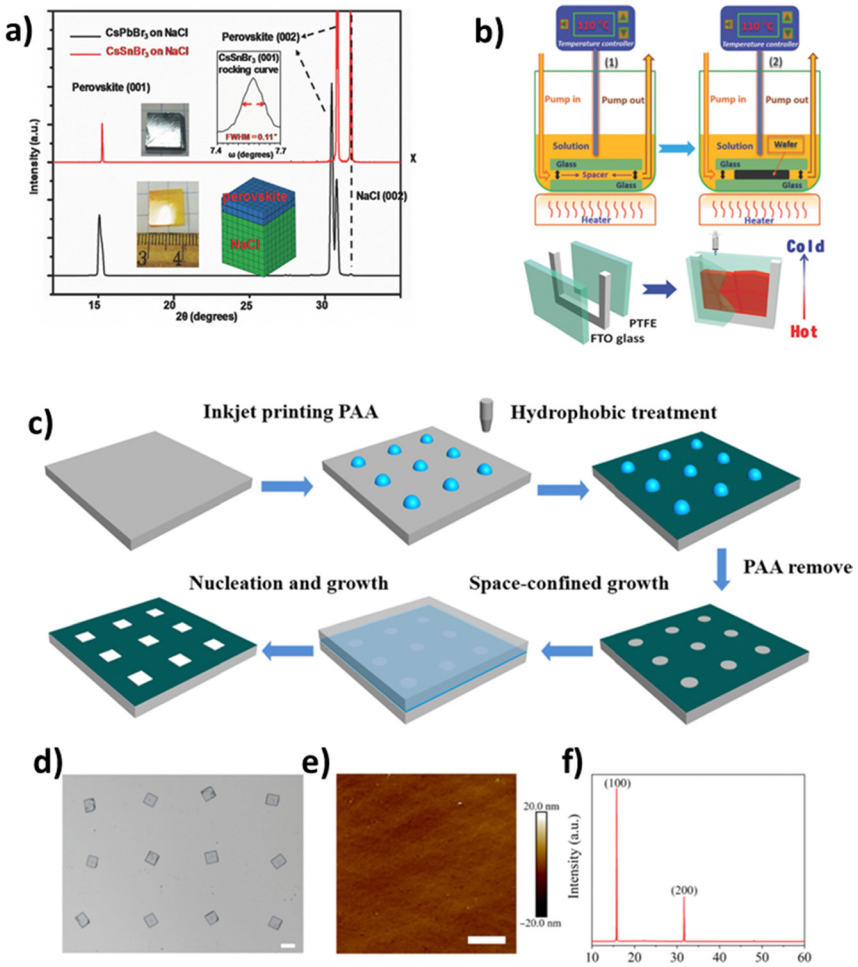

Fig. 17 (a) Structural and morphological characterization studies of VPE halide perovskites on NaCl. θ–2θ XRD analysis of $CsSnBr_3$/NaCl (red) and $CsPbBr_3$/NaCl (black). Both samples show only (100) and higher order peaks parallel to NaCl(002). The left two insets show the camera images of the mirror-like 1 cm × 1 cm film obtained after growth. The right inset shows a (001) rocking curve for $CsSnBr_3$ with a FWHM of 0.11°. Adapted with permission from ref. 292. (b) Schematic illustration of the space-confined method. Two flat glass slides are separated with two spacers to form a microreactor (top) and schematic diagram of the module to grow laminar $CH_3NH_3PbBr_3$ crystal films, whose thickness was defined by polytetrafluoroethylene (PTFE) thin membranes' thickness (bottom). Adapted with permission from ref. 294 and 296. Space-confined growth process of $MAPbCl_3$ single-crystal arrays. (c) Schematic illustration of the fabrication process of $MAPbCl_3$ single-crystal arrays. (d) Optical micrograph of the $MAPbCl_3$ single-crystal arrays. The scale bar is 50 μm. (e) AFM image of the $MAPbCl_3$ single crystal. The scale bar is 3 μm. (f) XRD pattern of the $MAPbCl_3$ single-crystal arrays. Adapted with permission from ref. 295.

$PbBr_2$/MABr molar ratio in precursors, which hindered the precipitation of the $PbBr_2$ phase. The optimum temperature and $PbBr_2$/MABr molar ratio were 50 °C and 0.85, respectively, which resulted in the formation of a ~4 mm^2 SCTF.[298]

Zhao *et al.* tried to grow a micrometer thick SCTF in the range of 3–10 μm on FTO/TiO_2 substrates, but obtained an irregular shape of $MAPbI_3$, because of the slow ion diffusion in the confined space.[298] Chen *et al.* developed a hydrophobic interface confined lateral crystal growth method, where they did grow $MAPbI_3$ SCTFs with controlled thicknesses of tens of micrometers, on HTL substrates.[300] When the film thickness was increased from 500 nm to 200 μm, they reported the expansion of the absorbance to the near-IR region. Huang *et al.* were the first to report the growth of mixed-halide, mixed-cation $(FAPbI_3)_{0.85}(MAPbBr_3)_{0.15}$ SCTFs, where they made films with various thicknesses ranging from 10 to 50 μm, through the polydimethylsiloxane-assisted solvent evaporation method.[301]

Recently Li *et al.* synthesized a laminar $MAPbBr_3$/$MAPbBr_{3-x}I_x$ heterojunction with a thickness of about 11 μm with the space-limited inverse temperature crystallization growth method and a gaseous halide exchange process in sequence, which was a new approach for growing iodide-based perovskite SCTFs.[302] In order to control the nucleation process, Gu *et al.* used a seed printing strategy, which was based on the space-confined approach, where they managed to create millimeter-sized $MAPbBr_3$ SCTFs that resulted in high yields, under controlled thickness. With the printing process, the SCTFs can be transferred to most arbitrary substrates and to scalable fabrication of photodetectors and image sensors.[303] More recently, a variety of perovskite single crystal arrays, such as $MAPbBr_3$, $CsPbCl_3$, $CsPbBr_3$, $Cs_3Cu_2I_5$, $Cs_3Bi_2I_9$, and

$(BA)_2(MA)_3Pb_4I_{11}$, were grown on Au electrodes using an inkjet-printed hydrophilic–hydrophobic substrate in the crystallization system to successfully fabricate high performance UV photodetectors.[306] Fig. 17c–f presents the schematic illustration of the space-confined growth procedure of $MAPbCl_3$ SC arrays, along with morphological and crystallinity characterization results.

4.2.3 Surface tension assisted growth. The surface tension assisted growth method is another method that is used to grow perovskite SCTFs. It was developed by Zhumekenov *et al.* who studied both theoretically and experimentally the role of surface tension in the synthesis of perovskite SCs.[48] With this method they managed to grow large-area perovskite SCTFs with thicknesses of about 5–10 μm. The versatility of this method was suitable for growing not only lead halide perovskites like $MAPbI_3$ and $MAPbBr_3$ but also tin halide perovskites like $MASnBr_3$. Fig. 18a and b shows the change in molecular interaction energies and the nucleation barrier in the volume and the surface layer of the solution, respectively. In addition, Fig. 18c illustrates the crystal growth, where the prepared film floats on the surface of the solution due to surface tension. Table 3 summarizes the electrical characteristics of PSCs using single crystal perovskites as absorbers.

Liu *et al.* modified the surface tension assisted growth method, with the introduction of a driving force by solvent evaporation.[305] They managed to grow within 30 min $MAPbI_3$ SCTFs with a lateral size of centimeters and a thickness of tens of micrometers. With this modified method, it is possible to grow SCTF crystals with a higher quality, confirmed by the long charge recombination lifetime, as measured with TRPL. In a recent work, wafer-sized 2D BA_2PbBr_4 SCTFs were grown through a gas–liquid interface crystalline route, where the crystal formed along the side parallel to the solution. Consequently, the prepared thin film buoyed on the solution surface, due to the solution surface tension.[306]

4.2.4 Top-down method. Another common method used for making perovskite SCTFs is the top-down method, where bulk perovskite SCs are reduced by using approaches like slicing, cutting and etching. This method is more suitable for large-scale fabrication and has no limitations on the method of the crystallization since there are no physical constraints, therefore offering higher-quality SCTFs. $FAPbI_3$ SCTFs prepared with this method with a thickness of 100 μm were reported by Liu *et al.*[307] They fabricated the SCTFs by slicing the bulk single crystal with a diamond wire slicing machine, as shown in Fig. 18d–g. The $FAPbI_3$ created with this method has broader absorption compared to the microcrystalline thin film, while the light emission of the single crystal was very close to the onset of the absorption, thus indicating a low trap density. Later, the same group extended their method, by growing large single-crystalline perovskites, like single-halide crystals $CH_3NH_3PbX_3$ (where X = I, Br, Cl), and dual-halide crystals

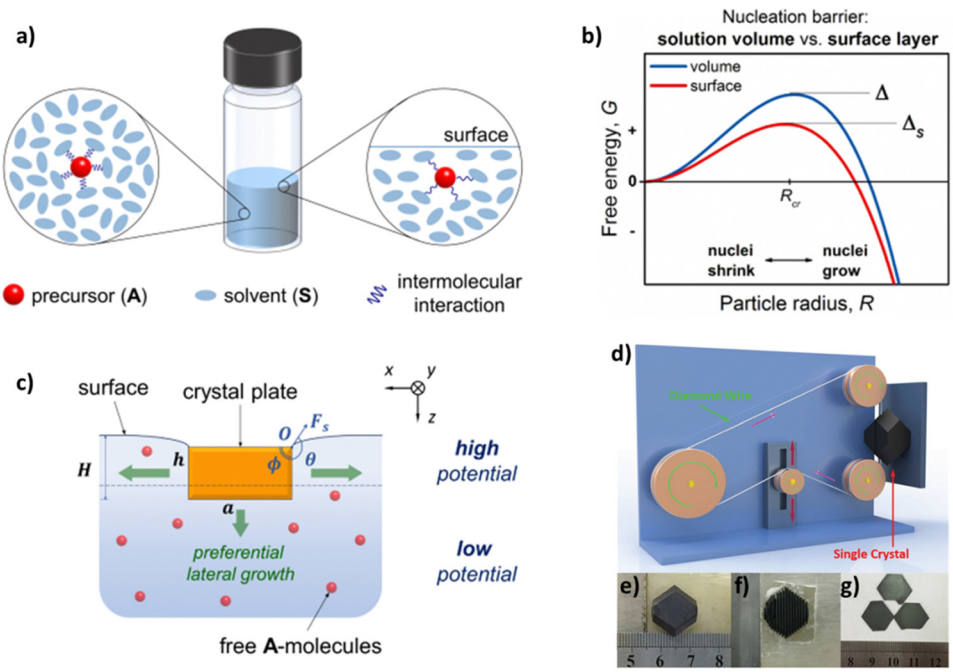

Fig. 18 (a) Schematic of change in molecular interaction energies in the volume (left) and the surface layer (right) of the solution. Due to the surface tension effect, the intermolecular distances in the surface layer are increased, hence decreasing the corresponding interaction energy. (b) Graph illustrating the lower nucleation barrier for the solution surface layer compared to that in the solution volume. (c) Schematic of crystal growth during ITC. The free precursor molecules in the surface layer (above the dashed line) are mainly attached to the sides of the nucleus (due to the higher free energy gain), resulting in lateral growth of the crystal plate. The crystal plate is kept afloat by the solution surface tension. Adapted with permission from ref. 304. (d) The schematic illustration of the single-crystalline $FAPbI_3$ wafer slicing process. (e) A $FAPbI_3$ single crystal. (f) The single-crystalline $FAPbI_3$ wafers sliced at the parallelogram natural crystallographic facets of a single-crystalline $FAPbI_3$, cross-sectional view. (g) The single-crystalline $FAPbI_3$ wafers, panoramic view. Adapted with permission from ref. 307.

Table 3 Perovskite solar cell parameters based on single crystals and the corresponding layers

Method	Perovskite	J_{SC} (mA cm^{-2})	V_{OC} (V)	FF	PCE (%)	Ref.
Droplet-pinned crystallization	$MAPbI_3$	8.7	0.52	0.38	1.73	255
ITC	$FA_{0.6}MA_{0.4}PbI_3$	26.2	1.1	0.79	22.8	270
AVC	$(NH_4)_3Sb_2I_xBr_{9-x}$	1.15	1.03	0.4288	0.51	283
Space-confined method	$MAPbBr_3$	8.77	1.31	0.62	7.11	297
Space-confined method	$MAPbI_3$	22.28	0.67	0.59	8.78	299
Space-confined method	$MAPbI_3$	20.5	1.06	0.741	16.1	300
Space-confined method	$(FAPbI_3)_{0.85}(MAPbBr_3)_{0.15}$	23.14	1.03	0.51	12.18	301
Space-confined method	$MAPbI_3$	5.06	0.66	0.44	5.9	304

$CH_3NH_3Pb(Cl_xBr_{1-x})_3$ and $CH_3NH_3Pb(Br_xI_{1-x})_3$, where the largest crystal had a length of 120 mm.[308] Lv *et al.* prepared thickness- and orientation-controllable perovskite SCTFs by using a universally applicable top-down method, where the thickness could be controlled from the millimeter level up to 15 micrometers.[309] This method is applicable to various perovskite materials, like $MAPbI_3$, $MAPbCl_3$ and $MAPbBr_3$, while controlling not only the thickness but also the orientation of the thin film.

5. Synthetic methods for 2D perovskites

The fundamental characteristics and device applications of 2D perovskites depend a lot on how they are synthesized in a controlled manner. Up to this point, several types of ultra-thin perovskites have been synthesized by utilizing various methods. In this section we will describe the current developments in the synthesis of 2D perovskites.

5.1 Inorganic 2D perovskites

The colloidal synthesis method is one of the most used approaches for producing 2D inorganic halide perovskites.[310–313] Fig. 19 shows the structural analysis of the $CsPbBr_3$ nanoplatelets formed through solution synthesis. While nanoplatelets might be produced at comparatively lower temperatures, reactions carried out above 150 °C would mostly result in nanocubes. At 130 °C, for example, nanoplatelets with lateral dimensions of 20 nm and a thickness of around 3 nm can be produced. $CsPbI_3$ and $CsPbCl_3$ nanoplatelets may be generated using anion exchange, and for device applications, they can be deposited onto substrates using the centrifugal casting process.[311] The lateral size, however, is only around 20–300 nm, which is small for the assessment of the basic characteristics of a single nanosheet and the manufacture of devices. By dissolving Cs-oleate in oleic acid and adding short ligands, Shamsi *et al.* discovered that they could create $CsPbBr_3$ ultra-thin rectangular shaped sheets of 3 nm and lateral dimensions ranging from 300 nm to 5 μm.[312] High-quality 2D $CsPbI_3$ perovskite nanosheets were produced by the space-confined vapor deposition approach by Zhai *et al.* By altering the growth temperature and distance, the 2D $CsPbI_3$ perovskite's shape and crystal quality may be easily regulated. 2D $CsPbI_3$ nanosheets are uniformly square-shaped and have a thickness of 6 nm and a side length of 10 μm, while the photoluminescence emission characteristics show a clear reliance on the 2D $CsPbI_3$ nanosheets' thickness.[313]

$Cs_2PbCl_2I_2$ nanosheets doped with Mn^{2+} were synthesized by Li *et al.* and Dutta *et al.* by an acid solution-assisted method resulting in all-inorganic 2D perovskites with ordered mixed halides.[314,315] They showed that an efficient method to improve the photoluminescence characteristics of $Cs_2PbCl_2I_2$ nanocrystals is to introduce appropriate Mn^{2+} together with Pb^{2+} into the crystals, which resulted in a higher PLQY of 16%. Note that the 2D $CsPbX_3$ nanoplatelets correspond to the morphological structure of the perovskite, while the $Cs_2PbCl_2I_2$ nanosheets are attributed to the molecular level.

A variety of inorganic lead perovskites can also be synthesized using CVD. Mica was used as the substrate by Zhang *et al.*, who employed the van der Waals epitaxial CVD technique for the fabrication of $CsPbX_3$ nanoplatelets.[316] The perovskite nanoplatelets were relatively thick, ranging in thicknesses from 50 to 300 nm, although having fairly considerable lateral dimensions in the range of 1–20 μm. Some studies have conclusively shown that all-inorganic 2D perovskites of cesium lead halides have comparatively poor mobility, which is mostly due to the extremely low frequency of the Pb-I vibrations. This finding suggests that combined Pb/Sn- or Sn-based perovskites with the light components of Cl or Br should be viewed as better materials.[317,318]

5.2 Solution synthesis of 2D perovskites

The majority of 2D halide perovskites are created using hydrohalic acid solution synthesis, while multilayered 2D perovskites can be fabricated using this technique very effectively.[319–322] Serving both as a solvent and as a halide source, hydrohalic acid must be compatible with the type of halide in the target perovskite. Under heating and stirring, the metal source, spacer (or spacer salt), and A-site cation salt dissolve, resulting in the ionization of all three components. To produce the desired crystal, the desired solution must be cooled to room temperature after it becomes clear. The perovskite with the same halide will be produced regardless of the anions in the metal source and cation salts because there is a significant excess of halide in the solution. The general rule is that substances with higher organic content are less soluble and will crystallize more quickly than substances with higher solubility. The solubility of the $n = 1$ compound determines the ratio of the spacer and Pb sources, which can be used to adjust the layer-number.[323] Iodide perovskites can occasionally produce a light-yellow

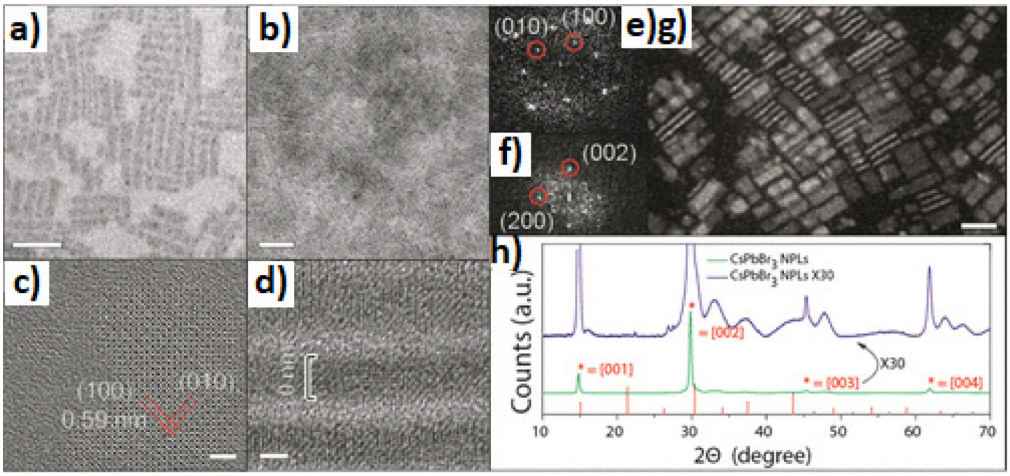

Fig. 19 Structural analysis of $CsPbBr_3$ NPLs emitting at 460 nm. TEM images of $CsPbBr_3$ NPLs at (a) low concentrations and (b) high concentrations. HRTEM images of NPLs (c) in top view and (d) in stacks as well as their respective Fourier transform patterns (e and f). (g) STEM dark-field image of NPLs. (h) XRD patterns of $CsPbBr_3$ NPLs. Reference pattern of cubic $CsPbBr_3$, ICSD 29073. Scale bars correspond to 50 nm in (a) and (b), 2 nm in (c) and (d), and 20 nm in (g). Adapted with permission from ref. 310.

hydrate phase instead of the desired perovskite phase if the hot solution is quickly cooled to room temperature. This step-cooling technique can be used in some circumstances to obtain the 2D phase. The solution can be heated to 125 °C, which is just below the boiling point of HI, so that it is hot and the light-yellow phase can continue to be soluble after all of the initial ingredients have been dissolved under stirring and boiling. The desired 2D phase can still precipitate out because the solution is extremely concentrated. Iodide perovskites can act as crystal growth seeds once the first few crystals begin to precipitate out, while a second precipitation phase would not occur if the temperature were gradually lowered to room temperature (Fig. 20).[324–326]

Organic solvents, including *N*,*N*-dimethylformamide (DMF), dimethyl sulfoxide (DMSO), and γ-butyrolactone (GBL), as well as mixtures of the aforementioned solvents, can also be used to create 2D halide perovskites.[46,326] Most organic and inorganic salts can be dissolved using these polar solvents, and they may also work for cations that are insoluble in HI. Some 3D halide perovskites become less soluble in organic solvents as the temperature increases; as a result, the crystal can precipitate out when using this method, as it necessitates a thorough examination of each compound's solubility with temperature, which may differ from spacer to spacer.[327] A large single crystal can also form by maintaining a constant solution temperature and allowing the solvent to slowly evaporate.[328] Sometimes the decrease in solubility caused by a temperature change or solvent evaporation is insufficient to cause the crystal to precipitate. In these circumstances, the precipitation process can be sped up by gradually adding an antisolvent. A stoichiometric ratio of starting materials is dissolved in a small vial with a "good solvent," much like solution synthesis using an organic solvent like DMF or DMSO. The vial with the cap open is then placed into a larger vial that contains a "poor solvent," such as ethyl ether or dichloromethane, which serves as the antisolvent. The solubility of the perovskite phase decreases as the "poor solvent" gradually diffuses into the "good solvent," and crystals may precipitate out.[329–331]

5.3 Substrate growth

Halide perovskites can be produced directly by the evaporation of their precursor solution on a substrate like silicon or glass in the form of atomically flat 2D sheets. On the substrate, the kinetics of crystal growth are significantly influenced by the rate of solvent evaporation. The 2D halide perovskite structures' overall quality and thickness are consequently influenced by the polarity of the solvents used to dissolve the precursors, the solvent volume ratio, the crystallization temperature, and the make-up of the substrate surface.[332–334]

By drop-casting the precursor solution onto a Si/SiO_2 substrate at a moderate temperature, Yang and colleagues were able to showcase the growth of single-crystalline $(BA)_2PbBr_4$ perovskites. As a ternary co-solvent to dissolve the precursors, DMF–chlorobenzene–acetonitrile was used to regulate the thickness of the 2D perovskite sheets. Fast acetonitrile evaporation induces the formation and growth of ultrathin 2D perovskite sheets, whereas chlorobenzene decreases the solubility of halide perovskites in DMF and encourages crystallization.[335]

Another effective method for creating uniform, superior-quality films of 2D halide perovskites is spin-coating.[333,336] Perovskite layers are typically deposited using this technique for the construction of devices like solar cells and LEDs. To create layered 2D halide perovskites, the precursors dissolved in DMF or DMSO are spin-coated on glass or ITO substrates in a single step or multiple steps, followed by ambient drying or annealing. In order to create perovskite solar cells, Smith *et al.* demonstrated the one-step spin coating of high-quality perovskite films.[337] The SEM cross sectional image of the corresponding perovskite solar cell and the *J*–*V* characteristic curves are presented in Fig. 21a and b, respectively. The selective thickness of these 2D materials is largely determined by crystallization dynamics during the film growth in addition to

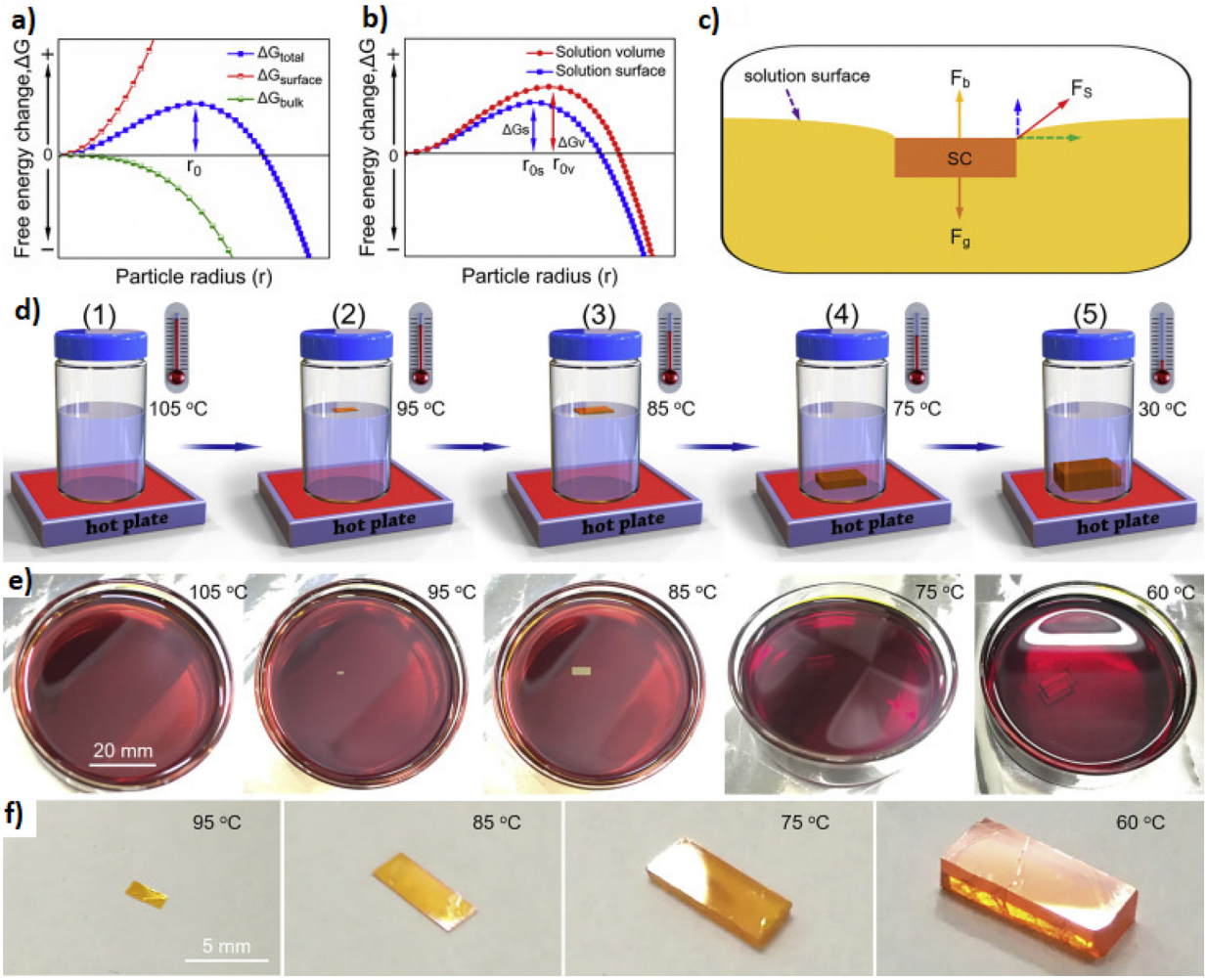

Fig. 20 Crystallization of $(PEA)_2PbI_4$ PSCs. (a) The Gibbs free energy change ΔG_{total} as a function of particle radius. ΔG_{total} consists of a surface term ΔG_s and a bulk term ΔG_b. (b) Graph illustrating the lower nucleation barrier for the solution surface compared with that in the solution volume. (c) Schematic of the single crystal staying afloat on the solution surface. (d) Schematic of the surface tension-controlled crystallization process. (e) Photographs of the $(PEA)_2PbI_4$ PSCs grown at different temperatures. (f) Corresponding photographs of $(PEA)_2PbI_4$ PSCs completed at different temperatures. Adapted with permission from ref. 326.

the stoichiometric ratio of precursors and the size of organic cations.[332] For instance, 2D halide perovskites made by quickly crystallizing stoichiometric precursors in DMF *via* spin coating and immediately annealing them at a high temperature do not always have stacking layers with a single value of *n*. They might include a variety of 2D layers with various *n*. On the other hand, Zhang *et al.* used a binary mixture of solvents as the precursors for perovskites.[338] Toluene is a poor solvent that is known to cause the precipitation of perovskite crystals, whereas acetonitrile is a suitable solvent for the precursors. The controlled synthesis of 2D RP perovskites on substrates is made possible by the two solvents' perfect miscibility in this situation, which could cause them to co-evaporate slowly at room temperature. As a result, nanosheets with various thicknesses were successfully produced.

5.4 Exfoliation method

Since 2D RP perovskites have a van der Waals layered crystal structure, mechanical exfoliation can easily produce atomically thin layers of perovskites, just as it can with other conventional 2D materials like graphene.[339] Niu *et al.* were able to produce from one to multiple layers of flakes by employing the micromechanical exfoliation technique.[340] In order to study the fundamental properties of quasi-2D perovskites with various layer numbers, this synthesis method is ideally suited.[341] However, due to the lack of size and thickness control over the obtained flakes, it cannot be widely used, and as a result, new techniques for creating atomically thin 2D RP perovskites were created.

Another way to create 2D structures that are as thin as atoms is by repeatedly peeling a bulk perovskite crystal that has been adhered between the adhesive sides of two scotch tape strips.[84,342]

By applying pressure to a substrate with the scotch tape, the resulting 2D halide perovskite layers are transferred there. It is simple to create 2D halide perovskites using this method, but it is frequently challenging to precisely control the thickness of the inorganic layers; therefore the 2D halide perovskites made

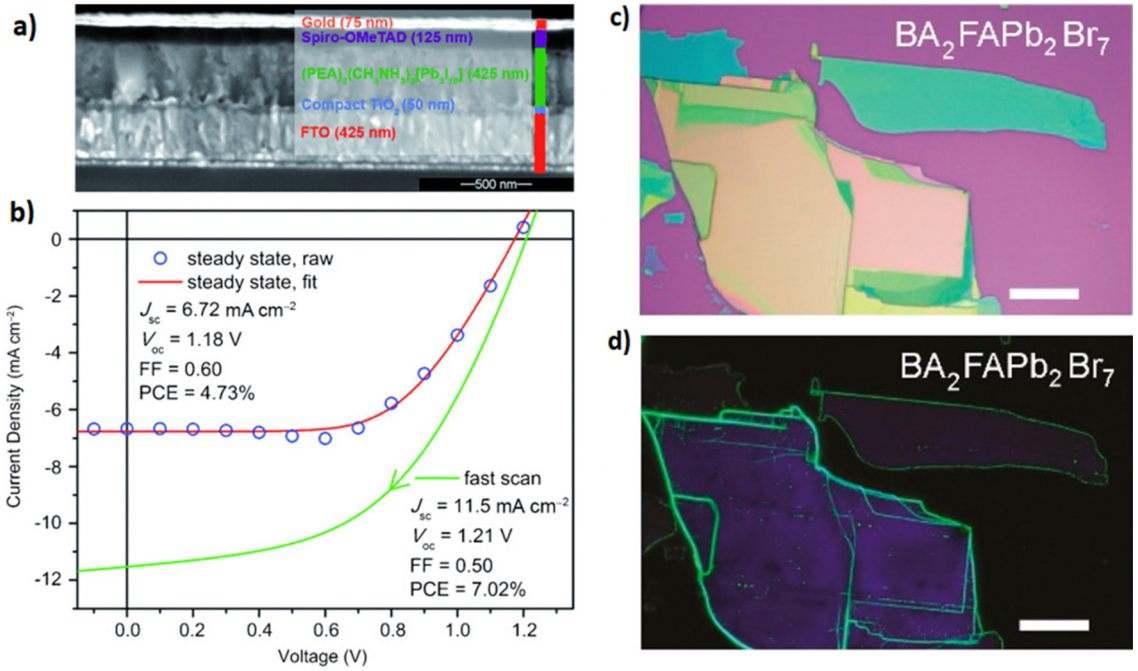

Fig. 21 (a) SEM cross-sectional image and device configuration of planar devices utilizing $(PEA)_2(MA)_2[Pb_3I_{10}]$ as the absorber layer. Scale bar = 500 nm. (b) Current–voltage (*J*–*V*) curves for the devices fabricated as given in (a). Adapted with permission from ref. 337. (c and d) Optical and PL images of a series of 2D $BA_2FAPb_2Br_7$ lead halide perovskites mechanically exfoliated on SiO_2/Si substrates. Adapted with permission from ref. 342.

using the Scotch tape method are mechanically fragile, and their stability and photoluminescence quantum yield (PLQY) can be affected by the fractured surface (Fig. 21c and d). Yun *et al.* recently demonstrated ligand-assisted ball milling for mechanically exfoliating perovskite crystals to produce quasi-2D structures with improved PLQYs and stability.[343]

Furthermore, liquid exfoliation has been used to create 2D RP perovskites from 3D perovskites by incorporating the long chain molecules into the 3D perovskite structures. OlA was an oleylamine cation, and X was Cl, Br, or I when Hintermayr *et al.* reported the synthesis of $OlA_2MA_{n-1}Pb_nX_{3n+1}$. $MAPbX_3$ microcrystal powder was first dissolved in toluene with OlA and subjected to tip sonication during the procedure. The large particles were then centrifuged out, resulting in nanoplate dispersion.[344] Exfoliating perovskite nanocrystals with a solvent or using sonication in the presence of many surface ligands results in colloidally stable ultrathin 2D halide perovskites.[345]

By diluting the colloidal nanocrystal solution, solvent-assisted exfoliation produces nanoplatelets of halide perovskites. The excess ligand molecules that are already present in or are later added penetrate the interlayer region and stabilize the newly formed surface as a result of the increase in osmotic swelling of nanocrystals caused by the solvent molecules at higher dilutions, which causes their fragmentation into nanoplatelets. Urban *et al.* showed that altering the level of dilution or ligand concentration caused perovskite nanocrystals to fragment into stable nanoplatelets of various thicknesses.[346] Sonication is one external stimulus that can cause larger nanocrystals to break up into quasi-2D structures. Instead of diluting the nanocrystals, sonication in this case breaks them up into thin perovskite layers, allowing the organic ligands to pass through and interact with the newly formed facets, and then by centrifugation at various speeds, the 2D perovskite nanoplatelets with various thicknesses are separated.[344]

Table 4 Perovskite solar cell parameters based on 2D RP phase perovskites

Method	Perovskite	J_{SC} (mA cm^{-2})	V_{OC} (V)	FF	PCE (%)	Ref.
Solution synthesis	$(CH_3(CH_2)_2NH_3)_2(CH_3NH_3)_5Pb_6I_{19}$	16.30	1.05	0.7539	10.9	319
Solution synthesis	$(CH_3(CH_2)_2NH_3)_2(CH_3NH_3)_6Pb_7I_{22}$	16.73	0.95	0.5603	8.93	319
Solution synthesis	$(CH_3(CH_2)_2NH_3)_2(CH_3NH_3)_8Pb_9I_{28}$	21.84	0.801	0.7219	12.63	319
Solution synthesis	$(CH_3(CH_2)_3NH_3)_2(CH_3NH_3)_4Pb_5I_{16}$	11.44	1.00	0.7559	8.71	320
Solution synthesis	$(ThMA)_2FA_4Pb_5I_{16}$	23.39	1.075	0.758	19.06	324
Solvent evaporation	$(iso\text{-}BA)_2(MA)_4Pb_5I_{16}$	18.1	1.15	0.772	16.0	332
Spin-coating	$BA_2MA_3Pb_4I_{13}$	11.3	1.07	0.648	7.9	336
Slow-solvent evaporation	$(PEA)_2(MA)_2[Pb_3I_{10}]$	6.72	1.18	0.60	4.73	337
Sonication	$(CH_3(CH_2)_3NH_3)_2(CH_3NH_3)_3Sn_4I_{13}$	24.1	0.229	0.457	2.53	347

5.5 Grinding method

Solid-state grinding is a technique that can be used to completely eliminate solvent effects. For 3D halide perovskites, this is first accomplished by stoichiometrically grinding the raw materials in a mortar and pestle, then annealing the mixture to produce the desired phase. In particular, 2D perovskites that cannot be produced in solution, because the spacers are too soluble or insoluble, can be produced using this method.[235,242,347] This method's advantage is that it can create 2D perovskites regardless of how soluble a spacer is. It is a good way to determine whether a spacer can create a 2D perovskite (if the solution synthesis does not work). This technique has not yet been used to synthesize 2D perovskites with more $n > 3$. Table 4 summarizes the electrical parameters of PSCs based on 2D perovskites.

6. Conclusions

In this review, we have summarized the synthetic approaches followed for the deposition of polycrystalline perovskite films and the growth of perovskite single crystals and their corresponding layers. The fabrication of high-quality perovskite layers has been recapitulated to be dependent on the synthetic method adopted. Various vacuum or solution based synthetic methods are effective and mature ways to fabricate high-quality polycrystalline films favorable for different applications. The carrier diffusion length, presence of defects, absorption coefficient and other optoelectronic properties are strongly related to the quality of the deposited film. Similarly, the growth of perovskite single crystals, 2D perovskites and the corresponding layers depends on the synthetic method applied and influences their effective material properties.

All these methods can be manipulated in order to minimise perovskite destroying defects. The low stability of perovskite optoelectronics is attributed to the intrinsic low formation energy of the 3D perovskite lattice. This leads to defect formation (uncoordinated halide ions, cation vacancies), which can migrate through the perovskite and cause perovskite-destabilising redox reactions catalysed by water, oxygen, light, temperature or the applied electric field. Recently, the paramount importance of strain (mechanical deformation of the crystal lattice) in halide perovskites was highlighted since it can be tuned to improve the thermodynamic stability of perovskites or locally alter defect dynamics and charge transfer. By using suitable synthetic protocols combined with *in situ* strain engineering and/or chemical passivation approaches perovskite layers with improved properties can be obtained.

The potential of perovskites for creating higher efficiency optoelectronic devices has been unambiguously demonstrated. Halide perovskite materials offer excellent light absorption and charge-carrier mobilities, resulting in high device efficiencies with opportunities to realise a low-cost, industry-scalable technology. Achieving this potential requires that a suitable deposition method be followed for the fabrication of perovskite functional layers. A large variety of deposition methods have been already explored with great success in terms of device efficiency. However, they perhaps need to overcome barriers related to stability, environmental compatibility, and reproducibility. If the existing synthetic approaches can be modified in order for these concerns to be effectively addressed, perovskite-based technology holds transformational potential for rapid terawatt-scale solar deployment, efficient solid state lighting, field-effect transistor and memory applications and beyond.

Conflicts of interest

There are no conflicts to declare.

References

1 D. A. Egger, A. Bera, D. Cahen, G. Hodes, T. Kirchartz, L. Kronik, R. Lovrincic, A. M. Rappe, D. R. Reichman and O. Yaffe, *Adv. Mater.*, 2018, **30**, e1800691.
2 J. Knutson, J. D. Martin and D. B. Mitzi, *Inorg. Chem.*, 2005, **44**, 4699–4705.
3 Y. Fang, Q. Dong, Y. Shao, Y. Yuan and J. Huang, *Nat. Photonics*, 2015, **9**, 679–686.
4 M. A. Green, A. Ho-Baillie and H. J. Snaith, *Nat. Photonics*, 2014, **8**, 506–514.
5 G. Xing, N. Mathews, S. Sun, S. S. Lim, Y. M. Lam, M. Grätzel, S. Mhaisalkar and T. C. Sum, *Science*, 2013, **342**, 344–347.
6 M.-C. Tang, H. X. Dang, S. Lee, D. Barrit, R. Munir, K. Wang, R. Li, D.-M. Smilgies, S. De Wolf, D.-Y. Kim, T. D. Anthopoulos and A. Amassian, *Solar RRL*, 2021, **5**, 2000718.
7 W. J. Yin, T. Shi and Y. Yan, *Adv. Mater.*, 2014, **26**, 4653–4658.
8 Q. Han, Y. Bai, J. Liu, K.-Z. Du, T. Li, D. Ji, Y. Zhou, C. Cao, D. Shin, J. Ding, A. D. Franklin, J. T. Glass, J. Hu, M. J. Therien, J. Liu and D. B. Mitzi, *Energy Environ. Sci.*, 2017, **10**, 2365–2371.
9 Y. Zhai, K. Wang, F. Zhang, C. Xiao, A. H. Rose, K. Zhu and M. C. Beard, *ACS Energy Lett.*, 2020, **5**, 47–55.
10 A. Biewald, N. Giesbrecht, T. Bein, P. Docampo, A. Hartschuh and R. Ciesielski, *ACS Appl. Mater. Interfaces*, 2019, **11**, 20838–20844.
11 S. D. Wolf, J. Holonsky, S.-J. Moon, P. Loper, B. Niesen, M. Ledinsky, F.-J. Haug, J.-H. Yum and C. Ballif, *J. Phys. Chem. Lett.*, 2014, **5**, 1035–1039.
12 M. Delor, A. H. Slavney, N. R. Wolf, M. R. Filip, J. B. Neaton, H. I. Karunadasa and N. S. Ginsberg, *ACS Energy Lett.*, 2020, **5**, 1337–1345.
13 S. D. Stranks, G. E. Eperon, G. Grancini, C. Menelaou, M. J. P. Alcocer, T. Leijtens, L. M. Herz, A. Petrozza and H. J. Snaith, *Science*, 2013, **342**, 341–344.
14 Q. Dong, Y. Fang, Y. Shao, P. Mulligan, J. Qiu, L. Cao and J. Huang, *Science*, 2015, **347**, 967–970.
15 M. Saliba, T. Matsui, J. Y. Seo, K. Domanski, J. P. Correa-Baena, M. K. Nazeeruddin, S. M. Zakeeruddin, W. Tress,

A. Abate, A. Hagfeldt and M. Grätzel, *Energy Environ. Sci.*, 2016, **9**, 1989–1997.
16 M. Saliba, T. Matsui, K. Domanski, J.-Y. Seo, A. Ummadisingu, S. M. Zakeeruddin, J.-P. Correa-Baena, W. Tress, A. Abate, A. Hagfeldt and M. Grätzel, *Science*, 2016, **354**, 206–209.
17 W. S. Yang, J. H. Noh, N. J. Jeon, Y. C. Kim, S. Ryu, J. Seo and S. I. Seok, *Science*, 2015, **348**, 1234–1237.
18 S. S. Shin, E. J. Yeom, W. S. Yang, S. Hur, M. G. Kim, J. Im, J. Seo, J. H. Noh and S. I. Seok, *Science*, 2017, **356**, 167–171.
19 M. Abdi-Jalebi, M. I. Dar, A. Sadhanala, S. P. Senanayak, M. Franckevičius, N. Arora, Y. Hu, M. K. Nazeeruddin, S. M. Zakeeruddin, M. Gratzel and R. H. Friend, *Adv. Energy Mater.*, 2016, **6**, 1502472.
20 C. Bi, X. Zheng, B. Chen, H. Wei and J. Huang, *ACS Energy Lett.*, 2017, **2**, 1400–1406.
21 M. Era, S. Morimoto, T. Tsutsui and S. Saito, *Appl. Phys. Lett.*, 1994, **65**, 676–678.
22 T. Hattori, T. Taira, M. Era, T. Tsutsui and S. Saito, *Chem. Phys. Lett.*, 1996, **254**, 103–108.
23 K. Chondroudis and D. B. Mitzi, *Chem. Mater.*, 1999, **11**, 3028–3030.
24 H. Cho, S.-H. Jeong, M.-H. Park, Y.-H. Kim, C. Wolf, C.-L. Lee, J. H. Heo, A. Sadhanala, N. Myoung, S. Yoo, S. H. Im, R. H. Friend and T.-W. Lee, *Science*, 2015, **350**, 1222–1225.
25 M. Yuan, L. N. Quan, R. Comin, G. Walters, R. Sabatini, O. Voznyy, S. Hoogland, Y. Zhao, E. M. Beauregard, P. Kanjanaboos, Z. Lu, D. H. Kim and E. H. Sargent, *Nat. Nanotechnol.*, 2016, **11**, 872–877.
26 C. R. Kagan, D. B. Mitzi and C. D. Dimitrakopoulos, *Science*, 1999, **286**, 945–947.
27 D. B. Mitzi, C. D. Dimitrakopoulos and L. L. Kosbar, *Chem. Mater.*, 2001, **13**, 3728–3740.
28 D. B. Mitzi, C. D. Dimitrakopoulos, J. Rosner, D. R. Medeiros, Z. Xu and C. Noyan, *Adv. Mater.*, 2002, **14**, 1772–1776.
29 H. P. Kim, M. Vasilopoulou, H. Ullah, S. Bibi, A. E. X. Gavim, A. G. Macedo, W. J. da Silva, F. K. Schneider, A. A. Tahir, M. A. M. Teridi, P. Gao, A. R. B. M. Yusoff and M. K. Nazeeruddin, *Nanoscale*, 2020, **12**, 7641–7650.
30 K. Kang, W. Hu and X. Tang, *J. Phys. Chem. Lett.*, 2021, **12**, 11673–11682.
31 Y. Yao, Y. Peng, L. Li, X. Zhang, X. Liu, M. Hong and J. Luo, *Angew. Chem.*, 2021, **60**, 10598–10602.
32 Y. Zhang, S. Poddar, H. Hang, L. Gu, Q. Zhang, Y. Zhou, S. Yan, S. Zhang, Z. Song, B. Huang, G. Shen and Z. Fan, *Sci. Adv.*, 2021, **7**, eabg3788.
33 M. Vasilopoulou, B. S. Kim, H. P. Kim, W. J. da Silva, F. K. Schneider, M. A. M. Teridi, P. Gao, A. R. B. M. Yusoff and M. K. Nazeeruddin, *Nano Lett.*, 2020, **20**, 5081–5089.
34 T. Zhang, M. Yang, E. E. Benson, Z. Li, J. van de Lagemaat, J. M. Luther, Y. Yan, K. Zhu and Y. Zhao, *Chem. Commun.*, 2015, **51**, 7820–7823.
35 O. Knop, R. E. Wasylishen, M. A. White, T. S. Cameron and M. J. V. Oort, *Can. J. Chem.*, 1990, **68**, 412–422.
36 W. J. Yin, Y. Yan and S. H. Wei, *J. Phys. Chem. Lett.*, 2014, **5**, 3625–3631.
37 Y. Fang, Q. Dong, Y. Shao, Y. Yuan and J. Huang, *Nat. Photonics*, 2015, **9**, 679–686.
38 R. Babu, L. Giribabu and S. P. Singh, *Cryst. Growth Des.*, 2018, **18**, 2645–2664.
39 G. Maculan, A. D. Sheikh, A. L. Abdelhady, M. I. Saidaminov, M. A. Haque, B. Murali, E. Alarousu, O. F. Mohammed, T. Wu and O. M. Bakr, *J. Phys. Chem. Lett.*, 2015, **6**, 3781–3786.
40 M. Volmer and A. Weber, *Phys. Chem.*, 1926, **119**, 277–301.
41 Z.-K. Tan, R. S. Moghaddam, M. L. Lai, P. Docampo, R. Higler, F. Deschler, M. Price, A. Sadhanala, L. M. Pazos, D. Credgington and F. Hanusch, *Nat. Nanotechnol.*, 2014, **9**, 687–692.
42 M. M. Lee, J. Teuscher, T. Miyasaka, T. N. Murakami and H. J. Snaith, *Science*, 2012, **338**, 643–647.
43 J. Frenkel, *J. Chem. Phys.*, 1939, **7**, 538–547.
44 L. Chen, Y.-Y. Tan, Z.-X. Chen, T. Wang, S. Hu, Z.-A. Nan, L.-Q. Xie, Y. Hui, J.-X. Huang, C. Zhan, S.-H. Wang, J.-Z. Zhou, J.-W. Yan, B.-W. Mao and Z.-Q. Tian, *J. Am. Chem. Soc.*, 2019, **141**, 1665–1671.
45 S. Kawachi, M. Atsumi, N. Saito, N. Ohashi, Y. Murakami and J.-I. Yamaura, *J. Phys. Chem. Lett.*, 2019, **10**, 6967–6972.
46 Y. Liu, Z. Yang, D. Cui, X. Ren, J. Sun, X. Liu, J. Zhang, Q. Wei, H. Fan, F. Yu, X. Zhang, C. Zhao and S. F. Liu, *Adv. Mater.*, 2015, **27**, 5176–5183.
47 J. M. Kadro, K. Nonomura, D. Gachet, M. Grätzel and A. Hagfeldt, *Sci. Rep.*, 2015, **5**, 11654.
48 A. A. Zhumekenov, V. M. Burlakov, M. I. Saidaminov, A. Alofi, M. A. Haque, B. Turedi, B. Davaasuren, I. Dursun, N. Cho, A. M. El-Zohry, M. D. Bastiani, A. Giugni, B. Torre, E. Di Fabrizio, O. F. Mohammed, A. Rothenberger, T. Wu, A. Goriely and O. M. Bakr, *ACS Energy Lett.*, 2017, **2**, 1782–1788.
49 M. I. Saidaminov, A. L. Abdelhady, G. Maculan and O. M. Bakr, *Chem. Commun.*, 2015, **51**, 17658–17661.
50 T. Baikie, Y. Fang, J. M. Kadro, M. Schreyer, F. Wei, S. G. Mhaisalkar, M. Graetzel and T. J. White, *J. Mater. Chem. A*, 2013, **1**, 5628–5641.
51 C. C. Stoumpos and M. G. Kanatzidis, *Acc. Chem. Res.*, 2015, **48**, 2791–2802.
52 X. Zhang, J.-X. Shen and C. G. Van de Walle, *Adv. Energy Mater.*, 2020, **10**, 1902830.
53 G. Kieslich, S. Sun and A. K. Cheetham, *Chem. Sci.*, 2014, **5**, 4712–4715.
54 V. M. Goldschmidt, *Naturwissenschaften*, 1926, **14**, 477–485.
55 Z. Li, M. Yang, J.-S. Park, S.-H. Wei, J. J. Berry and K. Zhu, *Chem. Mater.*, 2016, **28**, 284–292.
56 J.-W. Lee, S. Tan, S. I. L. Seok, Y. Yang and N. G. Park, *Science*, 2022, **375**, 6583.
57 B. Conings, J. Drijkoningen, N. Gauquelin, A. Babayigit, J. D'Haen, L. D'Olieslaeger, A. Ethirajan, J. Verbeeck, J. Manca, E. Mosconi, F. De Angelis and H.-G. Boyen, *Adv. Energy Mater.*, 2015, **5**, 1500477.

58 X. Li, M. Ibrahim Dar, C. Yi, J. Luo, M. Tscumi, S. M. Zakeeruddin, M. K. Nazeeruddin, H. Han and M. Grätzel, *Nat. Chem*, 2015, **7**, 703–711.
59 N. K. Kim, Y. H. Min, S. Noh, E. Cho, G. Jeong, M. Joo, S.-W. Ahn, J. S. Lee, S. Kim, K. ihm, H. Ahn, Y. Kang, H.-S. Lee and D. Kim, *Sci. Rep.*, 2017, **7**, 4645.
60 G. E. Eperon, C. E. Beck and H. J. Snaith, *Mater. Horiz.*, 2016, **3**, 63.
61 X. Zheng, C. Wu, S. K. Jha, Z. Li, K. Zhu and S. Priya, *ACS Energy Lett.*, 2016, **1**, 1014–1020.
62 N. Pellet, P. Gao, G. Gregori, T.-Y. Yang, M. K. Nazeeruddin, J. Maier and M. Grätzel, *Angew. Chem., Int. Ed.*, 2014, **53**, 3151–3221.
63 F. Brivio, C. Caetano and A. Walsh, *J. Phys. Chem. Lett.*, 2016, **7**, 1083–1087.
64 K. Tanaka, T. Takahashi, T. Ban, T. Kondo, K. Uchida and N. Miura, *Solid State Commun.*, 2003, **127**, 619–623.
65 Y. Cho, A. M. Soufiani, J. S. Yun, J. Kim, D. S. Lee, J. Seidel, X. Deng, M. A. Green, S. Huang and A. W. Y. Ho-Baillie, *Adv. Energy Mater.*, 2018, **8**, 1703392.
66 N. Li, S. Tao, Y. Chen, X. Niu, C. K. Onwudinanti, C. Hu, Z. Qiu, Z. Xu, G. Zheng, L. Wang, Y. Zhang, L. Li, H. Liu, Y. Lun, J. Hong, X. Wang, Y. Liu, H. Xie, Y. Gao, Y. Bai, S. Yang, G. Brocks, Q. Chen and H. Zhou, *Nat. Energy*, 2019, **4**, 408–415.
67 P. K. Nayak, D. T. Moore, B. Wenger, S. Nayak, A. A. Haghihgirad, A. Fineberg, N. K. Noel, O. G. Reid, G. Rumbles, P. Kukura, K. A. Vincent and H. J. Snaith, *Nat. Commun.*, 2016, **7**, 13303.
68 J. Jeong, M. Kim, J. Seo, H. Lu, P. Ahlawat, A. Mishra, Y. Yang, M. A. Hope, F. T. Eickemeyer, M. Kim, Y. J. Yoon, I. W. Choi, B. P. Darwich, S. J. Choi, Y. Jo, J. H. Lee, B. Walker, S. M. Zakeeruddin, L. Emsley, U. Rothlisberger, A. Hagfeldt, D. S. Kim, M. Grätzel and J. Y. Kim, *Nature*, 2021, **592**, 381–385.
69 Y. Zhao, F. Ma, Z. Qu, S. Yu, T. Shen, H.-X. Deng, X. Peng, Y. Yuan, X. Zhang and J. You, *Science*, 2022, **377**, 531–534.
70 Q. Jiang, J. Tong, Y. Xian, R. A. Kerner, S. P. Dunfield, C. Xiao, R. A. Scheidt, D. Kuciauskas, X. Wang, M. P. Hautzinger, R. Tirawat, M. C. Beard, D. P. Fenning, J. J. Berry, B. W. Larson, Y. Yan and K. Zhu, *Nature*, 2022, **611**, 278–283.
71 R. Comin, G. Walters, E. S. Thibau, O. Voznyy, Z. H. Lu and E. H. Sargetnt, *J. Mater. Chem. C*, 2015, **3**, 8839–8843.
72 W.-J. Yin, T. Shi and Y. Yan, *Appl. Phys. Lett.*, 2014, **104**, 063903.
73 H. Jin, E. Debroye, M. Keshavarz, I. G. Scheblykin, M. B. J. Roeffaers, J. Hofkens and J. A. Steele, *Mater. Horiz.*, 2020, **7**, 397–410.
74 M. Rahil, R. M. Ansari, C. Prakash, S. S. Islam, A. Dixit and S. Ahmad, *Sci. Rep.*, 2022, **12**, 2176.
75 C.-H. Liao, M. A. Mahmud and A. W. Y. Ho-Baillie, *Nanoscale*, 2023, **15**, 4219–4235.
76 Y. Zheng, T. Niu, X. Ran, J. Qiu, B. Li, Y. Xia, Y. Chen and W. Huang, *J. Mater. Chem. A*, 2019, **7**, 13860–13872.
77 C. Lan, Z. Zhou, R. Wei and J. C. Ho, *Mater. Today Energy*, 2019, **11**, 61–82.
78 G. Wu, R. Liang, Z. Zhang, M. Ge, G. Xing and G. Sun, *Small*, 2021, **17**, 2103514.
79 S. Masi, A. F. Gualdron-Reyes and I. Mora-Sero, *ACS Energy Lett.*, 2020, **5**, 1974–1985.
80 X. Li, J. Hoffman, W. Ke, M. Chen, H. Tsai, W. Nie, A. D. Mohite, M. Kepenekian, C. Katan, J. Even, M. R. Wasielewski, C. C. Stoumpos and M. G. Kanatzidis, *J. Am. Chem. Soc.*, 2018, **140**, 12226–12238.
81 J. Cho, J. T. DuBose, A. N. T. Le and P. V. Kamat, *ACS Mater. Lett.*, 2020, **2**, 565–570.
82 D. H. Cao, C. C. Stoumpos, O. K. Fahra, J. T. Hupp and M. G. Kainatzidis, *J. Am. Chem. Soc.*, 2015, **137**, 7843–7850.
83 X. Gan, O. Wang, K. Liu, X. Du, L. Guo and H. Liu, *Sol. Energy Mater. Sol. Cells*, 2017, **162**, 93–102.
84 N. Pandech, T. Kongnok, N. Palakawong, S. Limpijumnong, W. R. L. Lambrecht and S. Jungthawan, *ACS Omega*, 2020, **5**, 25723–25732.
85 J. C. Blancon, H. Tsai, W. Nie, C. C. Stoumpos, L. Pedesseau, C. Katan, M. Kepenekian, C. M. Soe, K. Appavoo, M. Y. Sfeir, S. Tretiak, P. M. Ajayan, M. G. Kanatzidis, J. Even, J. J. Crochet and A. D. Mohite, *Science*, 2017, **355**, 1288–1292.
86 C. C. Stoumpos, D. H. Cao, D. J. Clark, J. Young, J. M. Rondinelli, J. I. Jang, J. T. Hupp and M. G. Kanatzidis, *Chem. Mater.*, 2016, **28**, 2852–2867.
87 W. Li, X. Feng, K. Guo, W. Pan, M. Li, L. Liu, J. Song, Y. He and H. Wei, *Adv. Mater.*, 2023, 2211808.
88 N. Parikh, M. M. Tavakoli, M. Pandey, A. Kalam, D. Prochowicz and P. Yadav, *Sustainable Energy Fuels*, 2021, **5**, 1255–1279.
89 W. Yang, X. Xiao, M. Li, J. Hu, X. Xiao, G. Tong, J. Chen and Y. He, *Chem. Mater.*, 2021, **33**, 4456–4464.
90 L. Li, X. Xu, L. Xiao, W. Jeng, J. Zhao, X. Kong and G. Zou, *ACS Appl. Energy Mater.*, 2021, **4**, 5935–5943.
91 J. Yan, W. Qiu, G. Wu, P. Heremans and H. Chen, *J. Mater. Chem. A*, 2018, **6**, 11063–11077.
92 T. Zhou, H. Ali, T. Liu, D. Lu, Z. Wan, X. Zhang, Y. Liu and Y. Chen, *Adv. Mater.*, 2019, **31**, 1901242–1901251.
93 K. T. Cho, Y. Zhang, S. Orlandi, M. Cavazzini, I. Zimmermann, A. Lesch, N. Tabet, G. Pozzi, G. Grancini and M. K. Nazeeruddin, *Nano Lett.*, 2018, **18**, 5467–5474.
94 M. Liu, M. B. Johnston and H. J. Snaith, *Nature*, 2013, **501**, 395–398.
95 S.-R. Bae, D. Y. Heo and S. Y. Kim, *Mater. Today Adv.*, 2022, **14**, 100232.
96 Y. Vaynzof, *Adv. Energy Mater.*, 2020, **10**, 2003073.
97 T. Abzieher, T. Feeney, F. Schackmar, Y. J. Donie, I. M. Hossain, J. A. Schwenzer, T. Hellmann, T. Mayer, M. Powalla and U. W. Paetzold, *Adv. Funct. Mater.*, 2021, **31**, 2104482.
98 P. Fan, D. Gu, G.-X. Liang, J.-T. Luo, J.-L. Chen, Z.-H. Zheng and D.-P. Zhang, *Sci. Rep.*, 2016, **6**, 29910.
99 O. Malinkwiewicz, A. Yella, Y. H. Lee, G. M. Espallargas, M. Graetzel, M. K. Nazeeruddin and H. J. Bolink, *Nat. Photonics*, 2014, **8**, 128–132.

100 J. Li, H. Wang, X. Y. Chin, H. A. Dewi, K. Vergeer, T. W. Goh, J. W. M. Lim, J. H. Lew, K. P. Loh, C. Soci, T. C. Sum, H. J. Bolink, N. Mathews, S. Mhaisalkar and A. Bruno, *Joule*, 2020, **4**, 1035–1053.
101 X. Liu, X. Tan, Z. Liu, B. Sun, J. Li, S. Xi, T. Shi and G. Liao, *J. Power Sources*, 2019, **443**, 227269.
102 C.-W. Chen, H.-W. Kang, S.-Y. Hsiao, P.-F. Yang, K.-M. Chiang and H.-W. Lin, *Adv. Mater.*, 2014, **26**, 6647–6652.
103 J. B. Patel, R. L. Milot, A. D. Wright, L. M. Herz and M. B. Johnston, *J. Phys. Chem. Lett.*, 2016, **7**, 96–102.
104 J. Feng, Y. Jiao, H. Wang, X. Zhu, Y. Sun, M. Du, Y. Du, Y. Cao, D. Yang and S. F. Liu, *Energy Environ. Sci.*, 2021, **14**, 3035–3043.
105 H. M. Christen and G. Eres, *J. Phys.: Condens. Matter*, 2008, **20**, 264005.
106 H. Schwarz and H. A. Tourtellotte, *J. Vac. Sci. Technol.*, 1969, **6**, 373–378.
107 U. Bansode, R. Naphade, O. Game, S. Agarkar and S. Ogale, *J. Phys. Chem. C*, 2015, **119**, 9177–9185.
108 S. Hoffmann-Urlaub, Y. Zhang, Z. Wang, B. Kressdorf and T. Meyer, *Appl. Phys. A: Mater. Sci. Process.*, 2020, **126**, 553.
109 Y. Liang, Y. Yao, X. Zhang, W.-L. Hsu, Y. Gong, J. Shin, E. D. Wachsman, M. Dagenais and I. Takeuchi, *AIP Adv.*, 2016, **6**, 015001.
110 P. Luo, S. Zhou, W. Xia, J. Cheng, C. Xu and Y. Lu, *Adv. Mater. Interfaces*, 2017, **4**, 1600970.
111 X. Chen, Y. Myung, A. Thind, Z. Gao, B. Yin, M. Shen, S. B. Cho, P. Cheng, B. Sadtler, R. Mishra and P. Banerjee, *J. Mater. Chem. A*, 2017, **5**, 24728–24739.
112 P. Luo, Z. Liu, W. Xia, C. Yuan, J. Cheng and Y. Lu, *ACS Appl. Mater. Interfaces*, 2015, **7**, 2708–2714.
113 M. M. Tavakoli, L. Gu, Y. Gao, C. Reckmeier, J. He, A. L. Rogach, Y. Yao and Z. Fan, *Sci. Rep.*, 2015, **5**, 14083.
114 M. Aaamir, M. Sher, M. D. Khan, M. A. Malik, J. Akhtar and N. Revaprasadu, *Mater. Lett.*, 2017, **190**, 244–247.
115 D. S. Bhachu, D. O. Scanlon, E. J. Saban, H. Bronstein, I. P. Parklin, C. J. Carmalt and R. G. Palgrave, *J. Mater. Chem. A*, 2015, **3**, 9071–9073.
116 X. Liu, L. Cao, Z. Guo, Y. Li, W. Gao and L. Zhou, *Materials*, 2019, **12**, 3304.
117 S. R. Ratnasingham, L. Mohan, M. Daboczi, T. Degousee, R. Bibions, O. Fenwick, J.-S. Kim, M. A. McLachlan and J. Briscoe, *Mater. Adv.*, 2021, **2**, 1606–1612.
118 M. M. Tavakoli, S. M. Zakeeruddin, M. Grätzel and Z. Fan, *Adv. Mater.*, 2018, **30**, 1705998.
119 S. Wang, L. K. Ono, M. R. Leyden, Y. Kato, S. R. Raga, M. V. Lee and Y. Qi, *J. Mater. Chem. A*, 2015, **3**, 14631–14641.
120 M. R. Leyden, L. K. Ono, S. R. Raga, Y. Kato, S. Wang and Y. Qi, *J. Mater. Chem. A*, 2014, **2**, 18742–18745.
121 Y. Peng, G. Jing and T. Cui, *Mater. Res. Soc. Symp. Proc.*, 2015, **1771**, 187–192.
122 S. Ullah, L. Liu, S.-E. Yang, P. Liu, H. Guo and Y. Chen, *J. Phys. D: Appl. Phys.*, 2022, **55**, 064001.
123 P.-S. Shen, J.-S. Chen, Y.-H. Chiang, M.-H. Li, T.-F. Guo and P. Chen, *Adv. Mater. Interfaces*, 2016, **3**, 1500849.
124 L. Qiu, S. He, Y. Jiang, D.-Y. Son, L. K. Ono, Z. Liu, T. Kim, T. Bouloumis, S. Kazaoui and Y. Qi, *J. Mater. Chem. A*, 2019, **7**, 6920–6929.
125 H. S. Kim, C. R. Lee, J. H. Im, K.-B. Lee, T. Moehl, A. Marcioro, S.-J. Moon, R. Humphry-Baker, J.-H. Yum, J. E. Moser, M. Grätzel and N.-G. Park, *Sci. Rep.*, 2012, **2**, 591.
126 J. Burschka, N. Pellet, S.-J. Moon, R. Humphry-Baker, P. Gao, M. K. Nazeeruddin and M. Grätzel, *Nature*, 2013, **499**, 316–319.
127 K. Liang, D. B. Mitzi and M. T. Prikas, *Chem. Mater.*, 1998, **10**, 403–411.
128 K. L. Gardner, J. G. Tait, T. Merckx, W. Qiu, U. W. Paetzold, L. Kootstra, M. Jaysankar, J. Gehlhaar, D. Cheyns, P. Heremans and J. Poortmans, *Adv. Energy Mater.*, 2016, **6**, 1600386.
129 L. Zheng, D. Zhang, Y. Ma, Z. Lu, Z. Chen, S. Wang, L. Xiao and Q. Gong, *Dalton Trans.*, 2015, **44**, 10582.
130 P. J. Holliman, E. W. Jones, R. J. Hobbs, A. Connell, L. Furnell, R. Anthony and C. P. Kershaw, *Mater. Lett.*, 2019, **2**, 100011.
131 W. Nie, H. Tsai, R. Asadpour, J.-C. Blancon, A. J. Neukirch, G. Gupta, J. J. Crochet, M. Chowalla, S. Tretiak, M. A. Alam, H.-L. Wang and A. D. Mohite, *Science*, 2015, **347**, 522–525.
132 Q. Wang, W. Zhang, Z. Zhang, S. Liu, J. Wu, Y. Guan, A. Mei, Y. Rong, Y. Hu and H. Han, *Adv. Energy Mater.*, 2020, **10**, 1903092.
133 C. Li, Q. Guo, W. Qiao, Q. Chen, S. Ma, X. Pan, F. Wang, J. Yao, C. Zhang, M. Xiao, S. Dai and Z. Tan, *Org. Electron.*, 2016, **33**, 194–200.
134 M. Xiao, F. Huang, W. Huang, Y. Dkhissi, Y. Zhu, J. Etheridge, A. Gray-Weale, U. Bach, Y.-B. Cheng and L. Spiccia, *Angew. Chem., Int. Ed.*, 2014, **53**, 1–7.
135 J.-H. Im, H.-S. Kim and N.-G. Park, *APL Mater.*, 2014, **2**, 081510.
136 Z. Xiao, C. Bi, Y. Shao, Q. Dong, Q. Wang, Y. Yuan, C. Wang, Y. Gao and J. Huang, *Energy Environ. Sci.*, 2014, **7**, 2619–2623.
137 Z. Yang, S. Zhang, L. Li and W. Chen, *J. Materiomics*, 2017, **3**, 231–244.
138 A. Kumar, M. Shkir, H. H. Somaily, K. L. Singh, B. C. Choudhary and S. K. Tripathi, *Phys. B*, 2022, **630**, 413678.
139 C. Zuo and L. Ding, *Angew. Chem.*, 2021, **60**, 11242–11246.
140 Z. Lai, Y. Meng, F. Wang, X. Bu, W. Wang, P. Xie, W. Wang, C. Liu, S. Yip and J. C. Ho, *Nano Res.*, 2022, **15**, 3621–3627.
141 A. Mei, X. Li, L. Liu, Z. Ku, T. Liu, Y. Rong, M. Xu, M. Hu, J. Chen, Y. Yang, M. Grätzel and H. Han, *Science*, 2014, **345**, 295–298.
142 X. Li, M. Tschumi, H. Han, S. S. Babkair, R. A. Alzubaydi, A. A. Ansari, S. S. Habib, M. K. Nazeeruddin, S. M. Zakeeruddin and M. Grätzel, *Energy Technol.*, 2015, **3**, 551–555.
143 C. Zuo, A. D. Scully and M. Gao, *ACS Appl. Mater. Interfaces*, 2021, **13**, 56217–56225.
144 S. D. Stranks, P. K. Nayak, W. Zhang, T. Stergiopoulos and H. J. Snaith, *Angew. Chem., Int. Ed.*, 2015, **54**, 3240–3248.

145 T.-B. Song, Q. Chen, H. Zhou, C. Jiang, H.-H. Wang, Y. M. Yang, Y. Liu, J. You and Y. Yang, *J. Mater. Chem. A*, 2015, **3**, 9032–9050.
146 H. Zhou, Q. Chen and Y. Yang, *MRS Bull.*, 2015, **40**, 667–673.
147 Q. Chen, H. Zhou, Z. Hong, S. Luo, H.-S. Duan, H.-H. Wang, Y. Liu, G. Li and Y. Yang, *J. Am. Chem. Soc.*, 2014, **136**, 622–625.
148 R. Sedighi, F. Tajabadi, S. Shahbazi, S. Gholipour and N. Taghavinia, *ChemPhysChem*, 2016, **17**, 2382–2388.
149 W.-W. Zuo, Y.-G. Yang, W.-F. Fu, M. Li, M. M. Byranvand, D. D. Girolamo, J. Pascual, M.-Q. Li, L.-N. Li, A. Abate, M. Saliba and Z.-K. Wang, *ACS Mater. Lett.*, 2022, **4**, 448–456.
150 J. Chen, J. Xu, L. Xiao, B. Zhang, S. Dai and J. Yao, *ACS Appl. Mater. Interfaces*, 2017, **9**, 2449–2458.
151 Y.-A. Chen, H.-W. Shiu, Y.-J. Hsu, L. E. Mundt, W.-T. Hung, T. Ohigashi, M.-H. Li and P. Chen, *J. Phys. Chem. C*, 2021, **125**, 26601–26612.
152 M. U. Ali, W. Cai, J. Cai, J. Miao, S. Zhang, J. Chen, L. Xiao, H. Meng, C. Yan and G. Wei, *Adv. Opt. Mater.*, 2022, **10**, 2100671.
153 M. S. Shadabroo, H. Abdizadeh and M. R. Golobostanfard, *ACS Appl. Energy Mater.*, 2021, **4**, 6797–6805.
154 M. Prakasam, O. Viraphong, O. Cambon and A. Largeteau, Hydrothermal Crystal Growth and Applications, in *Advances in Solid Oxide Fuel Cells and Electronic Ceramics*, ed. N. P. Bansal, M. Kusnezoff and K. Shimamura, John Wiley & Sons, Inc., 2015, ch. 15, pp. 151–156.
155 R. C. M. Mambote, M. A. Reuter, P. Krijgsman and R. D. Schuiling, *Miner. Eng.*, 2000, **13**, 803–822.
156 S.-H. Feng and G.-H. Li, Hydrothermal and Solvothermal Syntheses, in *Modern Inorganic Synthetic Chemistry*, ed. R. Xu and Y. Xu, Elsevier B.V., 2017, ch. 4, pp. 73–104.
157 K. Byrappa and M. Yoshimura, 10-Hydrothermal technology for nanotechnology – A technology for processing of advanced materials, *Handbook of hydrothermal technology*, William Andrew Publishing, 2nd edn, 2013, pp. 615–762.
158 Y. X. Gan, A. H. Jayatissa, Z. Yu, X. Chen and M. Li, *J. Nanomater.*, 2020, **2020**, 8917013.
159 J. C. Rendón-Angeles, Z. Matamoros-Veloza, K. L. Montoya-Cisneros, J. L. Cuevas and K. Yanagisawa, Synthesis of perovskite oxides by hydrothermal processing – From thermodynamic modelling to practical processing approaches, perovskite materials – synthesis, in *Characterisation, Properties, and Applications*, ed. L. Pan and G. Zhu, IntechOpen, 2016.
160 H.-R. Xia, W.-T. Sun and L.-M. Peng, *Chem. Commun.*, 2015, **51**, 13787–13790.
161 K. Mahmood, A. Khalid and M. T. Mehran, *Nanoscale Adv.*, 2019, **1**, 64–70.
162 G. Murugadoss, R. Thangamuthu, S. M. S. Kumar, N. Anandhan, M. R. Kumar and A. Rathishkumar, *J. Alloys Compd.*, 2019, **787**, 17–26.
163 M. Jansen, *Angew. Chem., Int. Ed.*, 2002, **41**, 3746–3766.
164 R. I. Walton, *Chem. Soc. Rev.*, 2002, **31**, 230–238.
165 Y. Sun and H.-C. Zhou, *Sci. Technol. Adv. Mater.*, 2015, **16**, 054202.
166 R. A. Laudise, *Chem. Eng. News*, 1987, **65**, 30–43.
167 C. S. Cundy and P. A. Cox, *Chem. Rev.*, 2003, **103**, 663–702.
168 D. R. Modeshia and R. I. Walton, *Chem. Soc. Rev.*, 2010, **39**, 4303–4325.
169 C. N. R. Rao and J. Gopalakrishnan, *Acc. Chem. Res.*, 1987, **20**, 228–235.
170 C. N. R. Rao, *J. Mater. Chem. A*, 1999, **9**, 1–14.
171 B. Zhang, F. Guo, L. Yang, X. Jia, B. Liu, Z. Xie, D. Chen, H. Lu, R. Zhang and Y. Zheng, *J. Cryst. Growth*, 2017, **459**, 167–172.
172 F. Guo, B. Zhang, J. Wang, H. Ba, R. Guo, Y. Huang and P. Ren, *Opt. Mater. Express*, 2017, **7**, 4156–4162.
173 Y. Chen, S. Yang, X. Chen, Y. C. Zheng, Y. Hou, Y. H. Li, H. D. Zeng and H. G. Yang, *J. Mater. Chem. A*, 2015, **3**, 15854–15857.
174 W. Zhai, J. Lin, Q. Li, K. Zheng, Y. Huang, Y. Yao, X. He, L. Li, C. Yu, C. Liu, Y. Fang, Z. Liu and C. Tang, *Chem. Mater.*, 2018, **30**, 3714–3721.
175 D. Chen, G. Fang, X. Chen, L. Lei, J. Zhong, Q. Mao, S. Zhou and J. Li, *J. Mater. Chem. C*, 2018, **6**, 8990–8998.
176 C. Liu, J. Lin, W. Zhai, Z. Wen, X. He, M. Yu, Y. Huang, Z. Guo, C. Yu and C. Tang, *RSC Adv.*, 2019, **9**, 39315–39322.
177 W. Zhai, J. Lin, C. Li, S. Hu, Y. Huang, C. Yu, Z. Wen, Z. Liu, Y. Fang and C. Tang, *Nanoscale*, 2018, **10**, 21451–21458.
178 Z. Peng, D. Yang, B. Yin, X. Guo, S. Li, Q. Zhan, X. Xiao, X. Liu, Z. Xia, Z. Yang, J. Qiu and G. Dong, *Sci, China Mater.*, 2021, **64**, 2261–2271.
179 M. Yu, D. Zhang, Y. Xu, J. Lin, C. Yu, Y. Fang, Z. Liu, Z. Guo, C. Tang and Y. Huang, *J. Colloid Interface Sci.*, 2022, **608**, 2367–2376.
180 N. N. Gharat and V. K. Rathod, Ultrasound-assisted organic synthesis, *Green Sustainable Process for Chemical and Environmental Engineering and Science Sonochemical Organic Synthesis*, Elsevier, 2020, ch. 1, 1–41.
181 J. J. Hinman and K. S. Suslick, *Top. Curr. Chem.*, 2017, **375**, 12.
182 V. R. Raja, D. R. Rosaline, A. Suganthia and M. Rajarajan, *Ultrason. Sonochem.*, 2018, **44**, 73–85.
183 Y. Zhang, M. Park, H. Y. Kim, B. Ding and S.-J. Park, *Sci. Rep.*, 2017, **7**, 45086.
184 J. C. Colmenares, E. Kuna and P. Lisowski, *Top. Curr. Chem.*, 2016, **374**, 59.
185 M. Ashokkumar, J. L. S. Kentish and F. Grieser, *Ultrason. Sonochem.*, 2007, **14**, 470–475.
186 D. M. Jang, D. H. Kim, K. Park, J. Park, J. W. Lee and J. K. Song, *J. Mater. Chem. C*, 2016, **4**, 10625–10629.
187 W. Peng, L. Wang, B. Murali, K.-T. Ho, A. Bera, N. Cho, C.-F. Kang, V. M. Burlakov, J. Pan, L. Sinatra, C. Ma, W. Xu, D. Shi, E. Alarousu, A. Goriely, J.-H. He, O. F. Mohammed, T. Wu and O. M. Bakr, *Adv. Mater.*, 2016, **28**, 3383–3390.
188 L.-C. Chen, Z.-L. Tseng, S. Y. Chen and S. Yang, *Ceram. Int.*, 2017, **43**, 16032–16035.

189 K. Umemoto, H. Ebe, R. Sato, J. Enomoto, N. Oshita, T. Kimura, T. Inose, T. Nakamura, T. Chiba, S. Asakura, H. Uji-I and A. Masuhara, *ACS Sustainable Chem. Eng.*, 2020, **8**, 16469–16476.
190 J. Enomoto, R. Sato, M. Yokoyama, T. Kimura, N. Oshita, K. Umemoto, S. Asakura and A. Masuhara, *RSC Adv.*, 2022, **12**, 5571–5576.
191 A. Kokel, C. Schäfer and B. Torok, Microwave-Assisted Reactions in Green Chemistry, in *Green Chemistry and Chemical Engineering. Encyclopedia of Sustainability Science and Technology Series*, ed. B. Han and T. Wu, Springer, New York, 2019, pp. 537–612.
192 M. B. Gawande, S. N. Shelke, R. Zboril and R. S. Varma, *Acc. Chem. Res.*, 2014, **47**, 1338–1348.
193 A. Kumar, Y. Kuang, Z. Liang and X. Sun, Microwave chemistry, recent advancements, and eco-friendly microwave-assisted synthesis of nanoarchitectures and their applications: a review, *Mater. Today Nano*, 2020, **11**, 100076.
194 M. Henary, C. Kananda, L. Rotolo, B. Savino, E. A. Owens and G. Cravotto, *RSC Adv.*, 2020, **10**, 14170–14197.
195 R. Gedye, F. Smith, K. Westaway, H. Ali and L. Baldisera, *Tetrahedron Lett.*, 1986, **27**, 279e282.
196 R. J. Giguere, T. L. Bray, S. M. Duncan and G. J. Majetich, *Tetrahedron Lett.*, 1986, **27**, 4945e4948.
197 A. Kojima, K. Teshima, Y. Shirai and T. Miyasaka, *J. Am. Chem. Soc.*, 2009, **131**, 6050–6051.
198 Q. Cao, S. Yang, Q. Gao, L. Lei, Y. Yu, J. Shao and Y. Liu, *ACS Appl. Mater. Interfaces*, 2016, **8**, 7854–7861.
199 B. Yang, O. Dyck, J. Poplawsky, J. Keum, A. Puretzky, S. Das, I. Ivanov, C. Rouleau, G. Duscher, D. Geohegan and K. Xiao, *J. Am. Chem. Soc.*, 2015, **137**, 9210–9213.
200 M. Kim, G.-H. Kim, K. S. Oh, Y. Jo, H. Yoon, K.-H. Kim, H. Lee, J. Y. Kim and D. S. Kim, *ACS Nano*, 2017, **11**, 6057–6064.
201 L. Huang, Z. Hu, J. Xu, K. Zhang, J. Zhang and Y. Zhu, *Sol. Energy Mater. Sol. Cells*, 2015, **141**, 377–382.
202 X. Chen, Z. Wang, R.-J. Wu, H.-L. Cheng and H.-C. Chui, *Photonics*, 2021, **8**, 30.
203 C.-H. Lin, Z. Lyu, Y. Zhuo, C. Zhao, J. Yang, C. Liu, J. Kim, T. He, L. Hu, F. Li, Y. Shen, K. Liu, W. Yu and T. Wu, *Adv. Opt. Mater.*, 2020, **8**, 2001740.
204 I. Bilecka and M. Niederberger, *Nanoscale*, 2010, **2**, 1358–1374.
205 H. Pan, X. Li, X. Zhang, J. Liu, X. Chen, H. Zhang, A. Huang and Z. Xiao, *Langmuir*, 2020, **36**, 13663–13669.
206 H. Zhang, J. Mao, H. He, D. Zhang, H. L. Zhu, F. Xie, K. S. Wong, M. Grätzel and W. C. Choy, *Adv. Energy Mater.*, 2015, **5**, 1501354.
207 Z. Yang, B. Cai, B. Zhou, T. Yao, W. Yu, S. F. Liu, W. H. Zhang and C. Li, *Nano Energy*, 2015, **15**, 670–678.
208 B. A. Rosales, L. Men, S. D. Cady, M. P. Hanrahan, A. J. Rossini and J. Vela, *Chem. Mater.*, 2016, **28**, 6848–6859.
209 C. C. Hsu, S. M. Yu, K. M. Lee, C. J. Lin, H. C. Cheng and F. R. Chen, *Sol. Energy Mater. Sol. Cells*, 2021, **227**, 111014.
210 L. Chen, F. Tang, Y. Wang, S. Gao, W. Cao, J. Cai and L. Chen, *Nano Res.*, 2015, **8**, 263–270.
211 H. Zheng, Y. Liu and J. Sun, *Appl. Surface Sci.*, 2017, **405**, 412–419.
212 H. Huang, A. S. Susha, S. V. Kershaw, T. F. Hung and A. L. Rogach, *Adv. Sci.*, 2015, **2**, 1500194.
213 J. Sun, F. Li, J. Yuan and W. Ma, *Small Methods*, 2021, **5**, 2100046.
214 S. Ghosh, S. Mishra and T. Singh, *Adv. Mater. Interfaces*, 2020, **7**, 2000950.
215 W. Xu, Y. Gao, W. Ming, F. He, J. Li, X.-H. Zhu, F. Kang, J. Li and G. Wei, *Adv. Mater.*, 2020, **32**, 2003965.
216 D. S. Ahmed, B. K. Mohammed and M. K. A. Mohammed, *J. Mater. Sci.*, 2021, **56**, 15205–15214.
217 J. Li, X. Hua, F. Gao, X. Ren, C. Zhang, Y. Han, Y. Li, B. Shi and S. F. Liu, *J. Energy Chem.*, 2022, **66**, 1–8.
218 S. Paek, P. Schouwink, E. N. Athanasopoulou, K. T. Cho, G. Grancini, Y. Lee, Y. Zhang, F. Stellacci, M. K. Nazeeruddin and P. Gao, *Chem. Mater.*, 2017, **29**, 3490–3498.
219 L. Chouhan, S. Ghimire, C. Subrahmanyam, T. Miyasaka and V. Biju, *Chem. Soc. Rev.*, 2020, **49**, 2869–2885.
220 S. Ghimire, L. Chouhan, Y. Takano, K. Takahashi, T. Nakamura, K. I. Yuyama and V. Biju, *ACS Energy Lett.*, 2018, **4**, 133–141.
221 L. C. Schmidt, A. Pertegás, S. González-Carrero, O. Malinkiewicz, S. Agouram, G. Minguez Espallargas, H. J. Bolink, R. E. Galian and J. Pérez-Prieto, *J. Am. Chem. Soc.*, 2014, **136**, 850–853.
222 S. Sun, D. Yuan, Y. Xu, A. Wang and Z. Deng, *ACS Nano*, 2016, **10**, 3648–3657.
223 L. Potesescu, S. Yakunin, M. I. Bodnarchuk, F. Krieg, R. Caputo, C. H. Hendon, R. X. Yang, A. Walsh and M. V. Kovalenko, *Nano Lett.*, 2015, **15**, 3692–3696.
224 L. Potesescu, S. Yakunin, M. I. Bodnarchuk, F. Bertolotti, N. Masciocchi, A. Guagliardi and M. V. Kovalenko, *J. Am. Chem. Soc.*, 2016, **138**, 14202–14205.
225 F. Zhang, H. Zhong, C. Chen, X. G. Hu, H. Huang, J. Han, B. Zou and Y. Dong, *ACS Nano*, 2015, **9**, 4533–4542.
226 A. J. Prochazkova, M. C. Scharber, C. Yumusak, J. Másilko, O. Brüggemann, M. Weiter, N. S. Sariciftci, J. Krajcovic, Y. Salinas and A. Kovalenko, *Sci. Rep.*, 2020, **10**, 1–12.
227 J. Zhang, Y. Yang, H. Deng, U. Farooq, X. Yang, J. Khan, J. Tang and H. Song, *ACS Nano*, 2017, **11**, 9294–9302.
228 H. Chen, Z. Wei, X. Zheng and S. Yang, *Nano Energy*, 2015, **15**, 216–226.
229 J. A. Koza, J. C. Hill, A. C. Demster and J. A. Switzer, *Chem. Mater.*, 2015, **28**, 339–405.
230 G. Popov, M. Mattinen, M. L. Kemell, M. Ritala and M. Leskelä, *ACS Omega*, 2016, **1**, 1296–1306.
231 J. Yadav, Q. Liang and S. Pan, *J. Phys. Chem. C*, 2020, **124**, 10659–10668.
232 P. Luo, S. Zhou, Z. Liu, W. Xia, L. Sun, J. Cheng, C. Xu and Y. Lu, *Chem. Commun.*, 2016, **52**, 11203–11206.
233 D. Liu, K. Liu, Y. Liu, J. Bai, M. Dai, F. Liu and G. Lu, *Sol. Energy*, 2020, **212**, 275–281.

234 X. Wang, S. Abbasi, D. Zhang, J. Wang, Y. Wang, Z. Cheng, H. Liu and W. Shen, *ACS Appl. Mater. Interfaces*, 2020, **12**, 50455–50463.
235 A. D. Jodlowski, A. Yépez, R. Luque, L. Camacho and G. de Miguel, Benign-by-design solventless mechanochemical of three-,two-, and one-dimensional hybrid perovskites, *Angew. Chem., Int. Ed.*, 2016, **55**, 14972.
236 P. Pal, S. Saha, A. Banik, A. Sarkar and K. Biswas, *Chem. – Eur. J.*, 2018, **24**, 1811.
237 N. Leupold, K. Schötz, S. Cacovich, I. Bauer, M. Schultz, M. Daubinger, L. Kaiser, A. Rebai, J. Rousset, A. Köhler, P. Schulz, R. Moos and F. Panzer, *ACS Appl. Mater. Interfaces*, 2019, **11**, 30259.
238 A. Jana, M. Mittal, A. Singla and S. Sapra, *Chem. Commun.*, 2017, **53**, 3046.
239 D. J. Kubicki, D. Prochowicz, A. Hofstetter, P. Péchy, S. M. Zakeeruddin, M. Grätzel and L. Emsley, *J. Am. Chem. Soc.*, 2017, **139**, 10055.
240 A. M. Askar, A. Karmakar, G. M. Bernard, M. Ha, V. V. Terskikh, B. D. Wiltshire, S. Patel, J. Fleet, K. Shankar and V. K. Michaelis, *J. Phys. Chem. Lett.*, 2018, **9**, 2671.
241 L. Protesescu, S. Yakunin, O. Nazarenko, D. N. Dirin and M. V. Kovalenko, *ACS Appl. Nano Mater.*, 2018, **1**, 1300.
242 A. Karmakar, M. S. Dodd, X. Zhang, M. S. Oakley, M. Klobukowski and V. K. Michaelis, *Chem. Commun.*, 2019, **55**, 5079.
243 F. Palazon, Y. E. L. Ajjouri, P. Sebastia-Luna, S. Lauciello, L. Manna and H. J. Bolink, *J. Mater. Chem. C*, 2019, **7**, 11406.
244 C. A. López, C. Abia, M. C. Alvarez-Galván, B.-K. Hong, M. V. Martínez-Huerta, F. Serrano-Sánchez, F. Carrascoso, A. Castellanos-Gómez, M. T. Fernández-Díaz and J. A. Alonso, *ACS Omega*, 2020, **5**, 5931.
245 A. Goyal, E. Andrioti, Y. Tang, Q. Zhao, K. Zheng, K. D. Newell and P. Schall, *J. Phys. Mater.*, 2022, **5**, 024005.
246 Y. E. L. Ajjouri, F. Locardi, M. C. Gélvez-Rueda, M. Prato, M. Sessolo, M. Ferretti, F. C. Grozema, F. Palazon and H. J. Bolink, *Energy Technol.*, 2020, **8**, 1900788.
247 K. Kundu, P. Dutta, P. Acharyya and K. Biswas, *Mater. Res. Bull.*, 2021, **140**, 111339.
248 K. Kundu, P. Dutta, P. Acharyya and K. Biswas, *J. Phys. Chem. C*, 2021, **125**, 4720–4729.
249 P. Sebastian-Luna, J. Calbo, N. Albiach-Sebastian, M. Sessolo, F. Palazon, E. Orti and H. J. Bolink, *Chem. Mater.*, 2021, **33**, 8028–8035.
250 D. Prochowicz, P. Yadav, M. Saliba, D. J. Kubicki, M. M. Tavakoli, S. M. Zakeeruddin, J. Lewiński, L. Emsley and M. Grätzel, *Nano Energy*, 2018, **49**, 523.
251 B. Dou, L. M. Wheeler, J. A. Christians, D. T. Moore, S. P. Harvey, J. J. Berry, F. S. Barnes, S. E. Shaheen and M. F. A. M. van Hest, *ACS Energy Lett.*, 2018, **3**, 979.
252 S. Tang, X. Xiao, J. Hu, B. Gao, H. Chen, Z. Peng, J. Wen, M. Era and D. Zou, *ChemPlusChem*, 2020, **85**, 240.
253 S. Liu, J. K. Wu, C. C. Fan, G. B. Xue, H. Z. Chen, H. L. Xin and H. Y. Li, *Sci. Bull.*, 2015, **60**, 1122.
254 H. Li, B. C. K. Tee, J. J. Cha, Y. Cui, J. W. Chung, S. Y. Lee and Z. Bao, *J. Am. Chem. Soc.*, 2012, **134**, 2760.
255 T. Ye, W. Fu, J. Wu, Z. Yu, X. Jin, H. Chen and H. Li, *J. Mater. Chem. A*, 2016, **4**, 1214.
256 S. A. Gandhi, *Crystal Growth: Concepts, Mechanisms and Applications*, Nova Science Publishers, Inc., 2017, pp. 1–34.
257 W. Q. Liao, Y. Zhang, C. L. Hu, J. G. Mao, H. Y. Ye, P. F. Li, S. D. Huang and R. G. Xiong, *Nat. Commun.*, 2015, **6**, 7338.
258 P. W. Bridgman, *Proc. Am. Acad. Arts Sci.*, 1925, **60**, 305.
259 L. Braescu, *J. Colloid Interface Sci.*, 2008, **319**, 309.
260 I. Chung, B. Lee, J. He, R. P. H. Chang and M. G. Kanatzidis, *Nature*, 2012, **485**, 486.
261 M. Rodová, J. Brožek, K. Knížek and K. Nitsch, *J. Therm. Anal. Calorim.*, 2003, **71**, 667.
262 C. C. Stoumpos, C. D. Malliakas, J. A. Peters, Z. Liu, M. Sebastian, J. Im, T. C. Chasapis, A. C. Wibowo, D. Y. Chung, A. J. Freeman, B. W. Wessels and M. G. Kanatzidis, *Cryst. Growth Des.*, 2013, **13**, 2722.
263 Y. He, L. Matei, H. J. Jung, K. M. McCall, M. Chen, C. C. Stoumpos, Z. Liu, J. A. Peters, D. Y. Chung, B. W. Wessels, M. R. Wasielewski, V. P. Dravid, A. Burger and M. G. Kanatzidis, *Nat. Commun.*, 2018, **9**, 1609.
264 P. Zhang, G. Zhang, L. Liu, D. Ju, L. Zhang, K. Cheng and X. Tao, *J. Phys. Chem. Lett.*, 2018, **9**, 5040.
265 J. Peng, C. Q. Xia, Y. Xu, R. Li, L. Cui, J. K. Clegg, L. M. Herz, M. B. Johnston and Q. Lin, *Nat. Commun.*, 2021, **12**, 1531.
266 Y. Liu, Z. Yang, D. Cui, X. Ren, J. Sun, X. Liu, J. Zhang, Q. Wei, H. Fan, F. Yu and X. Zhang, *Adv. Mater.*, 2015, **27**, 5176–5183.
267 Y. Cho, H. R. Jung, Y. S. Kim, Y. Kim, J. Park, S. Yoon, Y. Lee, M. Cheon, S.-Y. Jeong and W. Jo, *Nanoscale*, 2021, **13**, 8275–8282.
268 D. N. Dirin, I. Cherniukh, S. Yakunin, Y. Shynkarenko and M. V. Kovalenko, *Chem. Mater.*, 2016, **28**, 8470–8474.
269 K. Wang, L. Jing, Q. Yao, J. Zhang, X. Cheng, Y. Yuan, C. Shang, J. Ding, T. Zhou, H. Sun, W. Zhang and H. Li, *J. Phys. Chem. Lett.*, 2021, **12**, 1904–1910.
270 A. Y. Alsalloum, B. Turedi, K. Almasabi, X. Zheng, R. Naphade, S. D. Stranks, O. F. Mohammed and O. M. Bakr, *Energy Environ. Sci.*, 2021, **14**, 2263–2268.
271 Z. Yuan, J. Zhou, Y. Zhang, X. Ma, J. Wang, J. Dong, F. Lu, D. Han, B. Kuang and N. Wang, *J. Phys.: Condens. Mater.*, 2022, **34**, 144009.
272 T. Baikie, Y. Fang, J. M. Kadro, M. Schreyer, F. Wei, S. G. Mhaisalkar, M. Graetzel and T. J. White, *J. Mater. Chem. A*, 2013, **1**, 5628–5641.
273 G. Walters, B. R. Sutherland, S. Hoogland, D. Shi, R. Comin, D. P. Sellan, O. M. Bakr and E. H. Sargent, *ACS Nano*, 2015, **9**, 9340–9346.
274 Q. Han, S.-H. Bae, P. Sun, Y.-T. Hsieh, Y. M. Yang, Y. S. Rim, H. Zhao, Q. Chen, W. Shi, G. Li and Y. Yang, *Adv. Mater.*, 2016, **28**, 2253–2258.
275 Y. Rakita, N. Kedem, S. Gupta, A. Sadhanala, V. Kalchenko, M. L. Böhm, M. Kulbak, R. H. Friend, D. Cahen and G. Hodes, *Cryst. Growth Des.*, 2016, **16**, 5717–5725.

276 M. I. Saidaminov, M. A. Haque, J. Almutlaq, S. Sarmah, X.-H. Miao, R. Begum, A. A. Zhumekenov, I. Dursun, N. Cho, B. Murali, O. F. Mohammed, T. Wu and O. M. Bakr, *Adv. Opt. Mater.*, 2017, **5**, 1600704.
277 Y. Hua, F. Cui, P. Zhang, Q. Zhang and X. Tao, *Anorg. Allg. Chem.*, 2022, e202200025.
278 X. Mo, T. Li, F. Huang, Z. Li, Y. Zhou, T. Lin, Y. Ouyang, X. Tao and C. Pan, *Nano Energy*, 2021, **81**, 105570.
279 D. Shi, V. Adinolfi, R. Comin, M. Yuan, E. Alarousu, A. Buin, Y. Chen, S. Hoogland, A. Rothenberger, K. Katsiev and Y. Losovyi, *Science*, 2015, **347**, 519–522.
280 Y. Yang, Y. Yan, M. Yang, S. Choi, K. Zhu, J. M. Luther and M. C. Beard, *Nat. Commun.*, 2015, **6**, 7961.
281 H. Wei, Y. Fang, P. Mulligan, W. Chuirazzi, H. H. Fang, C. Wang, B. R. Ecker, Y. Gao, M. A. Loi, L. Cao and J. Huang, *Nat. Photonics*, 2016, **10**, 333–339.
282 H. Zhou, Z. Nie, J. Yin, Y. Sun, H. Zhuo, D. Wang, D. Li, J. Dou, X. Zhang and T. Ma, *RSC Adv.*, 2015, **5**, 85344–85349.
283 C. Zuo and L. Ding, *Angew. Chem.*, 2017, **56**, 6528–6532.
284 F. Liu, F. Wang, K. R. Hansen and X.-Y. Zhu, *J. Phys. Chem. C*, 2019, **123**, 14865–14870.
285 C.-H. Liao, C.-H. Chen, J. Bing, C. Bailey, Y.-T. Lin, T. M. Pandit, L. Granados, J. Zheng, S. Tang, B.-H. Lin, H.-W. Yen, D. R. McCamey, B. J. Kennedy, C.-C. Chueh and A. W. Y. Ho-Baillie, *Adv. Mater.*, 2022, **34**, 2104782.
286 D. B. Mitzi, *J. Solid State Chem.*, 1999, **145**, 694–704.
287 Y. Dang, Y. Zhou, X. Liu, D. Ju, S. Xia, H. Xia and X. Tao, *Angew. Chem.*, 2016, **55**, 3447–3450.
288 Y. Dang, Y. Liu, Y. Sun, D. Yuan, X. Liu, W. Lu, G. Liu, H. Xia and X. Tao, *CrystEngComm*, 2015, **17**, 665–670.
289 Z. Lia, Q. Yan, Q. Lv, Y. Wang, L. Liu, L. Zhang, S. Pan, Q. Li, L. Wang and J.-L. Sun, *Sci. Rep.*, 2015, **5**, 16563.
290 H. Amano, N. Sawaki, I. Akasaki and Y. Toyoda, *Appl. Phys. Lett.*, 1986, **48**, 353.
291 T. Detchprohm, K. Hiramatsu, H. Amano and I. Akasaki, *Appl. Phys. Lett.*, 1992, **61**, 2688.
292 Y. Wang, X. Sun, Z. Chen, Y.-Y. Sun, S. Zhang, T.-M. Lu, E. Wertz and J. Shi, *Adv. Mater.*, 2017, **29**, 1702643.
293 X. Cheng, S. Yang, B. Cao, X. Tao and Z. Chen, *Adv. Funct. Mater.*, 2020, **30**, 1905021.
294 Y. Liu, Y. Zhang, Z. Yang, D. Yang, X. Ren, L. Pang and S. F. Liu, *Adv. Mater.*, 2016, **28**, 9204–9209.
295 Y. X. Chen, Q. Q. Ge, Y. Shi, J. Liu, D. J. Xue, J. Y. Ma, J. Ding, H. J. Yan, J. S. Hu and L. J. Wan, *J. Am. Chem. Soc.*, 2016, **138**, 16196.
296 H. S. Rao, W. G. Li, B. X. Chen, D. Bin Kuang and C. Y. Su, *Adv. Mater.*, 2017, **29**, 1602639.
297 H. S. Rao, B. X. Chen, X. D. Wang, D.-B. Kuang and C. Y. Su, *Chem. Commun.*, 2017, **53**, 5163–5166.
298 H. Di, W. Jiang, H. Sun, C. Zhao, F. Liao and Y. Zhao, *Thin Solid Films*, 2021, **720**, 138519.
299 J. Zhao, G. Kong, S. Chen, Q. Li, B. Huang, Z. Liu, X. San, Y. Wang, C. Wang, Y. Zhen, H. Wen, P. Gao and J. Li, *Sci. Bull.*, 2017, **62**, 1173–1176.
300 Z. Chen, Q. Dong, Y. Liu, C. Bao, Y. Fang, Y. Lin, S. Tang, Q. Wang, X. Xiao, Y. Bai, Y. Deng and J. Huang, *Nat. Commun.*, 2017, **8**, 1890.
301 Y. Huang, Y. Zhang, J. Sun, X. Wang, J. Sun, Q. Chen, C. Pan and H. Zhou, *Adv. Mater. Interfaces*, 2018, **5**, 1800224.
302 W. G. Li, X. D. Wang, J. F. Liao, Z. F. Wei, Y. F. Xu, H. Y. Chen and D. Bin Kuang, *J. Mater. Chem. C*, 2019, **7**, 5670.
303 Z. Gu, Z. Huang, C. Li, M. Li and Y. Song, *Sci. Adv.*, 2018, **4**, eaat2390.
304 S. Wang, Z. Gu, R. Zhao, T. Zhang, Y. Lou, L. Guo, M. Su, L. Li, Y. Zhang and Y. Song, *Nano Res.*, 2022, **15**, 6568–6573.
305 Y. Liu, Q. Dong, Y. Fang, Y. Lin, Y. Deng and J. Huang, *Adv. Funct. Mater.*, 2019, **29**, 1807707.
306 S. Wang, Y. Chen, J. Yao, G. Zhao, L. Li and G. Zou, *J. Mater. Chem. C*, 2021, **9**, 6498–6506.
307 Y. Liu, J. Sun, Z. Yang, D. Yang, X. Ren, H. Xu, Z. Yang and S. F. Liu, *Adv. Opt. Mater.*, 2016, **4**, 1829.
308 Y. Liu, X. Ren, J. Zhang, Z. Yang, D. Yang, F. Yu, J. Sun, C. Zhao, Z. Yao, B. Wang, Q. Wei, F. Xiao, H. Fan, H. Deng, L. Deng and S. F. Liu, *Sci. China Chem.*, 2017, **60**, 1367.
309 Q. Lv, Z. Lian, W. He, J. L. Sun, Q. Li and Q. Yan, *J. Mater. Chem. C*, 2018, **6**, 4464.
310 Q. A. Akkerman, S. G. Motti, A. R. Srimath Kandada, E. Mosconi, V. D'Innocenzo, G. Bertoni, S. Marras, B. A. Kamino, L. Miranda, F. De Angelis, A. Petrozza, M. Prato and L. Manna, *J. Am. Chem. Soc.*, 2016, **138**, 1010.
311 J. Song, L. Xu, J. Li, J. Xue, Y. Dong, X. Li, H. Zeng, J. Z. Song, L. M. Xu, J. H. Li, J. Xue, Y. H. Dong, X. M. Li and H. Zeng, *Adv. Mater.*, 2016, **28**, 4861.
312 J. Shamsi, Z. Dang, P. Bianchini, C. Canale, F. Di Stasio, R. Brescia, M. Prato and L. Manna, *J. Am. Chem. Soc.*, 2016, **138**, 7240.
313 Z. Zheng, X. Wang, Y. Shen, Z. Luo, L. Li, L. Gan, Y. Ma, H. Li, A. Pan and T. Zhai, *Adv. Opt. Mater.*, 2018, **6**, 1800879.
314 A. Dutta, R. K. Behera, S. Deb, S. Baitalik and N. Pradhan, *J. Phys. Chem. Lett.*, 2019, **10**, 1954.
315 J. Li, Q. Yu, Y. He, C. C. Stoumpos, G. Niu, G. G. Trimarchi, H. Guo, G. Dong, D. Wang, L. Wang and M. G. Kanatzidis, *J. Am. Chem. Soc.*, 2018, **140**, 11085.
316 Q. Zhang, R. Su, X. Liu, J. Xing, T. C. Sum and Q. Xiong, *Adv. Funct. Mater.*, 2016, **26**, 6238.
317 S. Poncé, M. Schlipf and F. Giustino, *ACS Energy Lett.*, 2019, **4**, 456.
318 J. Li, C. C. Stoumpos, G. G. Trimarchi, I. Chung, L. Mao, M. Chen, M. R. Wasielewski, L. Wang and M. G. Kanatzidis, *Chem. Mater.*, 2018, **30**, 4847.
319 C. M. Myae Soe, G. P. Nagabhushana, R. Shivaramaiah, H. Tsai, W. Nie, J. C. Blancon, F. Melkonyan, D. H. Cao, B. Traoré, L. Pedesseau, M. Kepenekian, C. Katan, J. Even, T. J. Marks, A. Navrotsky, A. D. Mohite, C. C. Stoumpos and M. G. Kanatzidis, *Proc. Natl. Acad. Sci. U. S. A.*, 2019, **116**, 58.
320 C. Stoumpos, C. Soe, H. Tsai, W. Nie, J. C. Blanco, D. H. Cao, F. Liu, B. Traoré, C. Katan, J. Even, A. D. Mohite and M. G. Kanatzidis, *Chem*, 2017, **2**, 427–440.

321 S. Han, X. Liu, Y. Liu, Z. Xu, Y. Li, M. Hong, J. Luo and Z. Sun, *J. Am. Chem. Soc.*, 2019, **141**, 12470.
322 A. H. Slavney, T. Hu, A. M. Lindenberg and H. I. Karunadasa, *J. Am. Chem. Soc.*, 2016, **138**, 2138.
323 X. Li, J. Hoffman and M. G. Kanatzidis, *Chem. Rev.*, 2021, **121**, 2230–2291.
324 H. Lai, D. Lu, Z. Xu, N. Zheng, Z. Xie and Y. Liu, *Adv. Mater.*, 2020, **32**, 2001470.
325 X. Li, Y. He, M. Kepenekian, P. Guo, W. Ke, J. Even, C. Katan, C. C. Stoumpos, R. D. Schaller and M. G. Kanatzidis, *J. Am. Chem. Soc.*, 2020, **142**, 6625.
326 Y. Liu, H. Ye, Y. Zhang, K. Zhao, Z. Yang, Y. Yuan, H. Wu, G. Zhao, Z. Yang, J. Tang, Z. Xu and S. F. Liu, *Matter*, 2019, **1**, 465–480.
327 Y. He, W. Ke, G. C. B. Alexander, K. M. McCall, D. G. Chica, Z. Liu, I. Hadar, C. C. Stoumpos, B. W. Wessels and M. G. Kanatzidis, *ACS Photonics*, 2018, **5**, 4132.
328 Y. Zhang, Y. Liu, Z. Xu, H. Ye, Q. Li, M. Hu, Z. Yang and S. F. Liu, *J. Mater. Chem. C*, 2019, **7**, 1584–1591.
329 X. Gong, O. Voznyy, A. Jain, W. Liu, R. Sabatini, Z. Piontkowski, G. Walters, G. Bappi, S. Nokhrin, O. Bushuyev, M. Yuan, R. Comin, D. McCamant, S. O. Kelley and E. H. Sargent, *Nat. Mater.*, 2018, **17**, 550–556.
330 D. Shi, V. Adinolfi, R. Comin, M. Yuan, E. Alarousu, D. Shi, V. Adinolfi, R. Comin, M. Yuan, E. Alarousu, A. Buin, Y. Chen, S. Hoogland, A. Rothenberger, K. Katsiev, Y. B. Losovyj, X. Zhang, P. A. Dowben, O. F. Mohammed, E. H. Sargent and O. M. Bakr, *Science*, 2015, **347**, 519.
331 Y. Gao, E. Shi, S. Deng, S. B. Shiring, J. M. Snaider, C. Liang, B. Yuan, R. Song, S. M. Janke, A. Liebman-Peláez, P. Yoo, M. Zeller, B. W. Boudouris, P. Liao, C. Zhu, V. Blum, Y. Yu, B. M. Savoie, L. Huang, L. Dou and C. D. Davidson, *Nat. Chem.*, 2019, **11**, 1151–1157.
332 C. Zuo, A. D. Scully, W. L. Tan, F. Zheng, K. P. Ghiggino, D. Vak, H. Weerasinghe, C. R. McNeill, D. Angmo, A. S. R. Chesman and M. Gao, *Commun. Mater.*, 2020, **1**, 33.
333 Y. Hu, L. M. Spies, D. Alonso-Álvarez, P. Mocherla, H. Jones, J. Hanisch, T. Bein, P. R. F. Barnes and P. Docampo, *J. Mater. Chem. A*, 2018, **6**, 22215.
334 Y. Liu, Y. Zhang, Z. Yang, H. Ye, J. Feng, Z. Xu, X. Zhang, R. Munir, J. Liu, P. Zuo, Q. Li, M. Hu, L. Meng, K. Wang, D. M. Smilgies, G. Zhao, H. Xu, Z. Yang, A. Amassian, J. Li, K. Zhao and S. F. Liu, *Nat. Commun.*, 2018, **9**, 5302.
335 L. Dou, A. B. Wong, Y. Yu, M. Lai, N. Kornienko, S. W. Eaton, A. Fu, C. G. Bischak, J. Ma, T. Ding, N. S. Ginsberg, L. W. Wang, A. P. Alivisatos and P. Yang, *Science*, 2015, **349**, 1518.
336 A. Z. Chen, M. Shiu, J. H. Ma, M. R. Alpert, D. Zhang, B. J. Foley, D. M. Smilgies, S. H. Lee and J. J. Choi, *Nat. Commun.*, 2018, **9**, 1336.
337 I. C. Smith, E. T. Hoke, D. Solis-Ibarra, M. D. McGehee and H. I. Karunadasa, *Angew. Chem., Int. Ed.*, 2014, **53**, 11232.
338 Q. Zhang, L. Chu, F. Zhou, W. Ji and G. Eda, *Adv. Mater.*, 2018, **18**, 1704055.
339 C. Tan, X. Cao, X. J. Wu, Q. He, J. Yang, X. Zhang, J. Chen, W. Zhao, S. Han, G. H. Nam, M. Sindoro and H. Zhang, *Chem. Rev.*, 2017, **117**, 6225.
340 W. Niu, A. Eiden, G. Vijaya Prakash and J. J. Baumberg, *Appl. Phys. Lett.*, 2014, **104**, 171111.
341 J. C. Blancon, H. Tsai, W. Nie, C. C. Stoumpos, L. Pedesseau, C. Katan, M. Kepenekian, C. M. M. Soe, K. Appavoo, M. Y. Sfeir, S. Tretiak, P. M. Ajayan, M. G. Kanatzidis, J. Even, J. J. Crochet and A. D. Mohite, *Science*, 2017, **355**, 1288.
342 E. Shi, S. Deng, B. Yuan, Y. Gao, Akriti, L. Yuan, C. S. Davis, D. Zemlyanov, Y. Yu, L. Huang and L. Dou, *ACS Nano*, 2019, **13**, 1635.
343 S. Yun, A. Kirakosyan, S. G. Yoon and J. Choi, *ACS Sustainable Chem. Eng.*, 2018, **6**, 3733.
344 V. A. Hintermayr, A. F. Richter, F. Ehrat, M. Döblinger, W. Vanderlinden, J. A. Sichert, Y. Tong, L. Polavarapu, J. Feldmann and A. S. Urban, *Adv. Mater.*, 2016, **28**, 9478.
345 B. J. Bohn, T. Simon, M. Gramlich, A. F. Richter, L. Polavarapu, A. S. Urban and J. Feldmann, *ACS Photonics*, 2018, **5**, 648.
346 Y. Tong, F. Ehrat, W. Vanderlinden, C. Cardenas-Daw, J. K. Stolarczyk, L. Polavarapu and A. S. Urban, *ACS Nano*, 2016, **10**, 10936.
347 D. H. Cao, C. C. Stoumpos, T. Yokoyama, J. L. Logsdon, T. Bin Song, O. K. Farha, M. R. Wasielewski, J. T. Hupp and M. G. Kanatzidis, *ACS Energy Lett.*, 2017, **2**, 982.